Chirped-Pulse Millimeter-Wave Spectroscopy, Dynamics, and Manipulation of Rydberg–Rydberg Transitions

by

Anthony P. Colombo

Submitted to the Department of Chemistry
in partial fulfillment of the requirements for the degree of

Doctor of Philosophy

at the

MASSACHUSETTS INSTITUTE OF TECHNOLOGY

June 2013

Author .....
Department of Chemistry
May 15, 2013

Certified by .....
Robert W. Field
Haslam and Dewey Professor of Chemistry
Thesis Supervisor

Accepted by .....
Robert W. Field
Chairman, Departmental Committee on Graduate Students

This doctoral thesis has been examined by a Committee of the Department of Chemistry that included

Professor Robert G. Griffin .....
Chairperson, Thesis Committee

Professor Sylvia T. Ceyer .....
Member, Thesis Committee

Professor Robert W. Field .....
Thesis Supervisor

Chirped-Pulse Millimeter-Wave Spectroscopy, Dynamics, and Manipulation of Rydberg–Rydberg Transitions

by

Anthony P. Colombo

Submitted to the Department of Chemistry
on May 15, 2013, in partial fulfillment of the
requirements for the degree of
Doctor of Philosophy

Abstract

The chirped-pulse millimeter-wave (CPmmW) technique is applied to transitions between Rydberg states, and calcium atoms are used as the initial test system. The unique feature of Rydberg–Rydberg transitions is that they have enormous electric dipole transition moments: ∼5 kiloDebye at $n^* \sim 45$, where n^* is the effective principal quantum number. After polarization by a mm-wave pulse in the 70–84 GHz frequency region, the excited transitions re-radiate free induction decay (FID) at their resonant frequencies, and the FID is heterodyne-detected by the CPmmW spectrometer. Data collection and averaging are performed in the time domain. The spectral resolution is ∼100 kHz. Because of the large transition dipole moments, the available mm-wave power is sufficient to polarize the entire bandwidth of the spectrometer (12 GHz) in each pulse, and high-resolution survey spectra may be collected. Both absorptive and emissive transitions are observed, and they are distinguished by the phase of their FID relative to that of the excitation pulse. With the combination of the large transition dipole moments and direct monitoring of transitions, dynamics are observed, such as transient nutations from the interference of the excitation pulse with the polarization that it induces in the sample. Transient nutations also provide information about the sample, such as the dipole moment and the number density of Rydberg states. Since the waveform produced by the mm-wave source may be precisely controlled, states with high angular momentum may be populated by a sequence of pulses while recording the results of these manipulations in the time domain. Also, the superradiant decay of the Rydberg sample is probed both directly through FID and indirectly using photon echoes. Prospects for further manipulations, such as adiabatic rapid passage, composite pulses, and optical/mm-wave stimulated Raman adiabatic passage, are evaluated. The application of the CPmmW technique to transitions between Rydberg states of molecules is discussed.

Thesis Supervisor: Robert W. Field
Title: Haslam and Dewey Professor of Chemistry

Acknowledgments

First, I will acknowledge my research advisor, Bob Field. I am confident that the most enduring thing that I have learned from Bob (other than how to turn a scientific phrase) is to always apply the simplest model conceivable to a problem first: Even when the simple approach fails, there is still something to learn from *how* it fails.

For most of my time in the Field Group, I have worked closely with Yan Zhou. I always appreciated his enthusiasm and his insight, and working with him has been excellent. We also worked with Kirill Prozument on the early Rydberg millimeter-wave experiments. In particular, he came up with the approach of using a large interaction volume that initially got things working. I have also enjoyed working closely with David Grimes since he joined the Rydberg Project. Steve Coy helped me especially with developing the phase extraction procedure discussed in Chapter 3. Jeff Kay and Vladimir Petrović introduced me to the Rydberg Project when I was a new graduate student in the group.

Barratt Park designed and assembled the chirped-pulse millimeter-wave spectrometer described in this thesis. We benefited from collaborating with Brooks Pate and Justin Neill on importing the chirped-pulse method into the Field Group as well. I interacted substantially with a few other members of the Singlet Project: Josh Baraban, Bryan Changala, and Adam Steeves, who were willing to provide input and assistance on many issues. Josh Middaugh also gave a helping hand whenever asked.

The Rydberg Project has been supported by the National Science Foundation. For three years, I was supported by a Department of Homeland Security Graduate Fellowship.

Contents

List of Figures

List of Tables

Chapter 1

Introduction

In Sec. 1.1, I discuss some properties of Rydberg states, especially those that are relevant to chirped-pulse millimeter-wave (CPmmW) studies. Sec. 1.2 describes current methods for mm-wave spectroscopy of Rydberg states, including advantages and disadvantages of the most common approach, pulsed-field ionization detection. The chirped-pulse methodology is discussed briefly in Sec. 1.3. The topics of the first three sections are brought together in Sec. 1.4, where I introduce CPmmW studies of Rydberg–Rydberg transitions. Finally, Sec. 1.5 outlines each chapter of this thesis.

1.1 Properties of Rydberg states

In a Rydberg state of an atom or a molecule, an electron is sufficiently highly excited that the electron/ion-core system is correctly described in zeroth order by the Coulomb interaction,

$$V(r) = -\frac{e^2}{4\pi\epsilon_{\mathrm{o}} r}, \tag{1.1}$$

where V is the potential of electron/ion-core interaction, e is the fundamental charge, ϵ_{o} is the vacuum permittivity, and r is the distance between the electron and the ion-core. The allowed energy levels of the system follow the Rydberg equation [74],

$$E = I - \frac{R}{(n-\delta)^2}, \tag{1.2}$$

where E is the energy of the state, I is the ionization limit, R is the Rydberg constant, n is the principal quantum number, and δ is the n-independent quantum defect. That a state falls into such an energy level pattern may be taken as a definition of a Rydberg state. In practice, atomic and molecular states with values of n that are greater than that of the ground state by 1 or more are generally Rydberg states [40].

In some cases, a more convenient label for a Rydberg state is the effective principal quantum number, n^*, is defined as

$$n^* \equiv \sqrt{\frac{R}{I-E}} = n - \delta. \tag{1.3}$$

The n^* notation has the advantage that the many properties of Rydberg states that scale with n scale more accurately with n^*, while the n^* label also provides direct information about the state energy. (The reasons for using primarily n^* notation in this thesis are discussed further in Sec. 2.7.1.) Examples of properties that scale with n^* include the orbital radius, dipole moment, and state density [21]. The scalings of some properties of Rydberg states that are relevant to this thesis are illustrated in Fig. 1-1. For example, it may be shown from Eqs. 1.2 and 1.3 that the energy level spacings scale as

$$\Delta E \propto (n^*)^{-3}. \tag{1.4}$$

Because the level spacing scales with n^*, Rydberg–Rydberg transitions of a given frequency may be located by tuning to the approximate value of n^*. At $n^* \sim 45$, the energy level spacings are approximately 70 GHz, which corresponds to a 4-mm wavelength for electromagnetic radiation to excite a transition.

For Rydberg–Rydberg transitions with $|\Delta n^*| \leq 1$, the transition dipole moment, μ, scales as the radius of the Rydberg orbital. The orbital radius, in turn, is proportional to $(n^*)^2$ (Ref. [21], pg. 26), and thus may become large for Rydberg states. Overall,

$$\mu \propto (n^*)^2 \tag{1.5}$$

for the the electric dipole transition moment. At $n^* \sim 45$, for example, the orbital

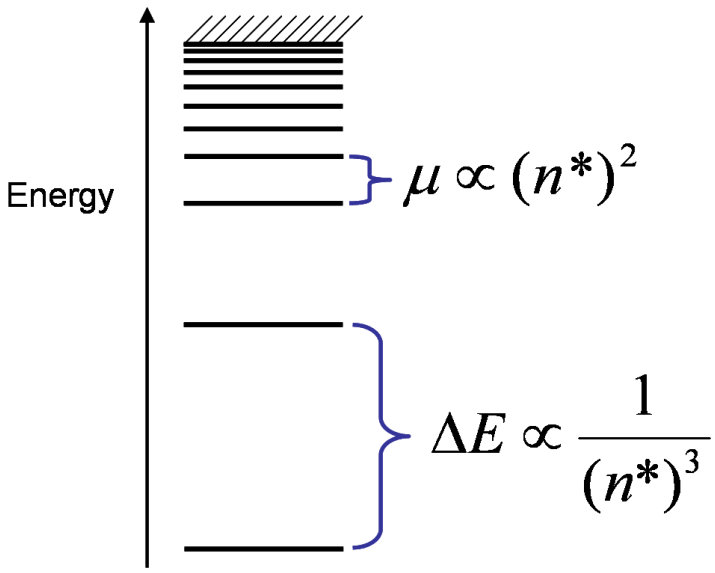

Figure 1-1: The electric dipole transition moment and the energy level spacings of Rydberg states scale with n^*. A schematic of energy levels that follow Eq. 1.2 is depicted, with discrete energy levels converging to an ionization continuum. Because of the $(n^*)^2$, the electric dipole transition moment, μ, becomes very large as n^* increases. Also, the scaling of the energy level spacing, ΔE, guarantees that, for a given (sufficiently large) frequency range, Rydberg–Rydberg transitions will exist at the appropriate value of n^*.

radius is $r \sim 100$ nm. Since the orbital radius of this state is large, and the classical dipole moment is $\mu = er$, it not surprising that these transition dipole moments would also be large. At $n^* \sim 45$, $|\Delta n^*| \leq 1$ Rydberg–Rydberg transition dipole moments are typically ∼5 kiloDebye. Such enormous electric dipole transition moments are a unique feature of electronic transitions between Rydberg states of atoms and molecules. These transition dipole moments are orders of magnitude larger than, for example, the ∼10 D dipole moments for *maximally allowed* optical transitions in a molecule (Ref. [40], pg. 352). Because of their large transition dipole moments, Rydberg states interact strongly with electromagnetic radiation and, via this radiation, with each other.

1.2 Millimeter-wave spectroscopy of Rydberg states: Advantages and challenges

As mentioned briefly in Sec. 1.1, $|\Delta n^*| \leq 1$ Rydberg–Rydberg transitions at medium-to-high n^* occur at mm-wave frequencies. For example, the $34.13p$–$33.67s$ transition in calcium has a frequency of approximately 77 GHz, which corresponds to a wavelength of about 4 mm. Millimeter-wave spectroscopy is an established tool for high-resolution studies of Rydberg atoms [19, 57, 28, 25, 55, 44] and has more recently been extended to Rydberg–Rydberg transitions in molecules [54, 61, 62, 63]. Millimeter-wave (and microwave) spectroscopy is a powerful method for observing the fine and hyperfine structure of Rydberg states, as well as for determining properties of the ion-core, such as its electric multipole moments and polarizabilities [45].

A major advantage of mm-wave spectroscopy over laser spectroscopy for studying Rydberg states is the $> 1000\times$ higher resolution of the mm-waves. With an etalon-narrowed pulsed dye laser of the type that is generally used for laser spectroscopy, spectral resolution is about 1 GHz. However, with mm-wave technologies, resolutions of 100 kHz are routine. Furthermore, Doppler broadening, which often limits the accuracy in a laser spectrum, is proportional to the excitation frequency. Since the frequencies in the mm-wave region are several orders of magnitude lower than laser frequencies, the spectral accuracy may indeed be orders of magnitude higher. It is noted in Ref. [75] that mm-wave spectroscopy is an "attractive option for studies of high Rydberg states" for reasons that include those discussed here.

Millimeter-wave spectroscopy of Rydberg–Rydberg transitions must overcome several significant challenges, however. For transitions with frequencies that are not well-known *a priori* (as is generally the case in spectroscopy), the time required to search for transitions significantly restricts what may be practically accomplished. Scanning through, for example, *one spectrum* with 10 GHz of bandwidth in resolution elements of 100 kHz—with appreciable signal-to-noise—may require *days* of experimental time. Another challenge is the sensitive detection of Rydberg–Rydberg transitions. Just as their large dipoles mean that Rydberg states interact strongly

with electromagnetic radiation, the large dipole moments also mean that Rydberg states are easily perturbed by stray electric fields in the experimental apparatus (see Sec. 2.6.1). Electric fields of 100 mV/cm will easily degrade signals due Stark shifts and inhomogeneous Stark broadening. Since Rydberg states are often detected by pulsed-field ionization, which uses ∼250-V pulses to ionize and extract the Rydberg states from the interaction region, such stray electric fields may be difficult to avoid. Furthermore, to distinguish among multiple Rydberg states in a single experiment, sequences of pulses or voltage ramps must be employed. All of these challenges are addressed using the chirped-pulse mm-wave (CPmmW) method.

1.3 The chirped-pulse millimeter-wave technique

Several years ago, Pate and coworkers developed the chirped pulse Fourier transform microwave (CP-FTMW) technique, which has revolutionized the field of rotational spectroscopy using newly available, fast electronics [11, 10, 17]. Instead of stepping sequentially through individual resolution elements in the frequency domain, an arbitrary waveform generator (AWG) generates a frequency-chirped microwave pulse that polarizes a large bandwidth (∼10 GHz) of rotational transitions in a molecular sample. All of these polarized 2-level systems then re-radiate free induction decay (FID) at their resonant frequencies, which is heterodyne-detected. The signal is digitized directly on a fast (∼10 GHz) oscilloscope. Pate's initial CP-FTMW spectrometer covered a microwave frequency region of 7–18 GHz. Fundamentally, the approach is strongly analogous to the methods used in nuclear magnetic resonance (NMR) spectroscopy (except with higher bandwidth), where all of the 2-level systems within the detection bandwidth are polarized, and the ringing is detected directly. With this approach, the CP-FTMW method allows for the collection of spectra that are simultaneously broadband and high resolution (better than 1 MHz).

Chirped pulse mm-wave (CPmmW) spectroscopy is an extension of CP-FTMW to the mm-wave frequency region (see Chapter 2 and Ref. [64]). Active frequency multipliers are used to generate mm-wave frequencies from the microwave signal of the

AWG. Heterodyne detection is also performed at mm-wave frequencies to convert the signals to the frequency range of our 12-GHz oscilloscope. Like CP-FTMW, CPmmW provides single-shot coverage of ∼10 GHz of spectrum at ∼100 kHz resolution, but at frequencies of 70–102 GHz. The configuration of the CPmmW spectrometer used in this thesis can cover the entire 70–84 GHz frequency range in a single chirp.

1.4 Application of the CPmmW technique to the study of Rydberg–Rydberg transitions

In this thesis, I discuss the application of the CPmmW technique to Rydberg–Rydberg transitions. In the case of CPmmW rotational spectroscopy, typical transition moments are ∼1 D, and hundreds of watts would be needed to fully polarize the molecular transitions over the entire bandwidth of the spectrometer. However, the broadband power that is presently available in the mm-wave region is severely limited. For Rydberg–Rydberg transitions with ∼5 kD transition dipole moments, mm-wave power requirements are reduced by a factor of $\sim 10^6$, compared to a chirped pulse rotational experiment, because the power required to completely polarize a sample scales as μ^{-2}. Thus, current mm-wave technology is well matched to this application.

The CPmmW method is a novel way to obtain spectra of Rydberg atoms and molecules. Transitions between Rydberg states have typically been detected indirectly by collecting ions, electrons, or ultraviolet photons [60, 53, 54, 12, 47, 25, 30, 69, 33, 76, 6, 44, 36, 1, 63, 68, 84, 34, 65, 32]. However, few studies have *directly* detected Rydberg–Rydberg transitions.[1] With its broadband search capability, direct detection, and avoidance of ionization-based detection methods, the CPmmW method surmounts the challenges discussed in Sec. 1.2 above while retaining all of the advantages that mm-wave spectroscopy has over laser spectroscopy. Along with spectroscopy, through the combination of direct, time-domain detection and large

[1] Ref. [57], where superradiant, mm-wave emission of a sodium transition in a cavity was heterodyne-detected, appears to be the only example in the literature of direct detection of Rydberg–Rydberg transitions.

transition dipole moments, dynamical phenomena are observed, such as transient nutations, photon echoes, and superradiant decay. In addition, the coherent mm-wave source can be used to manipulate ensembles that possess these large transition dipole moments; the results of these manipulations are monitored with the CPmmW spectrometer.

Here, CPmmW transitions in Rydberg states of the calcium atom are examined, although the results in this thesis are applicable to other atomic and molecular Rydberg systems. Calcium serves as a convenient system for initial study for several reasons. The spectroscopy of calcium is simplified by the existence of only one abundant isotope, which has zero nuclear spin. Much of the low orbital angular momentum ($\ell \leq 3$) structure of the singlet Rydberg levels in calcium is known from optical studies [79, 23, 9, 4, 8]. Additionally, Gentile *et al.* used microwave and mm-wave spectroscopy to observe the singlet and triplet S, P, and D Rydberg series for principal quantum number $n = 22$–55 [25]. That work provided many candidate transitions for CPmmW experiments as well as quantum defects, which allowed for prediction of other transitions outside the range of their study. The $n = 23$–25 singlet F and G states were examined by Vaidyanathan *et al.* using microwave spectroscopy, and quantum defects for these series were determined [82]. Consequently, the transition frequencies observed in this thesis were either *a priori* known to microwave precision or, because of the known quantum defects, were easily estimated well within the 12-GHz bandwidth of the CPmmW spectrometer.

1.5 Thesis overview

In Chapter 2, I discuss the use of the CPmmW technique for the study of Rydberg–Rydberg transitions, whose enormous electric dipole moments pose unique challenges *and* advantages. The CPmmW spectrometer itself, and its integration into an apparatus for Rydberg–Rydberg transitions are discussed. The roles of pulsed-field ionization as a support and diagnostic technique are also described. The chapter culminates with Rydberg–Rydberg FID spectra and their attributes.

Chapter 3 deals with two related topics: observations of transient nutations and the phases of transitions. For the enormous transition dipole moments of Rydberg systems, the polarization within the sample may be significant compared to the excitation pulse, resulting in transient nutations. In addition to providing spectroscopic information, some of the dynamics are driven by the phase of the FID relative to the excitation pulse that created it. This phase difference and its extraction from the time-domain data are described.

Chapter 4 opens with the manipulation of Rydberg systems with the CPmmW spectrometer. In the process of manipulating the quantum states and coherences of the system, cooperative effects, especially superradiant decay, between atoms in the Rydberg sample are observed. Some other signatures of cooperative effects are also addressed.

Chapter 5 describes numerical simulations of two methods for further manipulation of Rydberg states via robust inversion of populations. Adiabatic rapid passage and composite pulses, both developed initially for use in nuclear magnetic resonance spectroscopy, appear uniquely well-suited to the capabilities of the CPmmW spectrometer.

Chapter 6 describes simulations of the method of stimulated Raman adiabatic passage (STIRAP), which may be used to populate core-nonpenetrating states of Rydberg molecules, and addresses the feasibility of this approach. Such a technique will be valuable for studies of Rydberg molecules because core-nonpenetrating states predissociate much more slowly than their core-penetrating brethren, and thus live long enough that FID spectra of molecules may be collected.

Chapter 2

Design principles and implementation of the CPmmW method for Rydberg–Rydberg transitions

In this chapter, I discuss the technical application of the CPmmW method to the study of Rydberg–Rydberg transitions. The first three sections are concerned with various aspects of the CPmmW method itself. The laser and mm-wave excitation schemes are covered first in Sec. 2.1, and then some specifics of the CPmmW spectrometer—including features unique to Rydberg–Rydberg transitions—are covered in Sec. 2.2. Next, Sec. 2.3 is devoted to the combination of the laser excitation, the CPmmW spectrometer, and the supersonic jet source.

The second three sections of this chapter contain a discussion of pulsed-field ionization (PFI) detection, to the extent that it supports or is relevant to CPmmW experiments. Verification of the optical resonances, which are then used in CPmmW experiments, is outlined in Sec. 2.4. Conversion between and triggering of the CPmmW and PFI experiments is described in Sec. 2.5. Diagnostic uses of the PFI method for CPmmW work are given in Sec. 2.6.

In the last section, Sec. 2.7, I discuss some results of CPmmW experiments on Rydberg–Rydberg transitions. I introduce Rydberg–Rydberg FID spectra, analyze their characteristics, and describe the experimental methods by which spectra are acquired.

2.1 Excitation schemes for Rydberg–Rydberg transitions

The simplest laser/mm-wave schemes for exciting Rydberg–Rydberg transitions are depicted in Fig. 2-1. Two pulsed dye lasers (Lambda Physik Scanmate 2E) excite calcium atoms to an initial Rydberg state. Both dye lasers are pumped at a 20-Hz repetition rate by an injection-seeded Spectra-Physics GCR-290 Nd:YAG laser with a $\sim$7 ns pulse duration. The first transition, from the ground $4s^2\ ^1S_0$ state to the $4s5p$ $^1P_1$ state, uses 544 nm radiation doubled in a β-BBO crystal to 272 nm. The second optical transition populates either a $4sns\ ^1S_0$ or a $4snd\ ^1D_2$ level of $30 < n^* < 60$, which requires laser wavelengths around 800 nm. A chirped or Fourier-transform limited mm-wave pulse then excites Rydberg–Rydberg transitions between 70 and 84 GHz (3.6 to 4.3 mm). In addition to transferring population into the target Rydberg state, the mm-wave pulse polarizes the transition between the two Rydberg states. This polarization is detected in the form of the FID signal. From a $^1S_0$ initial Rydberg state, only $^1S_0$–$^1P_1$ transitions may be observed, and from $^1D_2$, $^1D_2$–$^1P_1$ and $^1D_2$–$^1F_3$ transitions are observable. The laser beams and the mm-waves are vertically polarized, so *all* of the Rydberg states sampled in these experiments are nominally $m = 0$, where m is the magnetic quantum number.

The available frequency range of the mm-wave spectrometer determines the lowest n^* at which Rydberg–Rydberg transitions can be observed. The $|\Delta n^*| \leq 1$ level spacings scale as $2R/(n^*)^3$, where R is the Rydberg constant. Below $n^* \approx 30$, the states with allowed $|\Delta n^*| \leq 1$ transitions are too high-frequency for the spectrometer. At high n^*, though, $|\Delta n^*|$ for accessible transitions need not be ≤ 1, and the available

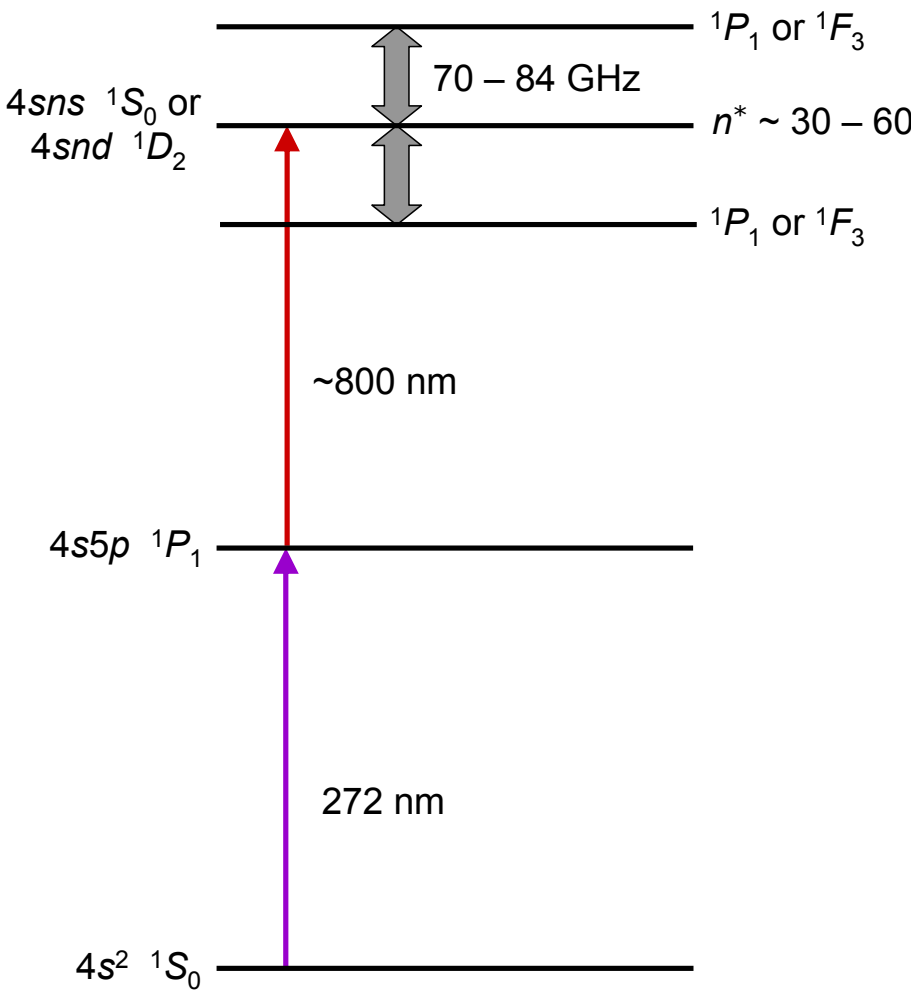

Figure 2-1: Schematic of stepwise, 3-photon excitations of calcium. Sequential laser pulses (thin arrows) populate a $^1S_0$ or $^1D_2$ Rydberg state with effective principal quantum number, n^*, between 30 and 60. The mm-waves (thick arrows) may then transfer population into and create coherences with levels in the 70–84 GHz frequency range (3.6–4.3 mm). The observable types of Rydberg–Rydberg transitions are $^1S_0$–$^1P_1$, $^1D_2$–$^1P_1$, and $^1D_2$–$^1F_3$. Because free induction decay (FID) is detected, transitions to both higher and lower energy are observed.

frequency range is no longer a restriction. Also, available mm-wave power is not a limitation in experiments on Rydberg–Rydberg transitions at the current n^* region, so the smaller transition moments of $|\Delta n^*| > 1$ transitions do not pose a problem. However, for $n^* \gtrsim 60$, the level density becomes sufficiently high that optical transitions into multiple Rydberg states fall within the 1-GHz bandwidth of the dye laser, and I have not thoroughly investigated mm-wave transitions in this n^* region. In practice, I also had difficulty obtaining high-quality FID spectra at higher values of n^*, which may be due to optical thickness causing mm-wave field inhomogeneity as n^* increases (see Sec. 4.2).

2.2 The chirped-pulse millimeter-wave spectrometer

Here, I describe the CPmmW spectrometer, a schematic of which is given in Fig. 2-2. The CPmmW spectrometer, developed primarily by Barratt Park in the Field group, is described in detail in Ref. [64]. For reference, some details of its operation, especially those pertaining to observing Rydberg–Rydberg transitions, are discussed here. The mm-wave-generating moiety of the spectrometer is addressed first in Sec. 2.2.1, then the detection arm in Sec. 2.2.2.

2.2.1 The mm-wave generation arm

To generate the mm-waves, a 4.2-GS/s arbitrary waveform generator (AWG, Tektronix AWG710B) first creates a user-designed pulse at 0.2–2 GHz, which is then mixed (Macom M79 double-balanced mixer) with a 10.7-GHz phase-locked oscillator (Miteq PLDRO-10-10700-3-8P). The output from the mixer, which contains both sum and difference frequencies, is sent through an isolator (Hitachi R3113110 circulator, 8–16 GHz) to prevent reflections back into the mixer and then amplified (Armatek MH978141 amplifier, 1.5–18 GHz). A bandpass filter (Spectrum Microwave C9680-1951-1355) transmits only the lower frequency sideband (8.7–10.5 GHz) from the

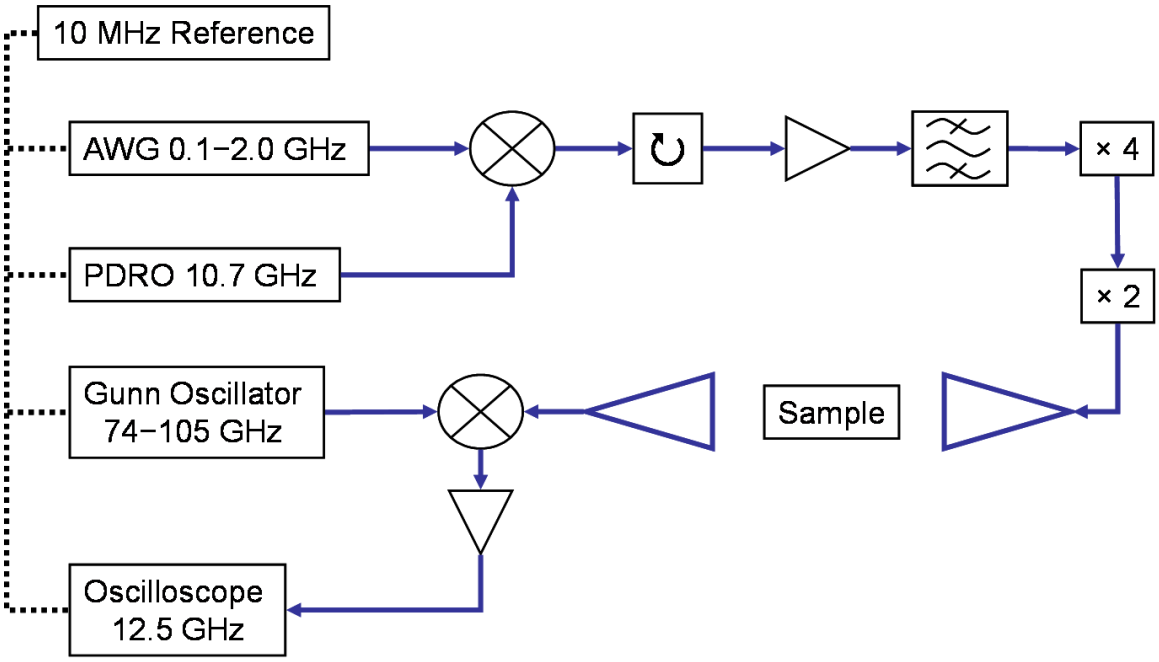

Figure 2-2: Schematic of the CPmmW spectrometer. A pulse from the arbitrary waveform generator (AWG) is mixed with the output of a fixed-frequency phase-locked dielectric resonant oscillator (PDRO). The resulting waveform travels through an isolator, an amplifier, and then a bandpass filter. The filtered signal is octupled in two steps, which generates a roughly constant power of 30 mW in the mm-wave frequency region. The mm-waves are broadcast with a standard gain horn into the sample. The variable attenuator used to prevent overdriving Rydberg–Rydberg transitions is not shown. Another gain horn on the detection side of the spectrometer collects the mm-wave radiation, which is mixed (downconverted) with output from a Gunn oscillator, amplified, and transmitted to the fast oscilloscope. All frequency-generating components and the oscilloscope are referenced (dotted lines) to the 10-MHz clock.

amplifier, and the waveform is sent through an active multiplier chain (a Phase One Microwave PS07-0153A R2 quadrupler followed by a Quinstar QMM-77151520 doubler). The multiplier chain octuples the frequency and, if the pulse is chirped, the bandwidth. The active doubler generates a fixed power level of about 30 mW over the 70–84 GHz output range. A 60-dB variable attenuator is appended after the multipliers. At least some attenuation (typically ∼30 dB) is always necessary to prevent overdriving the Rydberg–Rydberg transitions. When additional attenuation is required, a copy of Ref. [40] is used: The paperback version of Ref. [40] was measured to be a 25-dB attenuator from 70 to 84 GHz.

Once the mm-wave radiation has been generated, a 24-dBi standard gain horn

(TRG 861W/387) broadcasts the mm-wave radiation. Here, the "gain" refers to the enhancement in power that the horn achieves compared to an *isotropic* radiator, hence the units of dBi. This horn concentrates the power along the center-line of beam propagation 250 times better than an isotropic radiator. The broadcast mm-wave radiation is roughly collimated by Teflon lenses before entering the CPmmW vacuum chamber.

2.2.2 The pulse/FID detection arm

After the mm-wave radiation interacts with the calcium sample ($\sim 10^5$ Rydberg atoms/cm^3), Teflon lenses focus the mm-waves into another gain horn for collection. Radiation is then heterodyne-detected by mixing (Ducommun Technologies FDB-12-01 mixer) with a W-band Gunn oscillator (J. E. Carlstrom Co. H129), which is phase-locked using an XL microwave 800A/801 module as shown in Fig. 2-3. The Gunn oscillator may be locked to an integer multiple of the PDRO frequency plus the 10 MHz clock. For example, with the 10.7 GHz PDRO, the Gunn may be run at 74.91 GHz = 7×10.7 GHz + 10 MHz to act as a local oscillator between 70 and 84 GHz. To achieve phase-locking, part of the Gunn oscillator output is sent to a subharmonic mixer (Pacific Millimeter Products WM), where it combines with the PDRO signal. The resulting difference frequency, which should be 10 MHz and phase-stable relative to the rubidium oscillator, is separated using a diplexer and routed to the phase-lock box.

Once the mm-waves have been down-converted, the low-frequency signal is then sent to a low-noise amplifier (Miteq AMF-5D-00101200-23-10P). It is important that this amplifier contribute as little noise as possible to the heterodyne signal because, in general, the first active component on the detection arm will set the noise floor of a spectrometer. The amplified waveform is recorded directly on a 12.5-GHz oscilloscope (Tektronix DPO71254B, 50 GS/s). The 12.5-GHz bandwidth of the oscilloscope restricts the bandwidth within the 70–84 GHz region that can be collected in a single chirp. The oscilloscope and all of the frequency-generating components are phase locked to a 10-MHz rubidium frequency standard (Stanford Research Systems

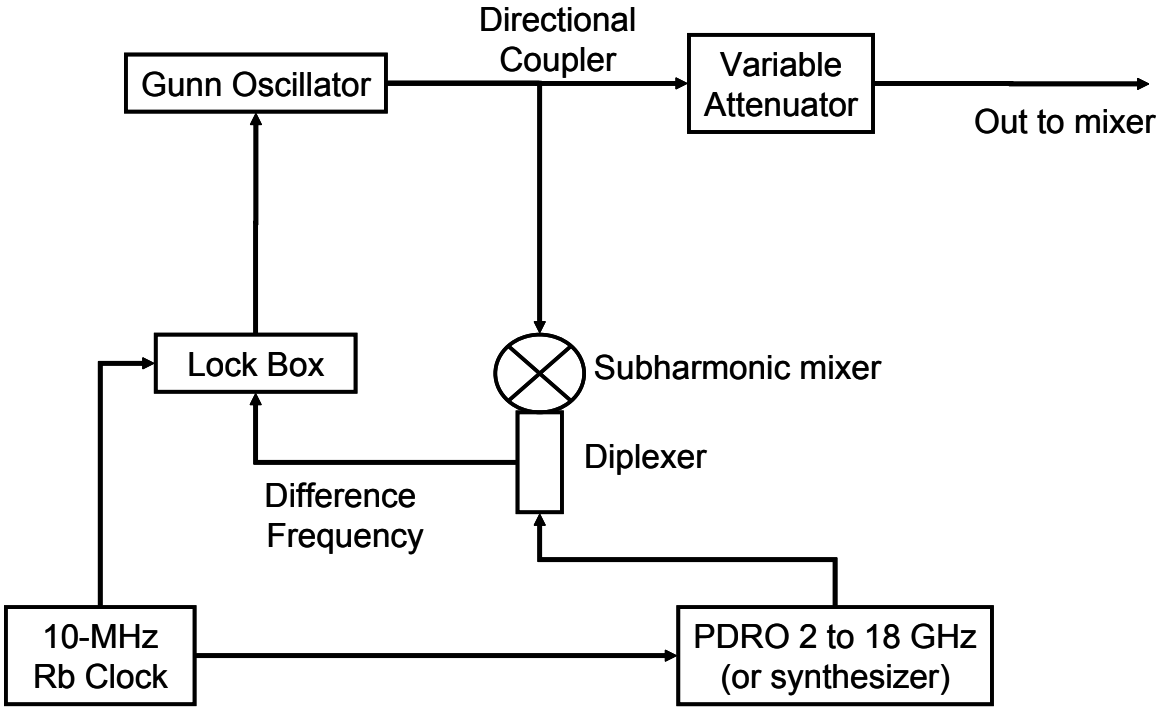

Figure 2-3: The loop for phase-locking the Gunn oscillator to a harmonic of the PDRO plus the 10 MHz clock. A fraction ($\sim$10%) of the power output of the Gunn oscillator is split off using a directional coupler and sent to a subharmonic mixer. Also, the PDRO, which is locked to the 10-MHz reference, sends a signal to the diplexer. The difference of the Gunn oscillator frequency and the integer multiple of the PDRO frequency—which should be the same 10 MHz as the reference—is compared to the 10-MHz clock in the Lock Box to achieve the phase lock. The majority of the Gunn output power is sent to the mixer for heterodyne-dectection of the mm-wave signals.

FS725), which allows the mm-wave signals (transmitted radiation and FID) to be phase-coherently averaged in the time domain. The resolution of the acquired mm-wave spectra is $\sim$100 kHz, which is determined by the duration of the collected FID (typically $\sim$10 μs).

2.3 The laser/mm-wave interaction region

In this section, I discuss the integration of the pulsed dye lasers, the CPmmW spectrometer, and the photoablation supersonic jet source of calcium atoms. In this way, the excitation schemes described in Sec. 2.1 are accomplished.

2.3.1 The guiding design principle: Large interaction volume

When rotational transitions are observed by the CPmmW spectrometer in a supersonic jet expansion [64], the number density of molecules that may be polarized by the mm-waves (the number density difference per quantum state) is typically $\sim 10^{11}$ molecules/cm^3. However, such a high number density of Rydberg atoms would encounter signal loss via dipole–dipole collisional dephasing [22, 65, 72, 3, 59, 1, 78, 80] and cooperative effects such as superradiant decay [70, 18, 77, 48, 27, 29, 57, 84, 86], also discussed in Sec. 4.2. Therefore, the interaction volume was enlarged to compensate for the required lower density of emitters. In this way, I still excite sufficient Rydberg emitters to generate detectable mm-wave FID signals.

2.3.2 Experimental implementation

A schematic of the overall apparatus is shown in Fig. 2-4. Calcium atoms are produced by ablation of a 0.245-inch diameter calcium rod with 5 mJ of the third harmonic of a Spectra-Physics GCR-130 Nd:YAG laser, which is focused to a $\approx$300 μm spot. The ablated calcium is entrained in a $\approx$200-μs long pulse of helium or argon gas, which is generated by General Valve (now owned by Parker Hannafin Corporation) Series 9 nozzle with an Iota One driver. The free jet supersonically expands from a 20-psi stagnation pressure into the CPmmW chamber.

The center of the region where the lasers, mm-waves, and beam of calcium atoms intersect is about 12 cm downstream from the 0.5-mm diameter nozzle. At this distance, the jet has expanded so that its cross-sectional area matches that of the mm-waves ($\sim$10 cm^2), which are not tightly focused. Before entering the CPmmW chamber through a fused silica window, the mm-waves are reflected off of an aluminum mirror. This mirror has a 12-mm hole in its center, and a diverging lens is placed immediately before the hole so that the laser and mm-wave beams have similar diameters in the interaction region. The dye laser beam profiles cover approximately 6 cm^2. When expanded to this size, the spatial profile of the pulsed dye lasers is generally quite non-uniform. Initially, both dye laser beams were spatially filtered

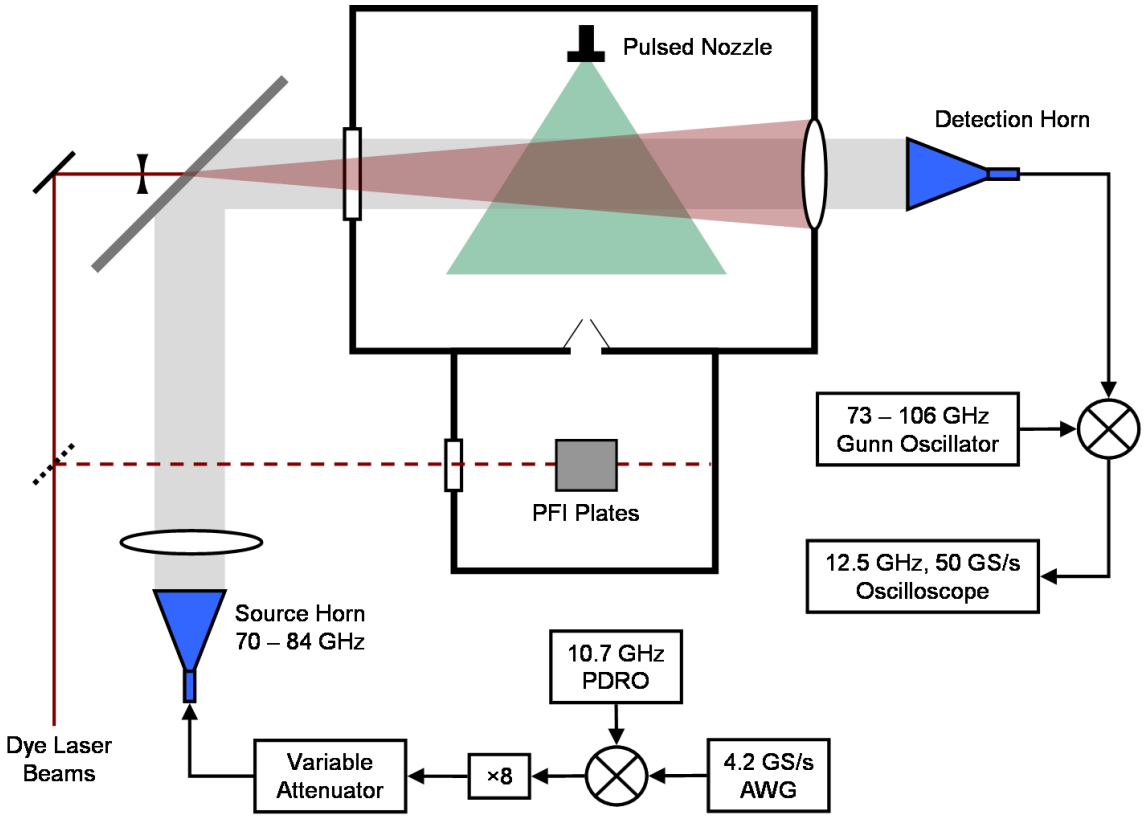

Figure 2-4: Diagram of the experimental apparatus for observing Rydberg–Rydberg transitions. The laser beams pass through an expanding lens and an aperture in a metal mirror before they excite calcium atoms from the ablation source (not shown) into the initial Rydberg state. A gain horn broadcasts the mm-waves (shaded gray), which then interact with the excited calcium atom sample. Another horn collects both transmitted radiation and free induction decay (FID). Teflon lenses collimate/focus the radiation before and after the interaction region. To collect as much mm-wave radiation as possible with the detection horn, a Teflon lens is used as a flange. Detected mm-waves are downconverted by mixing with radiation from a W-band Gunn oscillator, and the resulting signal, between DC and 12.5 GHz, is sent to a fast oscilloscope. Each of the mm-wave generation and detection components is phase-locked to a 10-MHz frequency standard (not shown), which enables averaging in the time domain. The lasers may also be directed into the pulsed field ionization (PFI) region (broken-line path), before which the supersonic expansion is skimmed. The PFI setup is used to tune the lasers into resonance with selected transitions.

in an attempt to avoid generating highly inhomogeneous Rydberg samples. However, spatial filtering was not found to be strictly necessary for obtaining high-quality data from the CPmmW experiments. The total interaction volume of the lasers, mm-waves, and jet expansion is about 50 cm^3.

The electric field ε of the mm-wave source is related to the excitation power P uniformly spread out over an area A by

$$\varepsilon^2 = \frac{2P}{\epsilon_o c A}, \tag{2.1}$$

where ϵ_o is the vacuum permittivity and c is the speed of light. This relation is used to compute the electric field that excites the sample based on the geometry of the interaction volume. To check the spatial profile of the mm-wave beam, a piece of metal foil is inserted into the mm-wave path, and the transmission amplitude is monitored on the fast oscilloscope. However, the wavelength is typically about 4 mm, so the mm-wave radiation is not fully in the far-field limit ($10\lambda = 4$ cm) on the size scale of, for example, the Teflon lenses. Thus, it is difficult to characterize the mm-wave profile, and method of assessing the beam propagation and focusing is only approximate.

The vacuum chamber is electrically grounded, and no electrical components are near the interaction volume. In this way, stray electric fields are minimized sufficiently that their effects are not observed with the apparatus. Helmholtz coils, controlled by variable resistors, partially compensate for ambient magnetic fields that split the Rydberg–Rydberg transitions and/or broaden the lineshapes.

2.4 Pulsed-field ionization detection of Rydberg states

For the CPmmW experiments, the correct laser wavelengths for exciting the desired Rydberg electronic states must be determined. To this end, laser transitions into calcium Rydberg states were also detected by pulsed-field ionization (PFI) in the

same apparatus—but in a different chamber. A schematic of the PFI moiety of the apparatus is shown in Fig. 2-5. To reach the ionization region, the calcium jet travels past the mm-wave-illuminated volume to a 1-mm skimmer, which is 40 cm away from the nozzle and which separates the CPmmW chamber from the PFI chamber. After traversing the skimmer, the jet propagates another 25 cm to the ionization region. Ions are detected with a 75-cm long time-of-flight mass spectrometer. A 250-V extraction pulse propels the ions towards a pair of microchannel plates (Burle Electrooptics, 10 μm in diameter with a 12-μm spacing between the channels) stacked in a chevron arrangement. The PFI instrument (as well as the ablation source) is described in detail in Refs. [14, 26, 36, 35].

When the first laser is tuned to resonance with the $4s5p\ ^1P_1 \leftarrow 4s^2\ ^1S_0$ transition, $1{+}1'$ resonance enhanced multiphoton ionization (REMPI) may be observed. A two-color PFI signal is used to tune the 800-nm laser to resonance with transitions from the $4s5p\ ^1P_1$ state into selected Rydberg states. It is necessary to detect PFI in a separate chamber because the PFI components generate electric fields that shift and broaden the mm-wave transitions. Moreover, the space between the Stark plates in the present apparatus (less than 1 cm) does not provide sufficient interaction volume to yield detectable FID. In practice, PFI signals from Rydberg states were detectable when helium was used as the buffer gas for the jet expansion, but not when argon was used. Argon, however, does give significantly narrower Doppler widths in the CPmmW spectra because argon is 10 times more massive than helium.

2.5 Converting between and triggering of the CPmmW and PFI experiments

Both the CPmmW and PFI experiments employ the same free-jet expansion, and conversion of the apparatus between the two types of experiment requires only a change in the delay for the dye laser pulses and adjustment of two mirrors, a process which is accomplished in a few minutes. A schematic of the pulses for both the

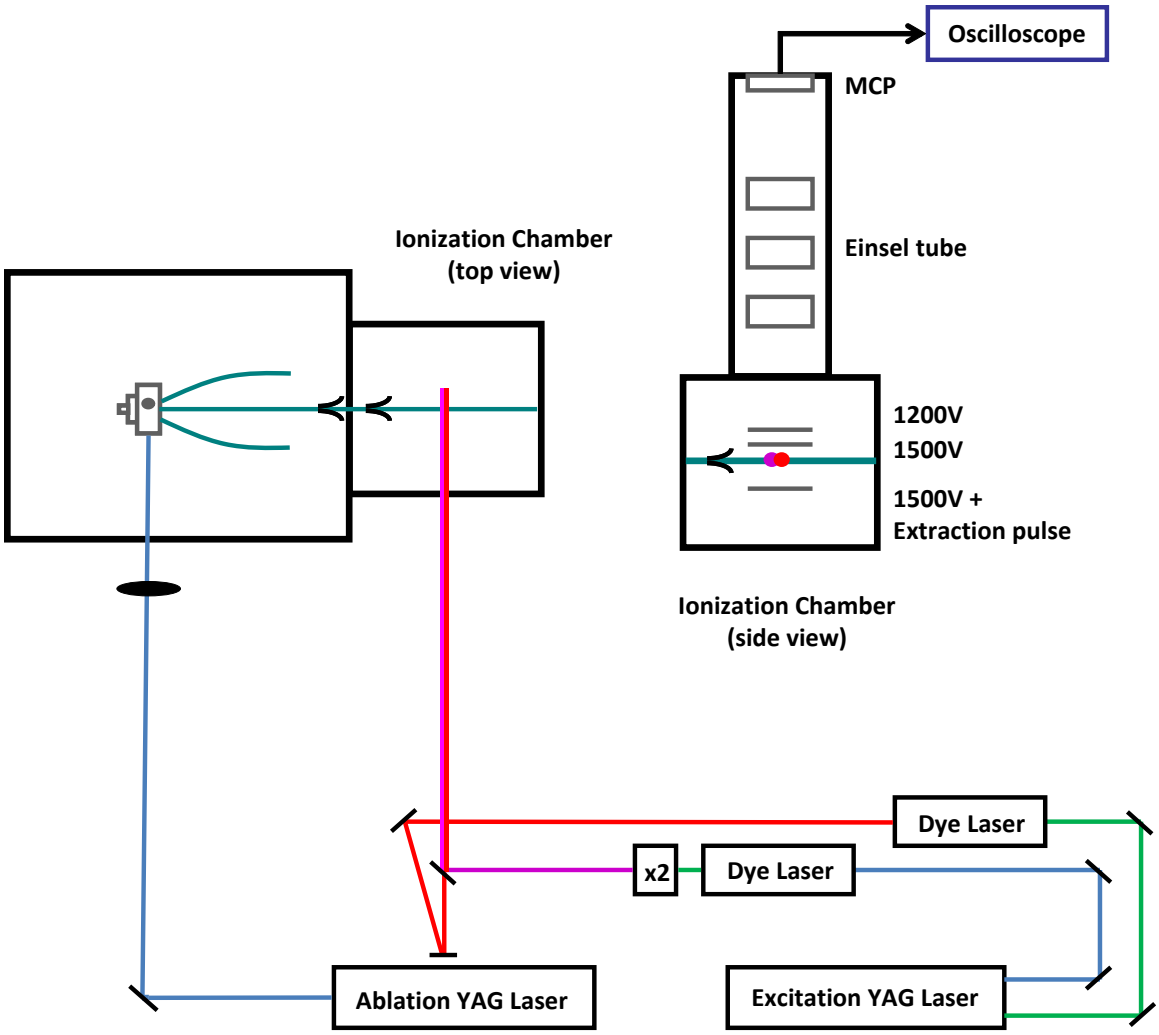

Figure 2-5: Schematic of the PFI apparatus for detecting transitions into Rydberg states. From the source, the jet expansion passes through 1-mm skimmer before entering the ionization region. The atoms in the jet interact with the laser beams between the pair of field plates, which are both nominally set to 1500 V to maintain zero bias. After laser excitation, a positive extraction pulse (≈250 V) is applied to the lower plate, which ionizes the Rydberg states if necessary, and pushes them up out of the interaction region. The 1200-V setting of the upper plate also accelerates the ions upward. The Einsel tube focuses the ion packet, which collides with a microchannel plate (MCP) detector. The detector has two stages, each with an 800-V bias, so that current is generated when ions collide with the MCP. The current is converted to a voltage and sent to a LeCroy 1-GHz oscilloscope for detection. For clarity, the mm-wave components are omitted.

CPmmW and PFI experiments is given in Fig. 2-6.

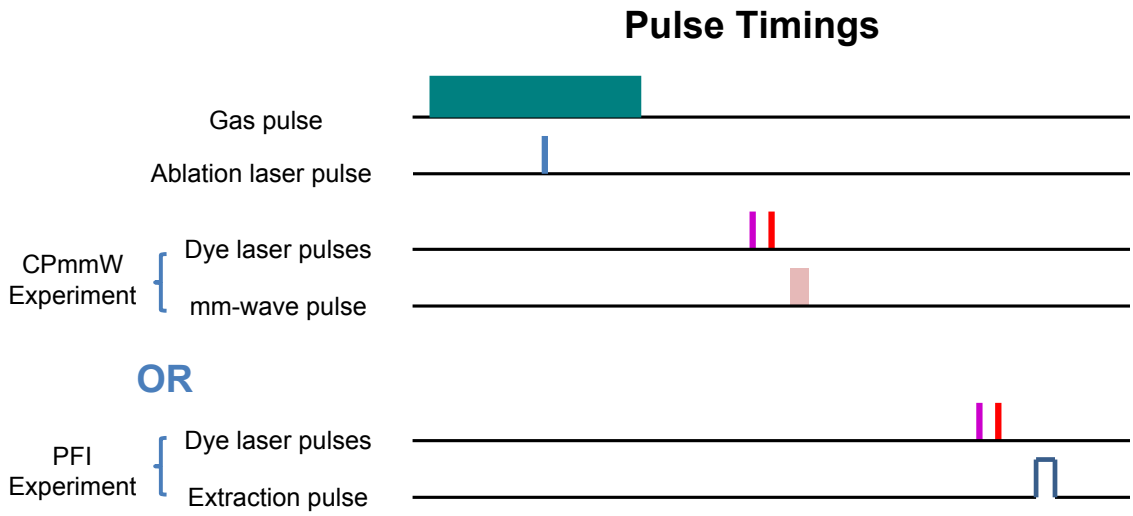

Figure 2-6: Schematic of the timings for CPmmW and PFI experiments. The gas nozzle opens first, during which time the ablation laser fires and generates calcium atoms that are entrained in the jet expansion. For CPmmW experiments, the two dye lasers populate the initial Rydberg state, then the mm-wave pulse interacts with the sample. Alternatively, to do PFI experiments, the dye laser pulses arrive later because the jet must travel further to reach the ionization region. An electrical pulse subsequently ionizes all Rydberg states and propels the ions to the MCP detector.

Due to the design of our AWG, it is not possible to trigger the AWG in a phase-stable way. Thus, in order to average coherently in the time domain, the AWG itself must be used as the master clock, triggering all of the other components in the CPmmW experiments. This trigger ordering is inconvenient because, as shown in Fig. 2-6, the mm-waves arrive after the gas nozzle, ablation laser, and dye laser pulses. Hence, the AWG activates first, waits while the other components are triggered, and then—after a long delay—produces the microwave waveform. To address this issue, the AWG is generally run in "Sequence Mode," where the user specifies each waveform to be executed and how many times to do so. The duration of the sequence is set to add up exactly to the duty cycle period (50 ms for the 20-Hz repetition rate), and the AWG runs continuously.

The values of the delays for the CPmmW and PFI experiments are given in Table 2.1. The AWG first triggers a Stanford Research Systems delay generator

Table 2.1: The delay generator settings for both the CPmmW and PFI experiments. The arbitrary waveform generator (AWG) acts as the master trigger and is used to trigger the first Stanford Research Systems delay generator (SRS1). The trigger output of SRS1 triggers the second Stanford Research Systems delay generator (SRS2). To convert between the CPmmW and PFI experiments, only channel A of SRS2 must be changed.

AWG (Master)	
SRS1 (Slave 1)	
A = T + 24.472 ms	Gas nozzle
B = T + 25.12166 ms	PFI oscilloscope
C = A + 293 μs	Ablation laser flashlamps
D = C + 150 μs	Ablation laser Q-switch
SRS2 (Slave 2)	
A = T + 24.87294 ms	Excitation laser flashlamps (CPmmW)
A = T + 25.1291 ms	Excitation laser flashlamps (PFI)
B = A + 126 μs	Excitation laser Q-switch
C = T + 25.2532 ms	PFI extraction pulse

(SRS DG535), which triggers the gas nozzle, the ablation laser, and the oscilloscope for PFI detection (if applicable). A second SRS DG535 is slaved to the first one, and the second delay generator triggers the excitation YAG laser and the extraction pulse for PFI detection (if applicable). After the first AWG waveform in the sequence triggers the first delay generator, the AWG runs blank waveforms (all points in the waveform have zero amplitude) for ≈25 ms, about half of the duty cycle. At this point, the AWG outputs the waveform desired for the CPmmW experiment, then resumes running blank waveforms to complete the duty cycle.

2.6 PFI detection of Rydberg–Rydberg transitions: Diagnostic tools

Rydberg–Rydberg transitions induced by mm-waves can also be detected by PFI; however, this method of pulsed-field ionization-detected optical–optical–millimeter triple resonance (PFID-OOmmTR) was not found to be feasible for spectroscopy in

this apparatus. Problems with this approach include Stark shifts and line broadenings due to local electric fields. These effects, which are illustrated in Fig. 2-7, are more

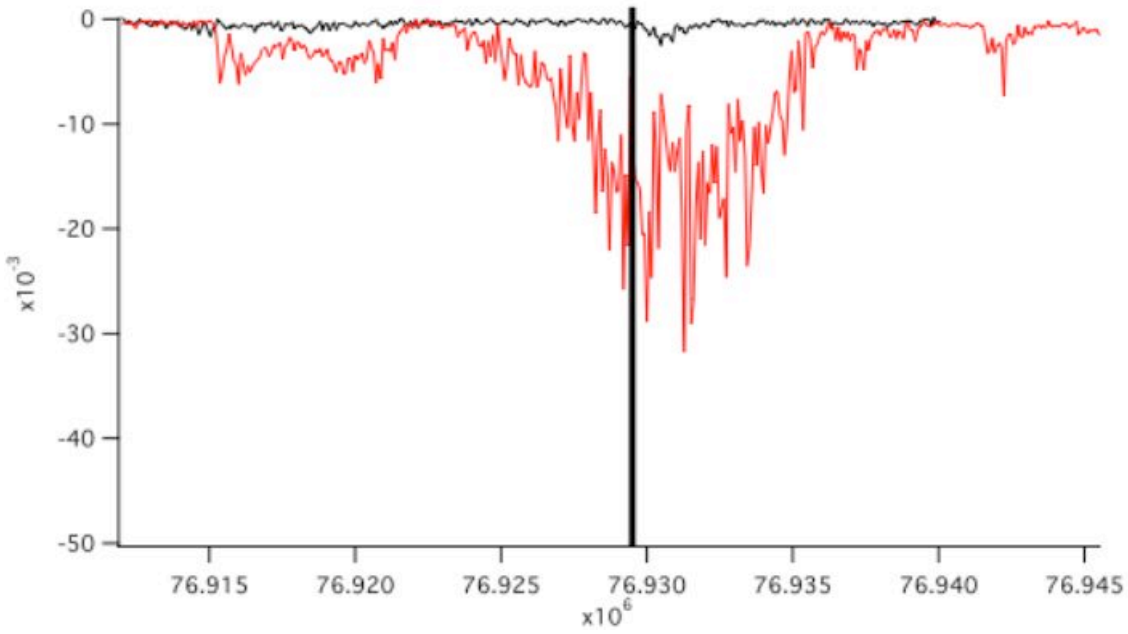

Figure 2-7: A PFID-OOmmTR spectrum of the $34.13p$–$33.67s$ transition exhibits both a Stark shift and broadening due to both stray electric fields and the mm-wave power. The red trace was acquired with ∼10 nW of mm-wave power, and the black trace was acquired with ∼0.1 nW of power. The full width at half maximum of the resonant feature in the black trace is 1 MHz. The black, vertical line indicates the frequency of the transition as measured in Ref. [25] and in Sec. 2.7 below.

pertinent for mm-wave spectroscopy than for optical spectroscopy because the resolution is 1000 times higher in the mm-wave case. For a discussion of the experimental conditions and procedures required to perform spectroscopy using PFID-OOmmTR techniques, see for example Refs. [55] and [54]. Another drawback is large amount of time required to scan the mm-wave source element-by-element (see Sec. 1.2), especially with the instability of our pulsed photoablation source. Both PFID-OOmmTR (Sec. 2.6.1) and purely optical PFI (Sec. 2.6.2), though, may still serve here as useful diagnostics for studying mm-wave transitions between Rydberg states.

2.6.1 PFID-OOmmTR measurement of Rydberg–Rydberg transitions

Even if not employed for high-resolution spectroscopy, PFID-OOmmTR may still be used to search for or verify the presence of Rydberg–Rydberg transitions. After the two dye laser pulses, a gain horn sends a broadband (chirped or Fourier-transform-limited) mm-wave pulse into the region between the PFI plates, and ions from the transitions are detected as in double resonance. The approach is to search for PFI signals that arise from Rydberg–Rydberg transitions, while restricting the bandwidth of each mm-wave pulse to be smaller than that of the fast oscilloscope—about 12 GHz in this case. Thus, if a PFID-OOmmTR signal is detected for some mm-wave pulse, then a Rydberg–Rydberg transition exists within the spectral width of that pulse. The mm-wave frequency region can later be investigated more fully with FID detection, and only one FID experiment is needed per PFID-OOmmTR signal because the fast oscilloscope will cover the entire bandwidth PFID-OOmmTR experiment.

The source arm of the CPmmW spectrometer may be used to generate the mm-waves, or even more simply, a microwave synthesizer may be directly connected to the active multiplier chain. In the latter case, a Hewlett-Packard 8637E Synthesized Signal Generator, which operates from 2.0 to 18.0 GHz, was used. With either microwave source, the approach is less complicated than using the entire CPmmW spectrometer, since no FID detection is involved. A further convenience of PFI detection is that the phase stability of the mm-waves is not a concern, so either the AWG or the synthesizer may be triggered by a delay generator in a straightforward way. Power broadening of the transitions is not a concern for this technique because the search is within the entire bandwidth of the fast oscilloscope. Thus, arbitrarily high mm-wave power (or in practice, less attenuation of the active multipliers) may be used.

A difficulty of the PFID-OOmmTR approach is that the amplitude of the PFI extraction pulse must be set so that it does not ionize the laser-populated Rydberg state, but only ionizes a state that is populated via an upward mm-wave transition. Such selective field ionization is only useful for absorptive (upward in energy) mm-

wave transitions. For upward transitions, in principle, the background is minimal if no mm-wave resonance is excited, and the signal contrast is high. For emissive (downward in energy) transitions, however, depletion of the initial Rydberg state would be monitored, and it would be difficult to achieve sufficiently high contrast to make this approach feasible. A more powerful version of this kind of diagnostic would involve ramped-field ionization. The ramped field would separate different states in the time-of-flight detection channel by ionizing Rydberg states of different energies at different times. Ramped-field ionization detection would also enable detection of both absorptive and emissive mm-wave transitions with similar sensitivity.

2.6.2 Location of Rydberg–Rydberg transitions by purely optical PFI

In atoms, parity is the evenness or oddness of L, the total orbital angular momentum quantum number. Selection rules for spherical symmetry require that the parity of a system change in an electric dipole transition, which leads to the $\Delta\ell \neq 0$ restriction for single-electron transitions [16]. However, application of a small, static electric field breaks the spherical symmetry, allowing parity-forbidden transitions in optical spectra. Moreover, the electric field makes ℓ no longer a good quantum number, and nominally $|\Delta\ell| > 1$ transitions may also be detected.[1] Thus, both states involved in a Rydberg–Rydberg transitions may appear in a *single* optical spectrum, and the energy difference may be measured to laser precision. In Fig. 2-8, for example, both states in the $34.13p$–$33.67s$ ($36p$–$36s$ in $n\ell$ notation) transition appear. In this way, the optical–optical double resonance technique with PFI detection, exactly the same technique that is described in Sec. 2.4, may also be used to identify candidate mm-wave transitions. These transitions may then be confirmed with the PFID-OOmmTR method, discussed in Sec. 2.6.1, or by employing full FID detection. Stark shifts caused by small electric fields are also generally not significant on the

[1] In practice, it is difficult to null the static field in the PFI instrument well enough to *avoid* the presence of parity-forbidden transitions. Moreover, the intensity of these forbidden transitions is an excellent diagnostic with which to minimize empirically the field bias between the two plates.

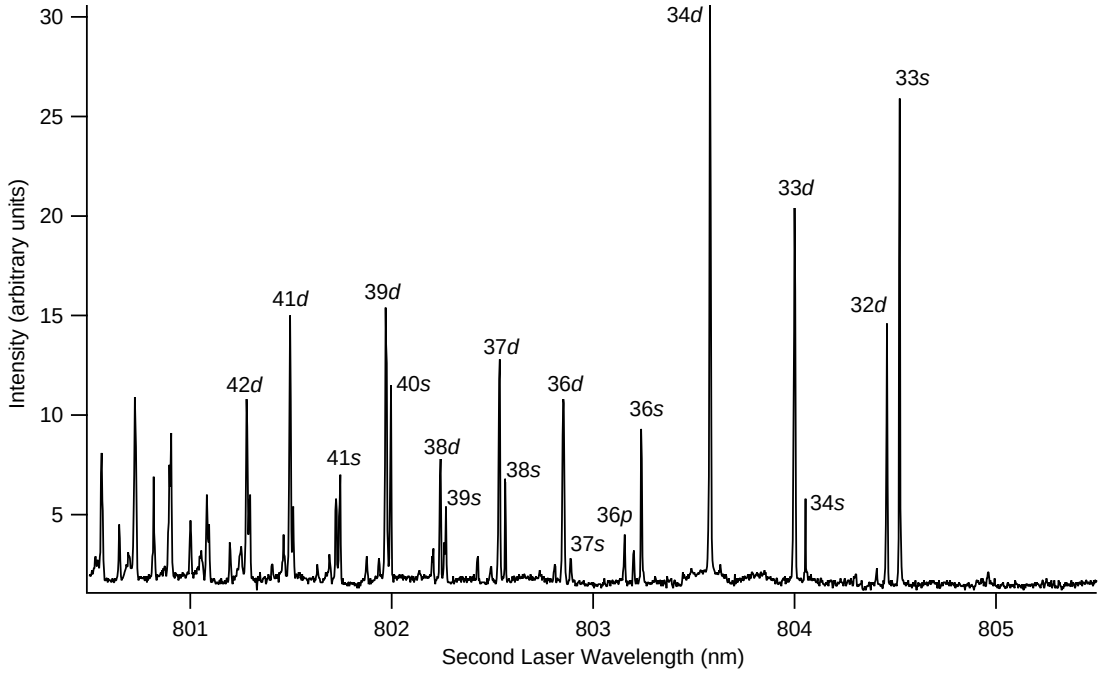

Figure 2-8: A survey spectrum of calcium contains parity-forbidden transitions. In this PFI double resonance spectrum, a nonzero electric field between the PFI plates causes extra lines to appear. Some of the states are labeled with $n\ell$ quantum numbers for reference. Since the intermediate state is a p state, only transitions to s and d states are nominally allowed. However, transitions into some p and f states are also present. Thus, some approximate mm-wave transition frequencies may be determined directly from this spectrum.

scale of the bandwidth of the fast oscilloscope, so any candidate mm-wave transition that is identified from purely optical PFI may be observed in only one mm-wave chirp.

In calcium atoms, of course, many microwave transitions and quantum defects had already been determined by Kleppner and coworkers [25, 82], but in cases where mm-wave transitions are not known *a priori*, the approach described here will be useful. Furthermore, in molecular Rydberg systems, the purely-optical PFI method of detecting both states involved in a mm-wave Rydberg–Rydberg transition is also expected to be applicable.

2.7 Excitation methods and Rydberg–Rydberg FID spectra

In this section, I discuss the methods of exciting Rydberg–Rydberg mm-wave transitions and the FID spectra that result from those excitations. First, the notation for labeling Rydberg–Rydberg transitions is explained in Sec. 2.7.1. Second, the two ways in which Rydberg–Rydberg transitions are excited with the CPmmW spectrometer, (1) single-frequency, Fourier-transform limited pulses and (2) frequency-chirped pulses, are discussed in Sec. 2.7.2. Lastly, Sec. 2.7.3 covers the properties of the FID spectra that are collected.

2.7.1 Notation for Rydberg–Rydberg transitions

Each Rydberg state in a transition is denoted by $n^*\ell$ (see Eq. 1.3), instead of in the $n\ell$ notation that is conventional for atomic systems. For values of the Rydberg constant and the ionization limit that may be used to compute n^* in calcium, see, for example, Ref. [25]. For convenience, Table 2.2 contains both the $n^*\ell$ and $n\ell$ labels of the transitions discussed in this thesis.

Table 2.2: The quantum numbers of the transitions discussed in this thesis are listed in both $n^*\ell$ and $n\ell$ notation.

$n^*\ell$	$n\ell$
$30.12p$–$29.80d$	$32p$–$31d$
$34.13p$–$33.67s$	$36p$–$36s$
$37.78d$–$37.13p$	$39d$–$39p$
$41.73d$–$40.88f$	$43d$–$41f$
$55.8d$–$53.9f$	$57d$–$54f$
$55.9g$–$53.9f$	$56g$–$54f$
$55.9g$–$54.0h$	$56g$–$54h$

The $n\ell$ convention for labeling states provides information on the number of radial nodes of the atomic wavefunction $(n - \ell - 1)$. However, $n^*\ell$ notation is used here primarily because the value of n^* is directly related to the energy of the state through the Rydberg equation (Eq. 1.3). This property is especially informative for examining

transitions between Rydberg states because the energy *differences* that are involved in the transitions are apparent, which is not the case for $n\ell$ notation. Moreover, the differences in the quantum defects between different-ℓ series can be > 1, which may lead to confusion. For example, the $55.8d$–$53.9f$ transition has $\Delta n^* \approx 2$, while it is labeled in Table 2.2 as $57d$–$54f$, which has a nominal Δn of 3. For comparison, the $55.9g$–$54.0h$ transition has a similar transition frequency (different by about 1 GHz) because the absolute energies of the states are similar to those in the $55.8d$–$53.9f$ transition. The $n\ell$ label for this transition, though, is $56g$–$54h$, which has $\Delta n = 2$. While the energies of the states involved are similar, the values of Δn for these two transitions are different, which may lead to confusion. A further advantage of the $n^*\ell$ notation is that it is also the standard for molecular Rydberg systems, where the results discussed in this thesis will also be generally applicable.

2.7.2 Single-frequency versus chirped excitation pulses

Rydberg–Rydberg transitions are excited in two ways, examples of which are shown in Fig. 2-9. In both cases, lasers initially populate the $33.67s$ state in calcium, and the mm-waves then probe the $34.13p$–$33.67s$ transition. In Fig. 2-9(a), the AWG is set to a single frequency, and the bandwidth of the excitation pulse is Fourier-transform-limited. The $34.13p$–$33.67s$ transition has a calculated electric dipole transition moment [70] of 3439 D, and $\pi/2$ polarization occurs in 10 ns with 2 μW of power spread over an ≈ 6 cm^2 spot. Here, the large Rydberg–Rydberg electric dipole transition moment makes it possible for a relatively short pulse to optimally polarize the transition. Alternatively, a resonant, 500-ns pulse would achieve $\pi/2$ polarization for the same transition at 0.6 nW, since the power required for a given pulse area scales as Δt^{-2}, where Δt is the pulse duration.

In Fig. 2-9(c), the frequency of the excitation pulse is chirped linearly in time, and the frequency range of the chirp, rather than the duration of the pulse, determines the bandwidth of the pulse. Since the power of a chirped pulse is distributed over more bandwidth than a transform-limited pulse, a combination of higher power and/or longer pulse duration is required to generate a $\pi/2$ flip angle. For example, the

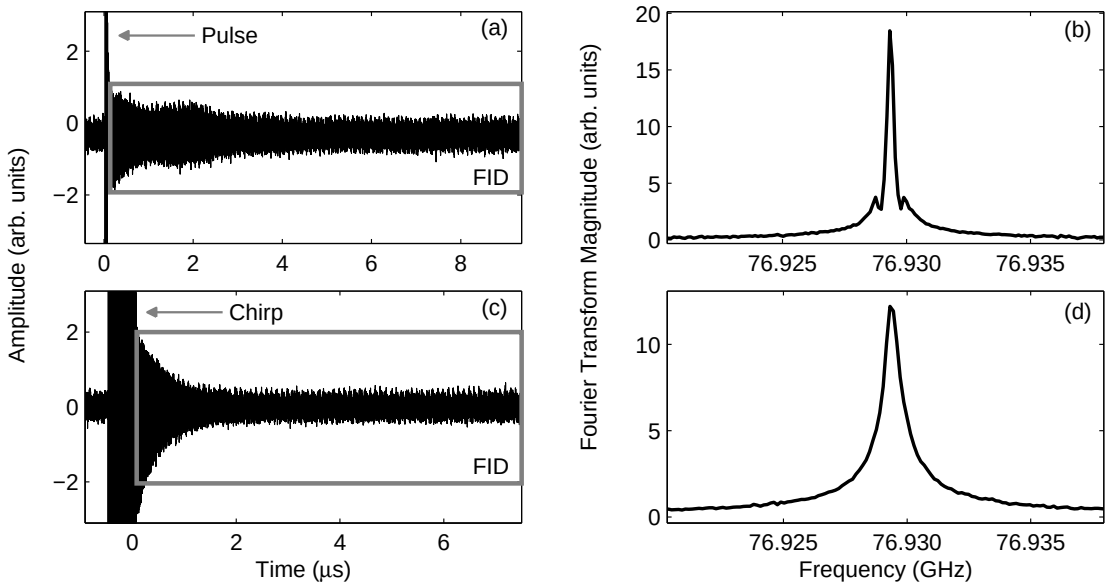

Figure 2-9: Basic single-frequency and chirped excitations of the $34.13p$–$33.67s$ transition in calcium. (a) A 10-ns, transform-limited pulse (with amplitude far larger than the vertical scale of the figure) is followed by FID from calcium in an argon jet expansion. The pulse is centered at the 76.9293 GHz transition frequency [25]. (b) The magnitude Fourier transform of the FID exhibits Zeeman splittings caused by the stray magnetic field that is not completely cancelled by the Helmholtz coils. The full width at half maximum (FWHM) of the center feature is 420 kHz. (c) A chirp over 500 MHz in 0.5 μs excites the same transition in a helium expansion. (d) The Doppler width, which is larger for a helium beam because helium is less massive than argon, is similar to the magnetic field splitting. Therefore, the Zeeman components are not resolved. Both time traces contain artifact oscillations because the 10 MHz frequency from the rubidium standard is present in the detection arm of the spectrometer.

chirp in Fig. 2-9(c) has a bandwidth of 500 MHz and a duration of 0.5 μs, which requires 0.2 μW for optimum, $\pi/2$ polarization of the $34.13p$–$33.67s$ transition. To achieve a given flip angle, the power needed for a chirped pulse scales linearly with the bandwidth if Δt is fixed or scales as Δt^{-1} if the bandwidth is fixed [52]. Of course, for both single-frequency and chirped excitations, the use of shorter pulses (with more power) maximizes the total signal because the earliest, most intense part of the FID cannot be collected while the excitation pulse is present.

2.7.3 Characteristics of Rydberg–Rydberg FID spectra

The spectra in Fig. 2-9 have S/N ratios of about 700 and were obtained from 5000 averages, which required approximately 5 minutes to accumulate. About 0.5 mJ of energy were used for each laser pulse, and the number density of Rydberg atoms in a single n^*, ℓ, $m = 0$ quantum state is estimated as $\sim 10^5/\text{cm}^3$ [70]. The usable FID persists for approximately 10 μs, well after the signal has fallen below the noise floor visible in the time trace. The spectral resolution is $\sim$100 kHz, which is a property of the CPmmW spectrometer that is discussed in Sec. 2.2.2. Linewidths are on the order of 500 kHz, which is consistent with the Doppler dephasing calculated for the geometry of the unskimmed jet expansion plus residual stray magnetic fields. The linewidths are similar in magnitude to those observed in Ref. [25], where the broadening had a different cause: the transit time of the Rydberg sample in a skimmed jet expansion. In cases where the same transition is measured, the frequencies agree with those in Ref. [25] within experimental uncertainty, which is $\sim$10 kHz in Ref. [25] and $\sim$1 kHz here. Since the precision of the transition line center scales linearly with the S/N ratio [67, 13], the line position could be determined even more accurately by averaging for longer than 5 minutes. In Fig. 2-9, the S/N ratio at 5000 averages suggests that a single shot would have S/N of around 10, and experimentally, single-shot signal is clearly visible. The smallest detectable (S/N ratio = 3) number density with 5000 averages is approximately 4×10^3 Rydberg emitters/cm^3, or, in the current experimental geometry, $\lesssim 2 \times 10^5$ total Rydberg atoms.

Along with the $34.13p$–$33.67s$ transition, other typical frequency-domain spectra

of Rydberg–Rydberg transitions are shown in Fig. 2-10. The S/N ratios are similar

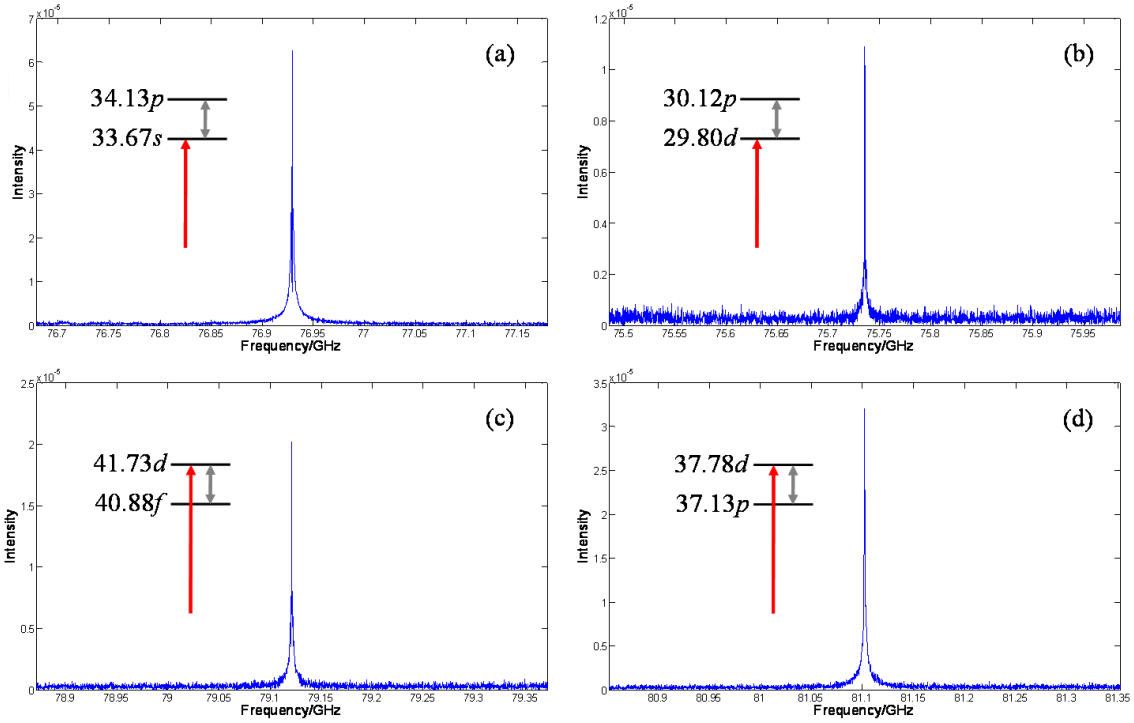

Figure 2-10: Typical Rydberg–Rydberg FID spectra of 4 transitions. The level diagram and the laser (single arrow) and mm-wave (double arrow) excitation schemes are shown in the insets. The transitions observed in panels (a) and (b) are upward in energy (absorptive), while those in panels (c) and (d) are downward in energy (emissive). Experimental conditions are similar to those in Fig. 2-9. Line positions agree with Ref. [25], except for the $41.73d$–$40.88f$ transition in (c), which had not been measured previously. These spectra do not have stray magnetic fields compensated by Helmholtz coils, although the linewidths are still less than 1 MHz.

to those in Fig. 2-9. Since FID from the transition is collected directly, mm-wave transitions that are upward in energy, as in Figs. 2-10(a) and (b), are observed just as well as those that are downward in energy, as in Figs. 2-10(c) and (d).

Chapter 3

Transient nutations and transition phases in Rydberg states

Since the electric dipole moments of Rydberg–Rydberg transitions are so large, radiation from the sample polarization may interfere with the excitation that created it, resulting in transient nutations, which are examined in Sec. 3.1. Transient nutations immediately distinguish absorptive from emissive transitions, providing spectroscopic information that is not generally available in frequency-domain experiments. The dynamics that are in evidence in transient nutations also exemplify the phase difference of the excitation pulse versus the subsequent FID, which is explained in Sec. 3.2. This phase information may be also extracted directly from the time-domain data, the procedure for which is described in detail in Sec. 3.3.

3.1 Transient nutations

One consequence of the kiloDebye dipole moments of Rydberg–Rydberg transitions is that the sample polarization induced by the excitation pulse can be comparable to the electric field of the pulse itself. That is, $\varepsilon \sim \varepsilon_{\text{samp}}$, where ε is the amplitude of the electric field of the excitation pulse (see Eq. 2.1) and $\varepsilon_{\text{samp}}$ is the induced electric field within the sample (compare to Eq. 3.4 below). Under such conditions, the emission from the sample polarization combines coherently with the excitation pulse while the

pulse is present, resulting in transient nutations [70, 81, 51]. For a given pulse area,

$$\theta = \frac{\mu\varepsilon}{\hbar}\Delta t, \tag{3.1}$$

where μ is the electric dipole transition moment, $\varepsilon_{\text{samp}}$ is more likely to be similar to ε if the excitation pulse has a lower power (and hence a smaller ε) and longer duration (Δt). Thus, the induced $\varepsilon_{\text{samp}}$ is a greater fraction of ε.

Another way to describe transient nutations is that excitation is strongly modulated by the Rabi frequency,

$$\omega_R = \frac{\mu\varepsilon}{\hbar}, \tag{3.2}$$

of the excitation (in this case, only resonant excitation is considered). Although a transient nutation is obvious when the amplitude of the modulation is large, this modulation is always present in any excitation. In the rotating frame [71], the state vector precesses at the resonant frequency of the transition. Furthermore, the state vector "nutates," or wobbles at the Rabi frequency for the finite duration that the excitation pulse is present, hence the terminology of "transient nutation."

In this section, various aspects of the transient nutations observed in CPmmW Rydberg–Rydberg transitions are discussed. Transient nutations immediately distinguish absorptive from emissive transitions, which is described in Sec. 3.1.1. The behavior of transient nutations as a function of pulse area for single-frequency excitations is discussed in Sec. 3.1.2. The information that may be extracted from transient nutations, such as the electric dipole transition moment and the sample number density, is the subject of Sec. 3.1.3. Finally, Sec. 3.1.4 addresses transient nutations observed during chirped-pulse excitation.

3.1.1 Transient nutations of absorptive versus emissive transitions

For a resonant, single-frequency excitation pulse in which transient nutations are observed, the sample polarization continues to emit radiation after the excitation pulse

has ended. This radiation is then in the form of Free Induction Decay (FID). Examples of transient nutations are shown in Fig. 3-1 for single-frequency, nearly-$\pi/2$ excitations of the $34.13p$–$33.67s$ and $41.73d$–$40.88f$ transitions. In Fig. 3-1(a), the power used for the $34.13p$–$33.67s$ transition is 0.3 nW at 76.9293 GHz for 0.5 μs. The $34.13p$–$33.67s$ transition is absorptive, since the lower-energy state is initially populated. During the mm-wave pulse, the sample emission interferes destructively with the excitation pulse as the sample accrues polarization, and the amplitude of the excitation pulse appears to decrease in the time domain—consistent with energy conservation. Conversely, Fig. 3-1(b) illustrates an emissive (downward) transition, in which the lasers populate $41.73d$. The $41.73d$–$40.88f$ transition is resonantly excited for 0.2 μs with 1 nW at 79.1212 GHz. Here, the amplitude of the excitation pulse appears to increase with time because the emission from the sample polarization interferes constructively with the pulse. In this way, the nutations immediately display whether the transition is upward or downward in energy relative to the initial population.

3.1.2 Transient nutations of different excitation pulse areas

A series of transient nutations of the $34.13p$–$33.67s$ transition is shown in Fig. 3-2, where the excitation pulse is systematically varied to make pulse areas of $\pi/2$, π, $3\pi/2$, and 2π. All pulses are resonant and single-frequency, with a 1-μs duration. In this way, dephasing effects such as Doppler broadening are the same in each data trace. Each pulse area is controlled by adjusting the power of the mm-wave excitation. In practice, it is easier to search for the power required for a π pulse by monitoring the disappearance of the FID than to try to find a $\pi/2$ pulse by maximizing the FID amplitude. There are two reasons for this: (1) The signal contrast is higher when operating in the nearly zero-background region near a pulse area of π, and (2) the system response is more sensitive to changes in power near π than $\pi/2$ pulse areas because the x-axis projection of the Bloch vector changes more rapidly in the former case. That is, the slope of $\sin\theta$ is 0 at $\theta = \pi/2$ and -1 at $\theta = \pi$. The power for the $\pi/2$ pulse is then 4 times (6 dB) lower than that for the π pulse, which is half the

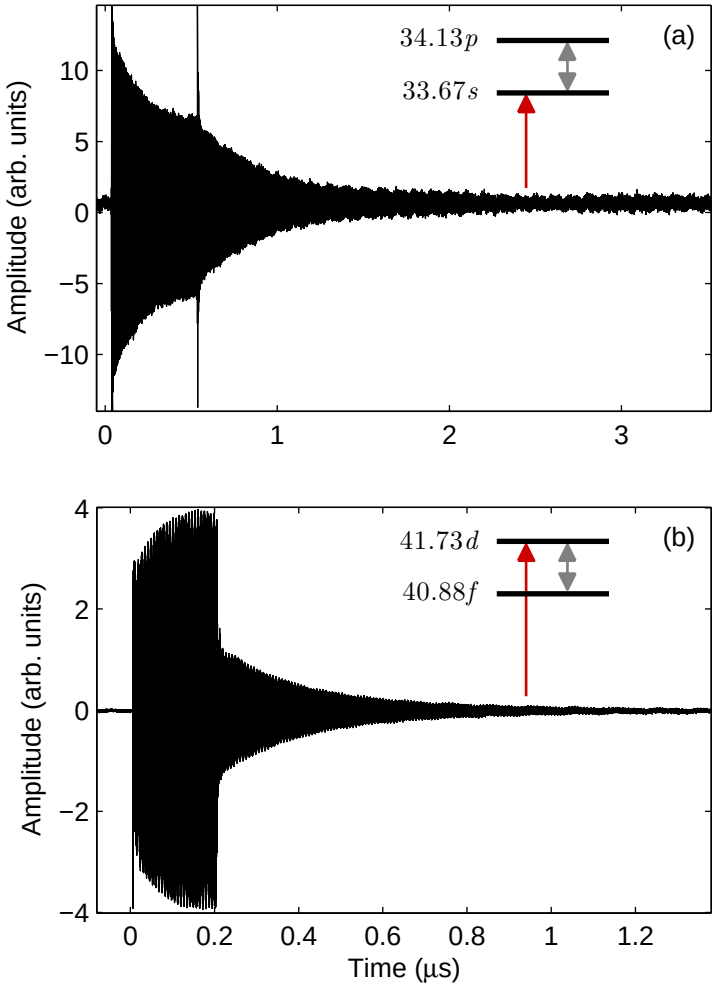

Figure 3-1: Transient nutations display the absorptive or emissive nature of transitions. (a) In the time trace for the absorptive $34.13p$–$33.67s$ transition, the excitation pulse is π radians out of phase with emission from the polarization of the Rydberg sample that the pulse generates. The resulting destructive interference is responsible for the appearance of the decreasing amplitude during the excitation pulse. After the excitation pulse ends at around 0.5 μs, the sample polarization continues to emit radiation, which is considered to be Free Induction Decay (FID) without the excitation pulse present. The inset shows the level diagram, where the laser (red, single arrow) initially populates the lower $33.67s$ state, and the mm-waves (gray arrows) create a coherence with the higher-energy $34.13p$ state. (b) The $41.73d$–$40.88f$ transition is emissive. The sample polarization emission interferes constructively with the excitation pulse, the amplitude of which appears to increase until 0.2 μs, when the excitation pulse terminates. In this excitation sequence, the laser transfers population into the upper state, and the mm-wave transition to the $40.88f$ state is downward in energy.

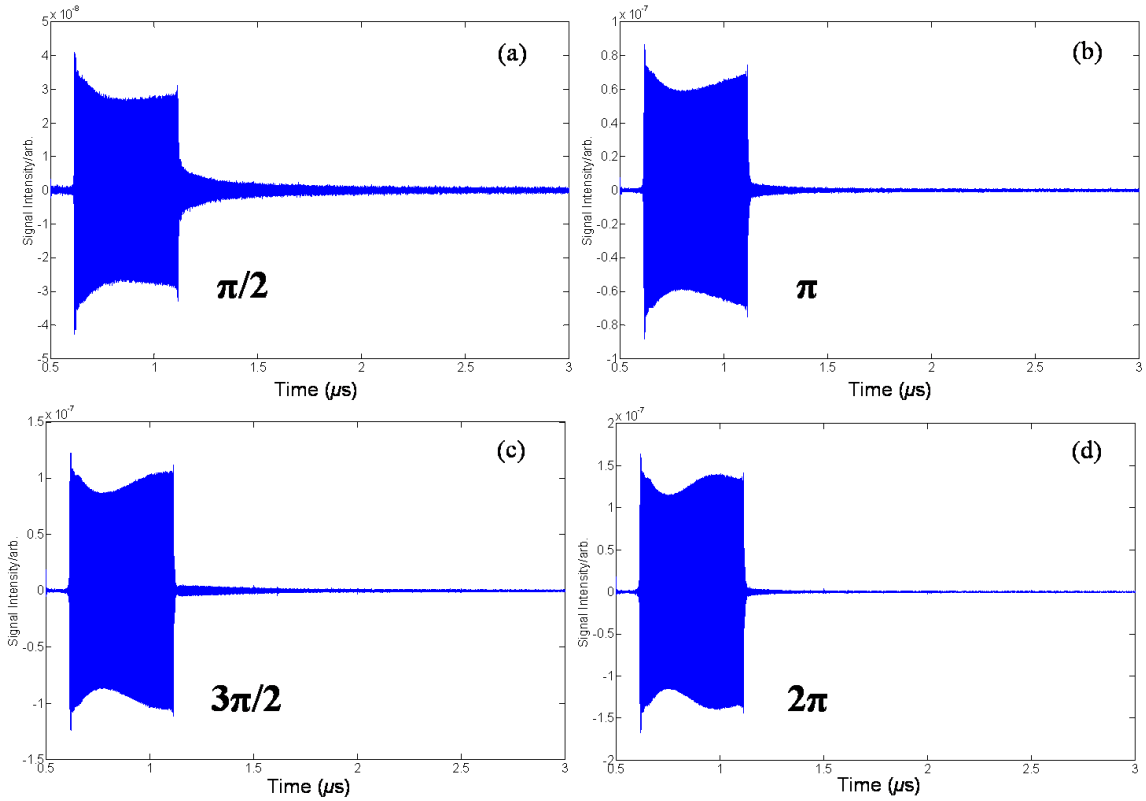

Figure 3-2: Transient nutations exhibit Rabi oscillations in the $34.13p$–$33.67s$ transition. Resonant, single frequency pulses have a 1-μs duration, and the excitation power (and hence electric field) is systematically varied to show its effect. In panel (a), the FID amplitude after the pulse is experimentally maximized. Maximum FID corresponds to an excitation with a pulse area of $\pi/2$. The $\pi/2$ pulse area is also reflected in the shape of the nutation, which appears to have reached a minimum amplitude at the end of the excitation pulse. In panel (b), the excitation power is quadrupled (the electric field is doubled), and minimum FID amplitude is observed, which corresponds to a π pulse. Here, the pulse amplitude seems to decrease and then increase back to its original amplitude. This behavior is consistent with completely inverting the population in the 2-level system. Pulse areas of (c) $3\pi/2$ and (d) 2π are also shown. The FID amplitudes in panels (a) and (c) are approximately the same, although the scale and the excitation pulse amplitude are different. As in panel (b), the FID amplitude in panel (d) is minimal. The amplitudes of the higher-pulse-area nutations dephase at a rate proportional to the driving field. The period of the nutation is a measure of the Rabi frequency of the transition, and the depth of the nutations indicates the number density of Rydberg emitters.

electric field.

In Fig. 3-2(a), the variable attenuator is adjusted to make a pulse area of $\pi/2$, which corresponds to maximum FID. (That the FID is maximized is confirmed by slightly tuning the variable attenuator in either direction.) As in Fig. 3-1(a), the amplitude of the excitation pulse appears to decrease because the lower state is initially populated by the lasers. Here, however, the amplitude of the excitation pulse looks like it reaches a minimum when the excitation pulse terminates. Because the interference of sample polarization with the excitation pulse is destructive, this behavior means that the sample polarization has reached a maximum. Maximum sample polarization, in turn, corresponds to a $\pi/2$ pulse.

In Fig. 3-2(b), the excitation power is quadrupled relative to that for Fig. 3-2(a) (so that the electric field is doubled), which doubles the pulse area for a given pulse duration. The FID amplitude is minimal,[1] which confirms that the pulse area is π. In this case, the excitation pulse amplitude appears to go through a minimum, and then it returns to its initial level. The sample polarization is zero, and thus no longer destructively interfering with (absorbing energy from) the excitation field, which corresponds to having moved all of the population into the upper state with the π pulse.

Fig. 3-2(c) shows a $3\pi/2$ pulse, which again has maximum FID; the FID amplitude in Fig. 3-2(c) is approximately the same as in Fig. 3-2(a), although the scale is different because the excitation pulse has a larger amplitude. The contour of the pulse goes through a minimum and then reaches a maximum that is greater than the original pulse amplitude. The system has been inverted, and the sample polarization is now destructively interfering with the driving field, so it appears that total amplitude is higher. In Fig. 3-2(d), which shows a 2π pulse, the FID amplitude is minimal—approximately the same as in Fig. 3-2(b). After going through the maximum that is seen in the case of the $3\pi/2$ pulse, the excitation pulse amplitude appears to return to its initial level.

[1]The nonzero FID amplitude in Figs. 3-2(b) and (d) indicates that the mm-wave beam profile is likely inhomogeneous.

3.1.3 Information from transient nutations

Transient nutations provide an obvious example of the electric field of the mm-waves modulating a transition at the Rabi frequency (Eq. 3.2). Thus, the period of a transient nutation, $T_{\rm nut}$ is related to the Rabi frequency by

$$T_{\rm nut} = \frac{2\pi}{\omega_R} = \frac{h}{\mu\varepsilon}. \tag{3.3}$$

Since $T_{\rm nut}$ is directly observable from oscillations within transient nutations, such as those in Fig. 3-2, $T_{\rm nut}$ provides a stand-alone measure of the Rabi frequency in a single data trace. In cases where the transition dipole moment is known or *a priori* calculable, such as for the $34.13p$–$33.67s$ transition, the nutations may confirm the amount of power that is being used to drive a transition via Eq. 2.1 (given that the beam area of the mm-waves is measured as well). Conversely, if the power through the mm-wave spectrometer is measured, then transient nutations can be used to determine an unknown transition dipole moment.

In the traces with larger pulse areas, the transient nutations exhibit a dephasing whose rate is proportional to the driving electric field. That is, the nutations of the 2π pulse in Fig. 3-2(d) dephase faster than those of the $3\pi/2$ pulse in Fig. 3-2(c). This behavior creates asymmetry in the contours of the transient nutations, which is visible in Figs. 3-2(b), (c), and (d). The dephasing may be due to inhomogeneities in the driving electric field, which would cause different Rydberg atoms to have different Rabi frequencies. Electric field inhomogeneity is also consistent with the observation that FID signals from $\pi/2$ pulses are larger than those from, for example, $5\pi/2$ pulses.

The depth of the transient nutation in, for example, Fig. 3-2(a), is determined by the magnitude of the macroscopic sample polarization that interferes with the excitation pulse. The electric field from a $\pi/2$-polarized sample is

$$\varepsilon_{\rm samp} = \frac{\mu N}{4\pi\epsilon_{\rm o}}\frac{L}{\lambda}, \tag{3.4}$$

where N is the Rydberg number density, λ is the wavelength of the radiation, and L is

the path length of the radiation through the sample. For the $34.13p$–$33.67s$ transition, $\lambda = 3.9$ mm, and the path length in the apparatus is at least 7 cm. Rewriting Eq. 3.1, the electric field of the excitation pulse is related to the pulse area by

$$\varepsilon = \frac{\theta\hbar}{\mu\Delta t}. \tag{3.5}$$

From the depth of transient nutations such as that observed in Fig. 3-2(a) (which is ≈30%), and the $\theta = \pi/2$ pulse area, the number density of Rydberg atoms may be determined. Taking the ratio of Eq. 3.4 to Eq. 3.5,

$$\frac{\varepsilon_{\text{samp}}}{\varepsilon} = \frac{\mu^2 N}{4\pi\epsilon_{\text{o}}}\frac{\Delta t}{\theta\hbar}\frac{L}{\lambda}, \tag{3.6}$$

and setting the ratio on the left hand side equal to the depth of modulation gives $N \sim 10^6$ Rydberg emitters/cm^3.

3.1.4 Transient nutations in chirped-pulse excitation

In addition to transient nutations in single-frequency excitations, Fig. 3-3 shows a transient nutation in a chirped mm-wave excitation. In this case, the chirped pulse covers 500 MHz of bandwidth in 500 ns with 0.1 μW of power. The frequency of the chirp passes through the $34.13p$–$33.67s$ resonance halfway through the pulse. Without calcium atoms present, the only response is that of the mm-wave spectrometer to different frequencies. With calcium atoms present in the $33.67s$ state, the data trace initially parallels the one without calcium atoms because the chirp is far from resonance. At around 200 ns in the gray trace, the amplitude appears to decrease relative to the black trace, corresponding to nonresonant interaction with the $34.13p$–$33.67s$ transition. Again, the decrease in amplitude occurs because this transition is absorptive, whereas the amplitude would increase for an emissive transition. The sample polarization continues to interfere destructively with the chirped pulse, absorbing energy from the excitation field, until the sweep accrues maximum polarization at resonance. Then, the polarization of the $34.13p$–$33.67s$ transition interferes with the

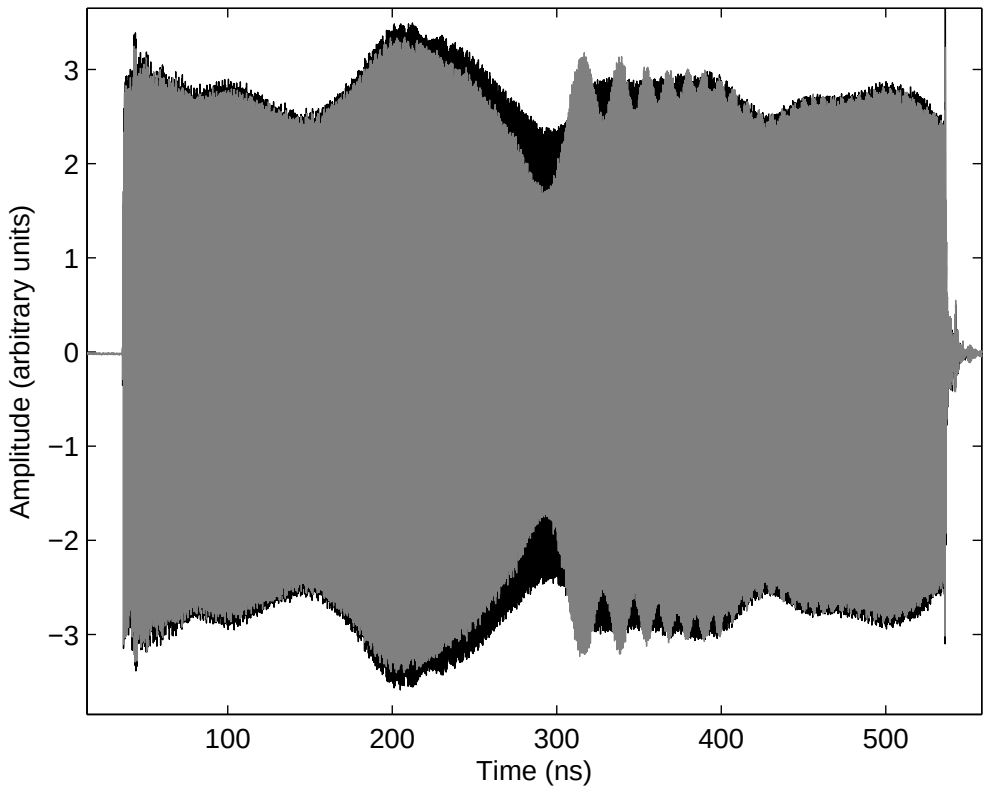

Figure 3-3: Transient nutation in a chirped excitation. A 0.1-μW chirp with a duration of 500 ns and a bandwidth of 500 MHz covers the $34.13p$–$33.67s$ resonance, without calcium atoms present (black, background trace). The contour of the trace is due to the response of the mm-wave spectrometer to different frequencies. With atoms present (gray, foreground trace), the shape initially follows that of the black trace. As the chirp approaches the $34.13p$–$33.67s$ resonance, which is at the center of the frequency sweep, the amplitude appears to decrease as the system nonresonantly interacts with the mm-waves. When the sweep passes through resonance, more energy is absorbed from the radiation field and more sample polarization is accrued. The sample polarization then interferes with the chirp, resulting in the visible beating pattern.

chirped pulse, visible as beating in the data trace. Because the $34.13p$–$33.67s$ transition is at a fixed frequency, the oscillations get closer (i.e. faster) together as the frequency of the chirp continues to increase. The envelope of the interference pattern still follows that of the black trace.

3.2 Principles of transition phases

In the case of obvious transient nutations, the phase of a transition (absorptive or emissive) is immediately discernible from the shape of the nutation. In Fig. 3-1(a), the excitation pulse and the sample emission are π radians out of phase (absorptive), whereas in Fig. 3-1(b) they have the same phase (emissive). However, the phase difference between the excitation pulse and the FID can also be extracted from the oscillations that are recorded directly in the time domain.

This section deals with the principles of transition phases, while the detailed procedure for the extraction of transition phases is in the next section, Sec. 3.3. First, I show in Sec. 3.2.1 that the accuracy of CPmmW data is far higher than sufficient to determine whether a transition is absorptive or emissive. Then, in Secs. 3.2.2 and 3.2.3, I describe transition phases that may be determined for single-frequency and chirped-pulse excitations, respectively.

3.2.1 High accuracy of phase information

To estimate a *lower bound* on the precision with which the phase of any FID, ϕ_{FID}, can be determined, the uncertainty in the time measurement, which comes from the 10-MHz frequency standard, is assumed to be negligible. The relative standard deviation (RSD) of ϕ_{FID} is also assumed to be no smaller than the combination of relative uncertainties in the other fitted parameters (decay rate, γ, frequency, ν, and amplitude, A) that reproduce the FID. That is, for the FID it is assumed that

$$\mathrm{RSD}_{\phi}^{2} = \mathrm{RSD}_{\gamma}^{2} + \mathrm{RSD}_{\nu}^{2} + \mathrm{RSD}_{A}^{2}. \tag{3.7}$$

In the CPmmW experiments discussed here, the precisions of γ_{FID} and A_{FID} are similar (while the precision of ν_{FID} is much higher), and the relative uncertainties of each are $\approx$(S/N ratio)$^{-1}$ [67, 13]. Thus, for the FID,

$$\mathrm{RSD}_{\phi} \approx \frac{\sqrt{2}}{\text{S/N ratio}}. \tag{3.8}$$

The S/N ratio of the excitation pulse is generally much higher than that of the FID, and thus uncertainties in the excitation pulse parameters are not considered here. For spectra such as those in Fig. 2-9, the relative uncertainty in γ_{FID} and A_{FID} is thus $\sim 10^{-3}$, which corresponds to an uncertainty in ϕ_{FID} of $<0.01\ \pi$ radians. Even this conservative estimate of the precision of the fitted ϕ_{FID} far exceeds what is necessary to distinguish absorptive (π phase difference) from emissive (0 phase difference) transitions.

3.2.2 Transition phases for single-frequency excitation

For a resonant, single-frequency excitation pulse ($\omega_{\mathrm{pulse}} = \omega_{\mathrm{FID}}$, where ω is the angular frequency) with phase ϕ_{pulse}, the phase difference, $\Delta\phi$, between the pulse and FID is simply

$$\Delta\phi = \phi_{\mathrm{FID}} - \phi_{\mathrm{pulse}}. \tag{3.9}$$

The phase of the time-domain oscillations of the excitation pulse is directly compared to the phase of the FID oscillations, and the phase difference (π or 0) identifies the upward or downward nature of the transition. This phase comparison is shown pictorially in Fig. 3-4. Thus, determination of the relative phase of the pulse and the FID need not require observation of nutations. Moreover, whether a transition is absorptive or emissive can be inferred from a time trace in which the excitation pulse is at a constant (possibly off-scale) amplitude. An example of this case is in Fig. 2-9(a), where the phase of the FID is indeed measured (using the methods described in Sec. 3.3 below) to be π radians different than the phase of the excitation pulse, as is expected when the lasers initially populate the lower state.

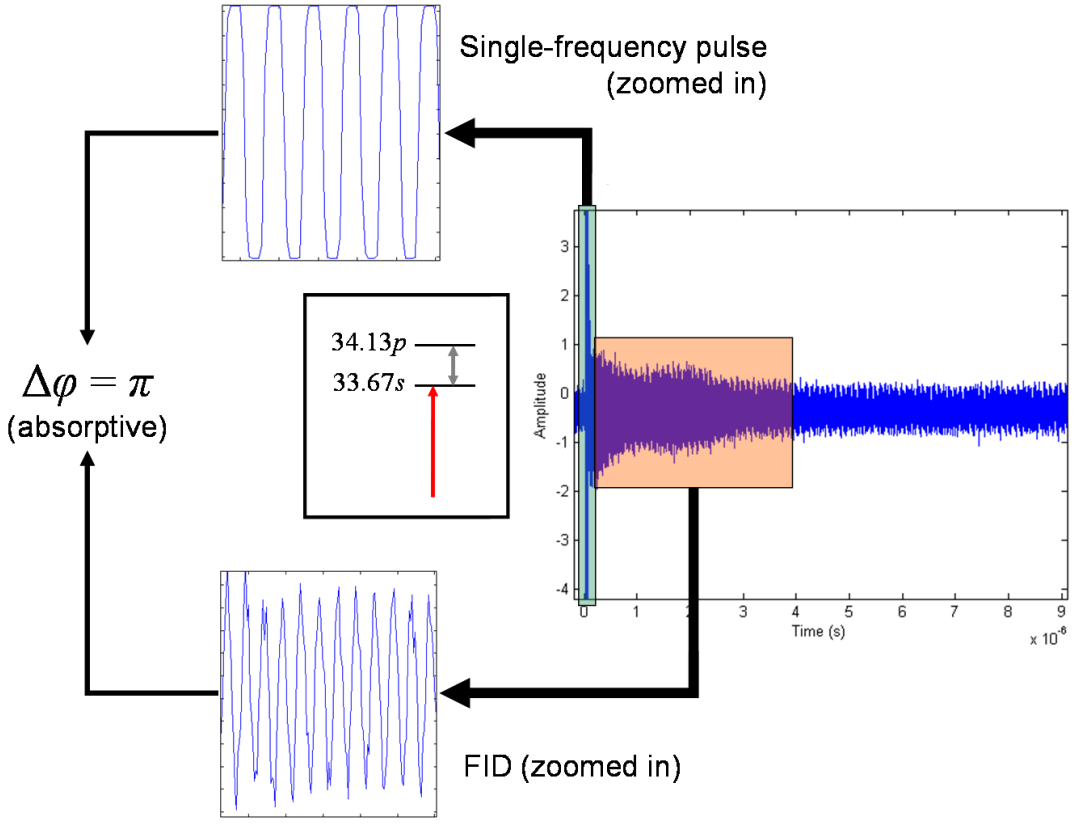

Figure 3-4: Excitation pulse and FID phases may be compared to determine whether a transition is absorptive or emissive. On the right is a time trace for a 10-ns, resonant excitation of the $34.13p$–$33.67s$ transition. The top frame shows a zoomed-in portion of the excitation pulse, while at the bottom is a zoomed-in portion of the FID. Since both the pulse and the FID are recorded on the same time axis, the oscillations of each can be compared to determine the relative phase. Since the lasers initially populate the lower state in this case, the phase difference is π radians.

3.2.3 Transition phases for chirped-pulse excitation

Measurement of the phase of the FID relative to that of the excitation can be extended to the case of a chirped excitation pulse. For a linearly chirped pulse, the phase at time t is

$$\phi_c(t) = \phi_o + \omega_o t + \frac{1}{2}\frac{\Delta\omega}{\Delta t}t^2, \tag{3.10}$$

where ϕ_o is the initial phase of the chirp, ω_o is the initial angular frequency of the chirp, and $|\Delta\omega|$ is the bandwidth of the chirp. (If the frequency of the chirp is increasing during the pulse, $\Delta\omega > 0$, and $\Delta\omega < 0$ if the frequency is decreasing.) The

sweep rate of the chirp is $\Delta\omega/\Delta t$, and the frequency of the chirp at a given time is

$$\omega_{\rm c}(t) = \omega_{\rm o} + \frac{\Delta\omega}{\Delta t}t. \tag{3.11}$$

The phase of the chirp may also be related to the instantaneous frequency by combining Eq. 3.10 with Eq. 3.11 and eliminating t:

$$\phi_{\rm c}(\omega_{\rm c}) = \phi_{\rm o} + \frac{1}{2}(\omega_{\rm c}^2 - \omega_{\rm o}^2)\left(\frac{\Delta\omega}{\Delta t}\right)^{-1}. \tag{3.12}$$

If the FID of a transition is recorded at a frequency $\omega_{\rm FID}$ and with a phase $\phi_{\rm FID}$, then the FID phase can be measured against the phase of the chirp when the chirp reaches the transition frequency.[2] In other words, the transition phase in this case is given by

$$\Delta\phi = \phi_{\rm FID} - \phi_{\rm c}(\omega_{\rm FID}), \tag{3.13}$$

which is evaluated by substituting $\omega_{\rm FID}$ into Eq. 3.12. Explicitly, the phase difference becomes

$$\Delta\phi = \phi_{\rm FID} - \phi_{\rm o} - \frac{1}{2}(\omega_{\rm FID}^2 - \omega_{\rm o}^2)\left(\frac{\Delta\omega}{\Delta t}\right)^{-1}. \tag{3.14}$$

In this way, a measurement of a chirped pulse and the subsequent FID can also be used to determine whether a transition is absorptive or emissive. For example, the FID in Fig. 2-9(c) is determined to be π radians out of phase with the chirp when it sweeps through resonance, which is consistent with an absorptive transition. The details of the phase extraction procedure for both single-frequency and chirped excitation pulses are presented in Sec. 3.3 below.

3.3 Extraction of transition phases

Here the procedure used in extracting transition phases is described in detail. This method is both robust and general. For example, it also applies to rotational transi-

[2]For a linearly chirped excitation, the nonresonant contributions to the phase above and below the resonance frequency cancel, and the phase of the excitation at the resonance frequency determines the phase of the FID.

tions in molecules, since the phase of the transition depends solely on whether there is more initial population in the upper or lower state. (For Rydberg states, only one state in the transition is populated by the lasers, and the initial population is equal to the population difference.) For reference, an overview of the process is presented first in Sec. 3.3.1. Then, a fuller description is given of each aspect: digital filtering of the time traces (Sec. 3.3.2), extracting the phase difference of a single-frequency excitation and FID (Sec. 3.3.3), and extracting the phase difference of a chirped-pulse excitation and FID (Sec. 3.3.4).

3.3.1 Overview of the phase extraction procedure

The general approach is to fit both the excitation pulse (single-frequency or chirped) and the subsequent FID in the time domain and thus determine the phases of each quantitatively. The phases of the pulse and FID may then be appropriately compared to determine whether the transition is absorptive or emissive. The steps:

1. If possible, digitally filter the data trace to remove frequencies that are not in the excitation pulse or FID.

2. Fit the magnitude Fourier transform of the FID in the frequency domain. Extract the frequency and decay rate (linewidth) from the fit.

3. Using the fitted frequency and decay rate, fit the FID in the time domain to determine the phase of the FID.

4. Fit the (single-frequency or chirped) excitation pulse in the time domain.

   (a) If the pulse is resonant and single-frequency, use the same frequency value as that for the fitted FID.

   (b) If the pulse is chirped, a guess of the initial frequency appropriate for the starting time of the chirp must be made.

5. Compute the transition phase (modulo 2π) using Eq. 3.9 for a single-frequency pulse or Eq. 3.14 for a chirped pulse.

3.3.2 Digital filtering

Directly fitting a raw time trace poses problems. Other frequencies present in the spectrometer may interfere with fitting. For example, the 10-MHz phase reference is generally seen in all of the time traces, as are frequencies from other oscillators in the spectrometer. Another issue is that the FID oscillates on a timescale of $\sim$0.1 ns, while the decay of the FID is generally on the order of $\sim$1 μs, a difference of 4 orders of magnitude. The multiple timescales also make it difficult to fit the time trace directly.

When possible, the data trace is digitally filtered before analysis. Filtering is not strictly necessary for the overall phase extraction procedure, but it does simplify the process considerably. Filtering removes other frequencies (such as the 10-MHz standard and the high-frequency noise that results from the excitation pulse being off the scale of the oscilloscope) that are not involved in the analysis of the transition phase, as well as DC. In MATLAB, the Filter Design & Analysis Toolbox (fdatool) is used to create a custom digital filter for each data trace. A finite impulse response (FIR) equiripple filter type (usually a bandpass) is used. An FIR filter has the property that the phase depends linearly on the frequency; $\phi \propto \omega$ is maintained. This property is important because the relationships between the phases at different frequencies are preserved.

3.3.3 Phase extraction for a single-frequency

Given a resonant, single-frequency excitation pulse and FID (digitally filtered or otherwise), such as that in Fig. 2-9(a), the magnitude Fourier-transform of the FID part is taken first. The resulting spectrum is fit in the frequency domain using an appropriate lineshape (usually Gaussian or square-root-Lorentzian) to determine the frequency, ω_{FID}, and decay rate (via the linewidth) of the FID to high precision. (The relations given in Appendix A are useful for converting the fitted linewidth the correct corresponding decay rate.) Then, the FID is fit in the time domain using the known values of the frequency and decay rate. Thus, only the amplitude and phase, ϕ_{FID}, of

the FID need to be fitted. In this way, the fast oscillations of the FID are decoupled from the slower decay rate, and the time trace can be fit more readily.

Once the parameters of the FID have been determined in the time domain, the excitation pulse is fitted in the time domain. This process is straightforward because the pulse is a single sinusoidal oscillation with large S/N. For convenience, the excitation pulse is fit to ω_{FID}, the same frequency as is determined for the FID. (Doing so eliminates the need to consider terms like $\Delta\omega \times \Delta t$ when comparing the phases later on.) So, only the amplitude and phase, ϕ_{pulse}, of the excitation pulse need to be fit in this case as well. With ϕ_{FID} and ϕ_{pulse} both extracted, the phase difference may be determined using Eq. 3.9 by taking $\phi_{\mathrm{FID}} - \phi_{\mathrm{pulse}}$ (modulo 2π), as long as both phases were extracted using the same time axis.

3.3.4 Phase extraction for a chirped pulse

For a chirped excitation, it is sometimes not feasible to filter the time trace for a chirped excitation because of the larger bandwidth, especially if the chirp passes through zero frequency in the detection arm. (In this case, low-frequency noise and DC cannot be filtered.) The phase extraction process, however, is mostly analogous to the case of a single-frequency excitation. All of the parameters of the FID (frequency, decay rate, amplitude, and phase) are determined as for a single frequency pulse.

The chirp is fit to a form like Eq. 3.10. The bandwidth, $\Delta\omega$, and pulse duration, Δt, are known *a priori*, but the amplitude, initial phase, ϕ_{o}, and initial frequency, ω_{o}, of the chirp must be determined through the fit. The value of ω_{o} must be fit because, in general, the chirped pulse will not begin exactly at $t = 0$ on the time axis of the data trace. (This issue is not encountered for single-frequency excitation pulses because the frequency is always the same, and any changes in the time axis only affect the value of ϕ_{o}.) The shift of the initial time of the chirp changes the fitted initial frequency, which is referenced to $t = 0$. Additionally, this time shift must be taken into account when making an initial guess for ω_{o} in order for the fitting process to converge. Having determined all of the parameters of both the FID and the chirp, the phase of the transition may be extracted using Eq. 3.14 as discussed above.

In the case where a chirped pulse excites multiple transitions that have different values of ω_{FID} and ϕ_{FID}, the approach described here may still be employed. As long as a transition in the frequency spectrum is resolved sufficiently that ω_{FID} and ϕ_{FID} can be determined, then each relative phase can be evaluated individually using Eq. 3.14.

Chapter 4

Manipulations of Rydberg quantum states and cooperative dynamics in Rydberg ensembles

First, in Sec. 4.1, I describe two examples of manipulations of Rydberg systems with the CPmmW instrumentation. In the process of the manipulations in Sec. 4.1.2, dynamics due to many-body interactions in the Rydberg ensemble are encountered. This and other cooperative effects are discussed in more detail in Sec. 4.2.

4.1 Manipulations

In this section, I discuss two types of manipulation of Rydberg states that have been performed using sequences of mm-wave pulses: (1) populating high-ℓ Rydberg states with a sequence of short mm-wave pulses (Sec. 4.1.1) and (2) generating mm-wave photon echoes of Rydberg–Rydberg transitions (Sec. 4.1.2).

4.1.1 Populating high-ℓ states with pulse sequences

Along with the large transition dipole moments, the easily controlled, phase coherent mm-wave source allows for manipulation of Rydberg states. For example, the $54.0h$

state is populated by a sequence of three pulses, as shown in Fig. 4-1. The $55.8d$

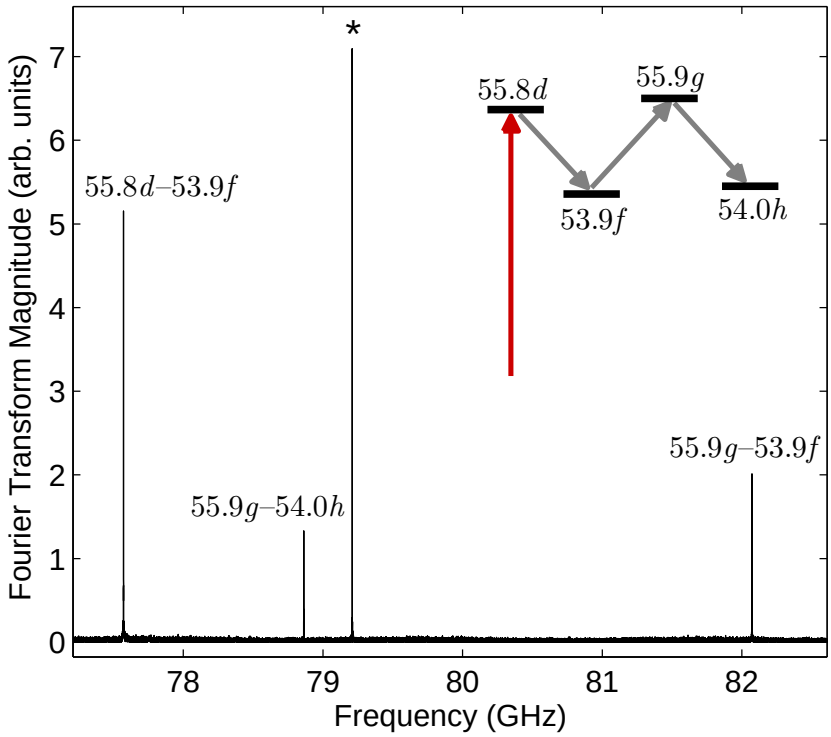

Figure 4-1: One spectrum contains each $\ell \rightarrow \ell + 1$ excitation step in the multiple-component-pulse population of the $54.0h$ state. The inset shows a schematic of the four energy levels and three transitions that contribute to the spectrum. The $55.8d$ state is initially populated by the lasers (long, red arrow). Sequential, resonant mm-wave pulses (gray arrows) then excite the $55.8d$–$53.9f$ transition at 77.5720 GHz, the $55.9g$–$53.9f$ transition at 82.0725 GHz, and the $55.9g$–$54.0h$ transition at 78.8625 GHz. Since no pulse area is chosen to be an integer multiple of π, each transition undergoes FID and therefore appears in the frequency spectrum. A known artifact (marked with an asterisk) is due to the the fixed-frequency 3.96-GHz oscillator of the mm-wave spectrometer.

state is initially populated by the laser radiation. Subsequent mm-wave pulses of 77.5720 GHz, 82.0725 GHz, and 78.8625 GHz each transfer some of the population into $53.9f$, $55.9g$, and $54.0h$, respectively. Because no pulse in the excitation sequence caused an integer multiple of π polarization, at each step there is both FID signal and population transfer. Thus, each mm-wave transition in the $\ell \rightarrow \ell + 1 \rightarrow \ell + 2$ transition sequence appears in a single spectrum.

A restriction of this approach for creating states of high angular momentum is that

all of the Rydberg–Rydberg transitions must fall within the excitation bandwidth of the CPmmW spectrometer. For example, the current CPmmW spectrometer can cover 70–84 GHz in one configuration, so all transitions must be within the ≈15 GHz centered around 77 GHz, or within about ±10% of the center of the frequency range. Core-nonpenetrating Rydberg states all have quantum defects that are approximately zero; thus the transitions between these states will have similar frequencies, and groups of such transitions are more likely to fall within a given window of excitation bandwidth. The core-penetrating states do not have near-zero quantum defects, and the frequencies of Rydberg–Rydberg transitions change significantly as ℓ increases (for a given n^*) and the Rydberg states become more nonpenetrating. One way to increase the usable number of groups of levels would simply be to increase the excitation bandwidth of the CPmmW spectrometer. Additionally, the Rydberg level spacings decrease as $(n^*)^{-3}$, so appropriate groups of levels are more likely available at higher n^* using $|\Delta n^*| > 1$ transitions, as in Fig. 4-1.

4.1.2 Photon echoes of Rydberg–Rydberg transitions

In addition to populating states of high angular momentum, photon echoes of the $34.13p$–$33.67s$ transition have been observed. These experiments are analogous to the well-established spin-echo method of NMR spectroscopy [31], and one example is shown in Fig. 4-2. Initially a 10-ns, single-frequency pulse with 2 μW of power $\pi/2$-polarizes the transition. The resulting FID decays (mostly) inhomogeneously due to Doppler and Zeeman broadening. After a waiting time τ, a π pulse—the same power as the $\pi/2$ pulse but twice the duration—is applied.[1] The π pulse reverses the inhomogeneous components of the phase evolution, and during another period of length τ, the FID revives (incompletely), then dephases again.

A time series of photon echoes of the same transition is shown in Fig. 4-3 for τ values of 2.0, 2.4, and 2.8 μs. The measured phase difference between each echo

[1]The active multipliers in the mm-wave spectrometer generate a fixed power level, while the variable attenuator is adjusted mechanically and cannot be tuned on the μs timescale. Thus, the pulse areas in a sequence of pulses must be controlled by setting the duration of each pulse.

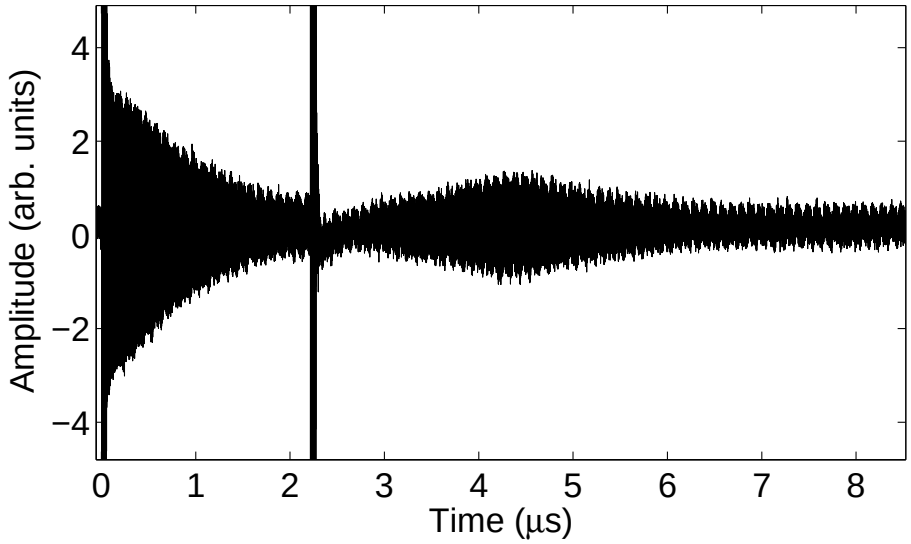

Figure 4-2: Rydberg mm-wave Photon Echo. A 10-ns $\pi/2$ pulse initially polarizes the $34.13p$–$33.67s$ transition, and most of the dephasing of the FID is inhomogeneous. At 2.2 μs, a 20-ns π pulse is applied, which reverses the inhomogeneous dephasing. After another 2.2 μs, a fraction of the FID recovers. The decrease of the echo amplitude (relative to the initial FID) is determined primarily by the superradiant decay rate [18, 77, 48, 70, 86] of this system. The dip in the signal immediately after the π pulse ends is due to the pulse saturating the amplifier on the detection arm of the spectrometer. Fine modulation is an artifact that arises from the 10-MHz phase reference in the frequency downconversion step.

and initial FID (extracted using an approach similar to the one discussed in Sec. 3.3) is π radians, which is consistent with the π pulse inverting the two-level system. The amplitude of the echo is determined by the extent of the homogeneous decay over the $\approx 2\tau$ interval. If the homogeneous decay rate were negligible (that is, the decay of the FID were completely inhomogeneous), then the amplitude of the echo would be equal to that of the initial FID. Conversely, in the case of a purely homogeneous decay, there would be no rephasing at all. Assuming an exponential decay of the echo amplitude relative to the FID amplitude,

$$\frac{A_{\text{echo}}}{A_{\text{FID}}} = e^{-t/\text{T}_{\text{hom}}}, \tag{4.1}$$

where A_{echo} is the amplitude of the echo and A_{FID} is the initial amplitude of the FID, the homogeneous decay constant of the echoes, T_{hom}, was determined to be

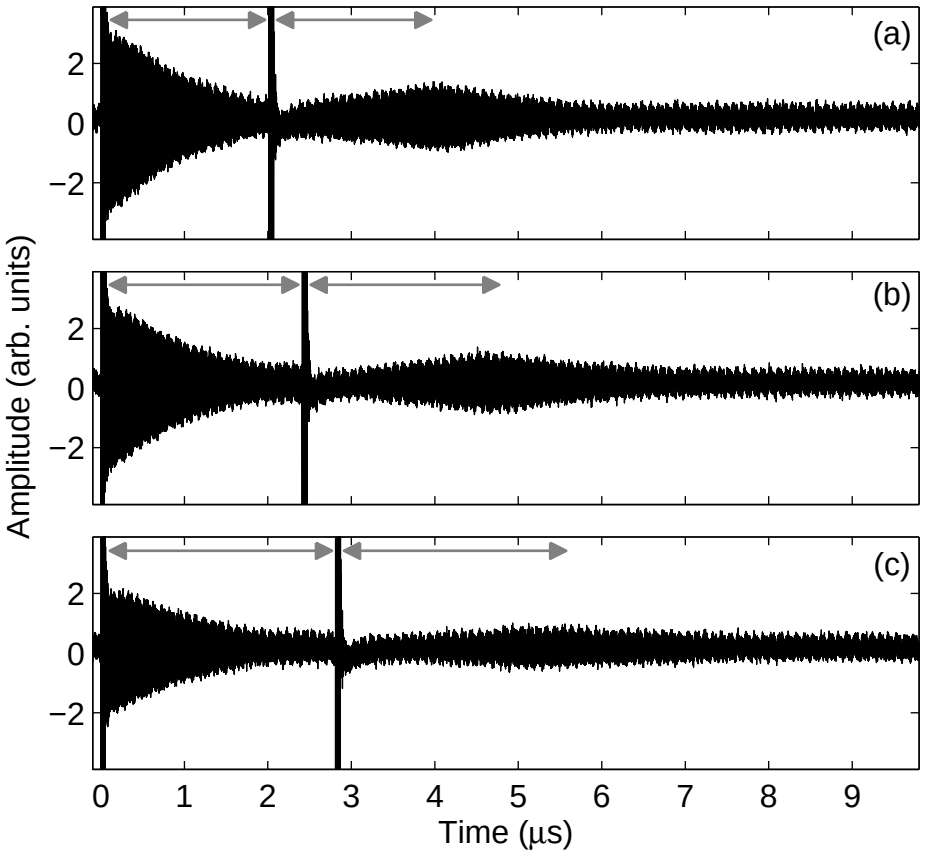

Figure 4-3: Photon echoes are observed at a series of delay times. Photon echoes of the 34.13p–33.67s transition are collected with waiting times, τ, of (a) 2.0 μs, (b) 2.4 μs, (c) and 2.8 μs. In each panel, rephasings are observed at time $\sim 2\tau$. The horizontal arrows indicate the value of τ for each time trace. The echo amplitude in panel (c) is commensurate with that of the initial FID.

4.6 ± 0.5 μs. The cause of this homogeneous decay constant, which is discussed in detail in Sec. 4.2.1 below, is superradiance.

4.2 Cooperative effects and superradiance

In optically thick systems, emitters in the sample are coupled together through the radiation field and behave cooperatively. In general, cooperative effects become more

important as the "cooperativity parameter," given by [85, 84]

$$C = \frac{N\lambda^3}{4\pi^2}, \tag{4.2}$$

becomes larger. Here, N is the number density in the sample and λ is the emission wavelength. The physical interpretation of this parameter is simply the number of emitters that are in a region that is the size of the emission wavelength. The more emitters there are in such a region, the more significant near-field coupling becomes. In the case of mm-wave radiation, λ is significantly larger than the average interatomic spacing in a supersonic jet expansion, even at comparatively low number densities. For example, in conditions typical of CPmmW Rydberg–Rydberg experiments, $N \sim 10^5$ emitters cm^{-3} and $\lambda = 4$ mm, giving $C \sim 10^2$ emitters. Thus, it is reasonable to expect significant, observable cooperative effects in mm-wave measurements of Rydberg–Rydberg transitions.

One example of a cooperative effect is superradiance, where intense, collective emission occurs with a rate that is N times faster than spontaneous emission [18, 77, 48, 27, 29, 57, 84, 70, 86, 15]. A situation where superradiance may occur is illustrated in Fig. 4-4. In the case of typical fluorescence, shown in Fig. 4-4(a), the emission lifetime may be determined by the spontaneous emission rate. However, in Fig. 4-4(b), multiple emitters are in a region that is the size of the emission wavelength λ. The ensemble behaves like one emitter with an intensity N times greater than the spontaneous emission rate. The emission lifetime is correspondingly N times shorter, conserving the radiated energy. (A more detailed description of superradiant decay is given in Sec. 4.2.1 below.)

With their enormous transition dipole moments and associated low-frequency (long-wavelength) transitions, Rydberg systems may exhibit many cooperative effects. In this section, I first discuss examples of superradiant decay that is observed indirectly in photon echoes (Sec. 4.2.1) and directly in FID (Sec. 4.2.2). Then, I discuss other consequences of cooperative effects that are expected to be manifest in Rydberg–Rydberg CPmmW experiments (Sec. 4.2.3).

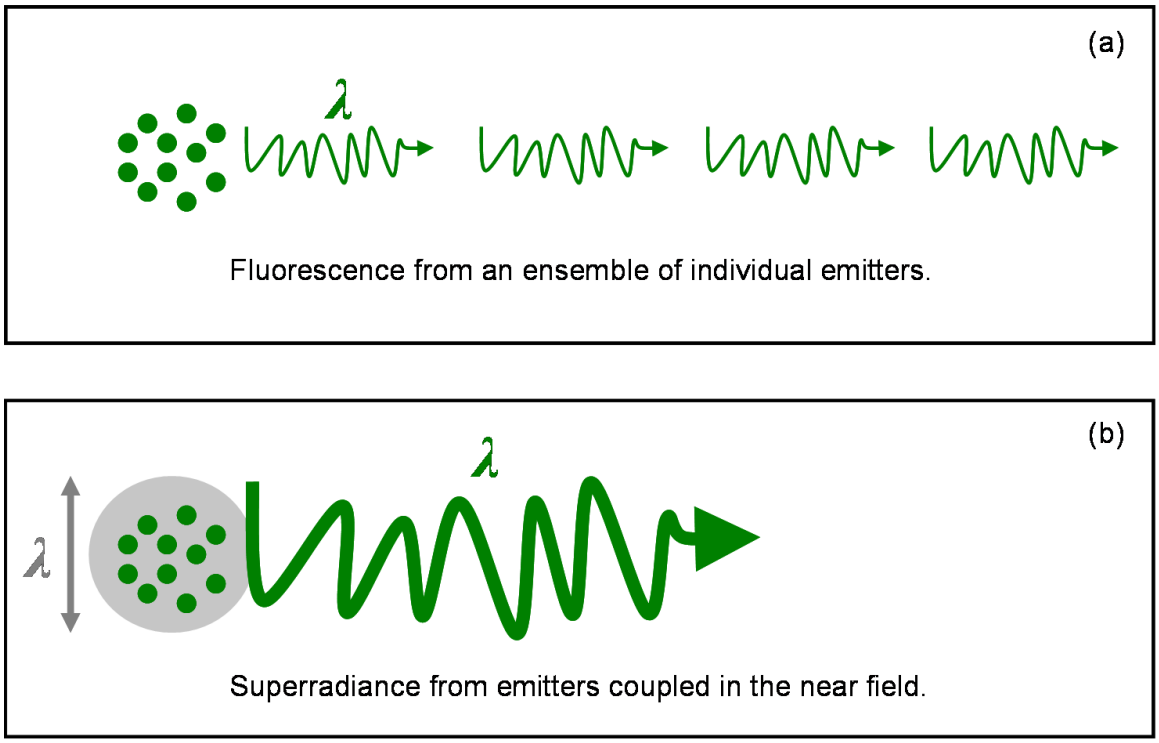

Figure 4-4: Typical fluorescence versus superradiant emission. (a) An ensemble of independent emitters (green circles) fluoresce at a wavelength λ. The temporal distribution of the emission (indicated by thin, curly arrows) may be governed by, for example, the spontaneous emission lifetime of the fluorescent state. (b) Since the emitters are close together on the scale of the emission wavelength (indicated by the gray region), they are coupled together by near-field interactions and thus are no longer independent. The resulting superradiant emission (thick, curly arrow) is more intense by a factor of the number density, N, and the lifetime is shorter by the same factor of N.

4.2.1 Superradiant decay of photon echoes

The photon echo experiments discussed in Sec. 4.1.2 have a homogeneous decay constant of 4.6 μs. The possible sources of homogeneous decay are transit time of the jet expansion, blackbody radiation from the surrounding apparatus, collisional dephasing from the dipole–dipole interaction, and cooperative radiation of the Rydberg emitters (superradiance). Each plausible decay mechanism is analyzed in order to show that superradiance is the dominant effect.

The first consideration is the transit time of the calcium emitters through the field of view of the apparatus, which is depicted in Fig. 4-5. The field of view of the

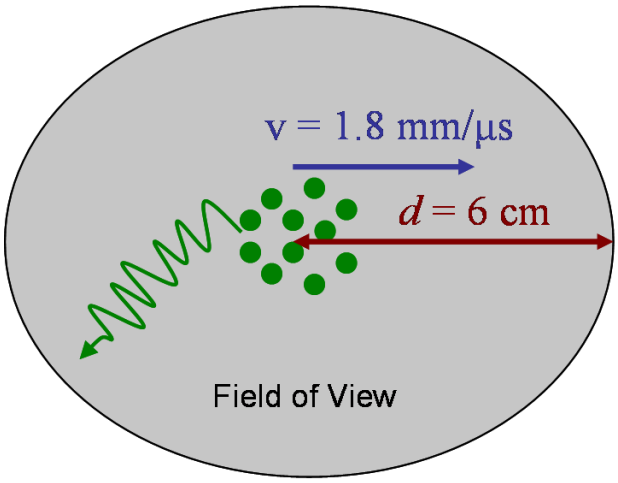

Figure 4-5: Pictorial representation of transit-time broadening in the photon echoes of the 34.13p–33.67s transition. The Rydberg emitters (green circles) reside in the center of the field of view (large gray oval) and emit FID (green, curved arrow). The edge of the field of view is 6 cm (red double-arrow) from the emitters. Seeded in a jet expansion of helium atoms, the emitters travel at a velocity (blue arrow) of 1.8 mm/μs. The loss of emitters from the field of view will cause decay of the FID signal observed at the detection horn.

detection horn is 12 cm wide, and the velocity of Rydberg atoms in the helium jet expansion under typical conditions is $v = 1.8$ mm/μs. The average transit time from the center of the interaction volume over a distance d is thus given by

$$\mathrm{T_{tt}} = \frac{d}{v}. \tag{4.3}$$

In this case, $d = 6$ cm, and the transit time is estimated to be $\mathrm{T_{tt}} = 33$ μs, which is more than 7 times greater than the observed 4.6-μs homogeneous decay time. Thus, the transit time of the calcium emitters does not contribute significantly to the homogeneous decay.

In the case of blackbody radiation, homogeneous decay occurs in two ways: (1) the blackbody field incoherently excites the observed transition, directly causing dephasing, and (2) the field moves population out of a state involved in the transition, decreasing the observed transition intensity. Both decay processes are illustrated in Fig. 4-6. For mechanism (1), the direct dephasing rate of a given transition by

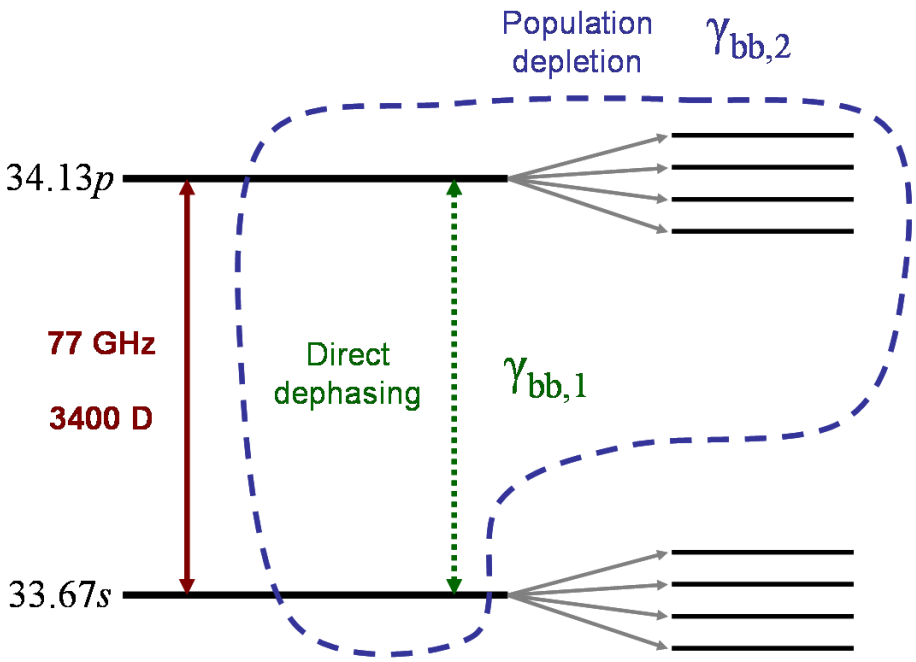

Figure 4-6: Blackbody-induced dephasing mechanisms in the 34.13p–33.67s transition. The coherence that generates the FID is indicated by the red double-arrow. Resonant blackbody photons may dephase the transition directly (green, dotted double-arrow) with a rate of $\gamma_{bb,1}$. Blackbody radiation may also incoherently drive population out of either state (into other states as well as the 33.67s state), causing a loss of FID signal. This process has a rate of $\gamma_{bb,2}$ and is labeled for only the 34.13p state for simplicity (blue, dashed curve). The contribution of $\gamma_{bb,1}$ is contained in that of $\gamma_{bb,2}$.

blackbody radiation is (Ref. [21], pp. 53–54)

$$\gamma_{bb,1} = \frac{4\pi kT}{3\epsilon_o c^3}\left(\frac{\mu\nu}{\hbar}\right)^2, \tag{4.4}$$

where k is the Boltzmann constant and T is the temperature. For the 34.13p–33.67s transition at 295 K, $\gamma_{bb,1} = 5$ kHz. As for mechanism (2), the blackbody field depopulates each Rydberg state at an approximate rate of

$$\gamma_{bb,2} = \frac{4\alpha^3 kT}{3\hbar(n^*)^2}, \tag{4.5}$$

where α is the fine structure constant. For states with $n^* \approx 34$, the population depletion rate is $\gamma_{bb,2} \approx 17$ kHz. Both levels undergo this loss of population. The

contribution from $\gamma_{\mathrm{bb},1}$ in Eq. 4.4, however, is implicitly present in Eq. 4.5 (see Fig. 4-6). To avoid counting $\gamma_{\mathrm{bb},1}$ twice, the total contribution of blackbody radiation to the homogeneous decay is estimated to be

$$\gamma_{\mathrm{bb}} = 2\gamma_{\mathrm{bb},2} - \gamma_{\mathrm{bb},1}, \tag{4.6}$$

which gives an overall blackbody dephasing time of $\mathrm{T}_{\mathrm{bb}} = \gamma_{\mathrm{bb}}^{-1} = 34\ \mu$s. As is the case for the transit time, the blackbody dephasing time is significantly longer than the observed 4.6 μs homogeneous decay time.

The large dipole moments of Rydberg–Rydberg transitions also dephase each other at long range, and the expected homogeneous dephasing rate from the dipole–dipole interaction is (Ref. [2], pp. 140–146)

$$\gamma_{\mathrm{dd}} = \frac{\pi\mu^2 N}{4\epsilon_{\mathrm{o}}\hbar}. \tag{4.7}$$

Here, N is the number density of Rydberg states. By comparison, the superradiant decay rate [77, 48] is

$$\gamma_{\mathrm{SR}} = \frac{\pi\mu^2 N}{3\epsilon_{\mathrm{o}}\hbar}\frac{L}{\lambda}, \tag{4.8}$$

where λ is the wavelength of the radiation, and L is the path length of radiation through the sample. The expression for the superradiant decay rate is substantially similar to that for the dipole–dipole dephasing, *except for an additional factor of* $\sim L/\lambda$. In the current experimental geometry, this factor is large because L is at least 7 cm ($\approx 18\lambda$ for the $34.13p$–$33.67s$ transition). Thus, the superradiant decay is expected to be more than 20 times faster than the dipole–dipole dephasing, and thus the dipole–dipole interaction does not contribute significantly to the observed homogeneous decay.

On the other hand, assuming that the observed 4.6 μs homogeneous decay time is entirely due to cooperative effects, Eq. 4.8 gives a corresponding Rydberg number density of $N = 8 \times 10^4/\mathrm{cm}^3$. This estimate is at the lower end of the previous determinations of the number density in the experimental apparatus, including that

from transient nutations discussed in Sec. 3.1.3. Thus, any reasonable number density of Rydberg emitters fully accounts for the homogeneous decay rate that is observed. The conclusion, then, is that the homogeneous decay of the photon echoes in Figs. 4-2 and 4-3 is primarily due to superradiance.

4.2.2 Direct observation of superradiance in FID

If the number density of Rydberg emitters is sufficiently high, then superradiance (Eq. 4.8) may become the dominant decay mechanism, which would then be directly observable in the FID of Rydberg–Rydberg transitions. Fig. 4-7 shows such an example of superradiant decay in the $34.13p$–$33.67s$ transition. In this case, the pulsed photoablation source was optimized to yield as many calcium Rydberg atoms as possible, and a short run (5000 averages) of data was collected while the calcium atom source remained at peak conditions.

The mm-wave power in this experiment was optimized to give the maximum FID amplitude, which should correspond to a pulse area of $\pi/2$. However, the transient nutation in Fig. 4-7 passes through a minimum and then starts to increase, unlike the $\pi/2$ pulse in Fig. 3-2(a). The shape of the transient nutation is not consistent with a pulse area of $\pi/2$, and this anomalous behavior indicates the presence of another dynamical process.

Fig. 4-7(1) shows the magnitude Fourier transform of the entire FID. The broad line has a square-root-Lorentzian lineshape (see Appendix A), which indicates a homogeneous decay process and is consistent with superradiance. The linewidth is consistent with the superradiant decay rate, based on Eq. 4.8, that is expected for the $34.13p$–$33.67s$ transition at a number density of approximately 10^6 Rydberg emitters/cm^3, which is a reasonable number density for the current apparatus (see Sec. 3.1.3). The splittings at the center of the line are consistent with Zeeman splittings due to the ambient magnetic fields in the vacuum chamber.

Fig. 4-7(2), on the other hand, contains the magnitude Fourier transform without the early part of the FID. Since the superradiant decay in this case is much faster than the Doppler dephasing (the next-fastest decay mechanism), the superra-

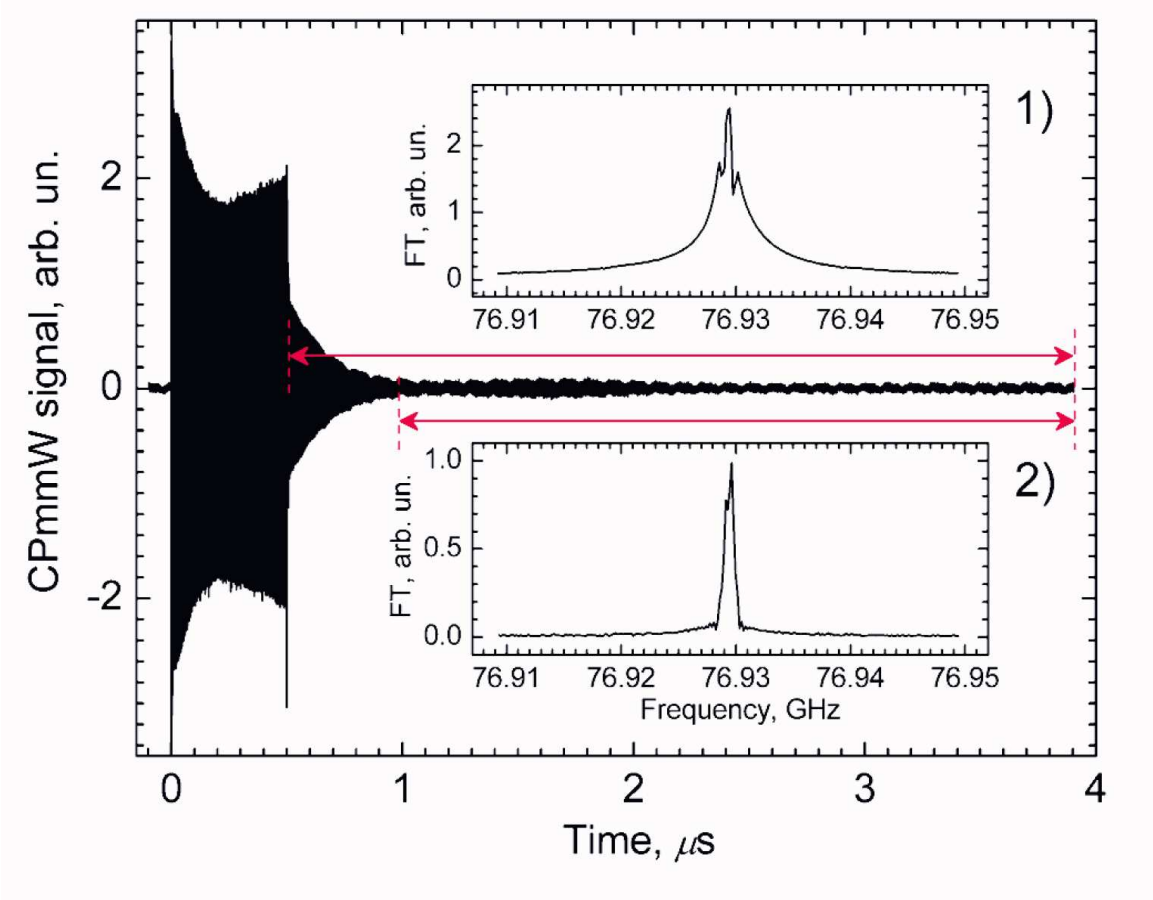

Figure 4-7: Superradiant decay is observed directly in the calcium $34.13p$–$33.67s$ transition. The FID amplitude is optimized experimentally; however, the shape of the nutation is not consistent with a $\pi/2$ pulse area. Inset (1) contains the magnitude Fourier transform of the entire FID (time window indicated by the upper, red double-arrow). The envelope of the lineshape appears square-root-Lorentzian, which indicates a homogeneous decay process, and the linewidth is consistent with the superradiant decay rate expected from 10^6 Rydberg emitters/cm^3. The line splittings are consistent with the stray magnetic fields in the chamber. Inset (2) contains the magnitude Fourier transform without the early part of the FID (time window indicated by the lower, red double arrow). The lineshape appears Gaussian, with the linewidth due to the Doppler broadening that is typical of the pulsed jet expansion. The two insets are different because the superradiant component of the FID decays more quickly, leaving behind the Doppler-dominated FID in the latter part of the time trace.

diance has already finished before the time window in Fig. 4-7(2) starts. Thus, the Doppler-dominated component remains in the frequency spectrum, with the expected lineshape and a linewidth that is typical of the Doppler dephasing observed in the pulsed jet expansion.

The presence of two different decay mechanisms in Fig. 4-7, with one mechanism dependent on the number density of emitters and the other not, indicates that the Rydberg sample is inhomogeneous. If the sample had a high, uniform number density of Rydberg emitters, then a single, superradiant decay rate would be expected for the emission from the sample. Inhomogeneity in the number density of the Rydberg sample likely comes from two sources: (1) variations in the photoablation source and (2) non-uniformity of the beam profiles of the pulsed dye lasers.

4.2.3 Further consequences of cooperative effects

As shown in Secs. 4.2.1 and 4.2.2 above, cooperative effects have both direct and indirect effects that are observable with the CPmmW technique. For the purpose of acquiring FID spectra, it is noteworthy that superradiance is a radiative decay mechanism; therefore, the amount of signal collected should not diminish as the superradiant decay rate increases. However, the increased decay rate causes the lines in the frequency domain to broaden, as is the case in Fig. 4-7. Thus, the precision of line frequencies in the spectrum may not improve as a sample becomes more strongly superradiant because the absolute frequency precision, $\Delta\nu$, scales as [67, 13]

$$\Delta\nu \propto \frac{\mathrm{S/N}}{\Gamma}, \tag{4.9}$$

where Γ is the full width at half maximum of the spectral feature. Both S/N and Γ are linearly proportional to N for superradiant decay, and so $\Delta\nu$ would not be expected to decrease with increasing Rydberg number density.

Since superradiant Rydberg samples interact strongly with electromagnetic radiation, the FID from an excitation pulse can also, in turn, act as a driving field within the sample. This self-driving FID should also have observable consequences. A self-

induced AC Stark shift [86] of ∼100 kHz is predicted at number densities $\gtrsim 10^6$ Rydberg emitters/cm^3. This effect is similar in origin to the AC Stark shift that occurs when Rydberg states are in the presence of a blackbody field (Ref. [21], pp. 55–56). Another effect is that the modulation of the resonance by the Rabi frequency, which causes the Mollow triplet [58], could perturb the observed lineshapes—especially if the Rydberg sample is spatially inhomogeneous. Splittings of around 500 kHz are expected at number densities $\gtrsim 10^6$ Rydberg emitters/cm^3 for this process. A dynamical prediction of cooperative interactions is that long-lived coherences should persist via the collective radiation field in a Rydberg sample if superradiant decay is the next-fastest decay process after Doppler dephasing [86]. These coherences should be measurable using the photon echo method that is described in Secs. 4.1.2 and 4.2.1 above.

For the strongest, $|\Delta n^*| \leq 1$ transitions, the dipole moment term in Eq. 4.8 scales as

$$\mu^2 \propto (n^*)^4, \tag{4.10}$$

while, for the wavelength term,

$$\frac{1}{\lambda} \propto (n^*)^{-3}. \tag{4.11}$$

So overall, the superradiant decay varies according to

$$\gamma_{\mathrm{SR}} \propto n^*. \tag{4.12}$$

Thus, the strength of the cooperative effects may be *tuned* by changing n^*. Since the cooperative effects also scale linearly with the number density of Rydberg states, a higher-density source will allow for a more systematic investigation of these effects.

One such example of a more intense source is a collisional cooling photoablation beam source [56, 50, 66]. A further advantage of a collisional cooling source is that it is expected to yield a more homogeneous sample than the current photoablation source. Higher sample uniformity will be important in the measurement of cooperative effects because of their dependence on number density. Additionally, the effects

of superradiance may be studied systematically with this source, since the number density of Rydberg emitters will be trivially tunable by adjusting the power of the pulse dye lasers used to generate the Rydberg states.

Chapter 5

Methods for robust population transfer in Rydberg states: Adiabatic rapid passage and composite pulses

In this chapter, I discuss simulations of mm-wave methods for manipulating Rydberg systems by robustly transferring population between Rydberg states—that is, moving population both with high efficiency and with tolerance of mm-wave field inhomogeneity. The desired scheme of sequential excitation is outlined in Sec. 5.1. Two methods for high-efficiency population transfer that utilize the capabilities of the arbitrary waveform generator are simulated: adiabatic rapid passage (Sec. 5.2) and composite pulses (Sec. 5.3). Prospects for experimental implementation of these techniques are addressed in Sec. 5.4.

5.1 Sequential excitation of Rydberg states with mm-wave pulses

In Fig. 4-1, a sequence of resonant mm-wave pulses was used to generate Rydberg states of high orbital angular momentum ($\ell \geq 4$) and to observe a transition between two high-ℓ (g and h) states. One particular application for producing high-ℓ states is the spectroscopy of molecules in core-nonpenetrating Rydberg states (see Sec. 7.3). However, powerful manipulation of Rydberg states, in particular robust population transfer through multiple excitation steps, is required for this application. Such a desired mm-wave excitation process is depicted in Fig. 5-1. High efficiency is necessary

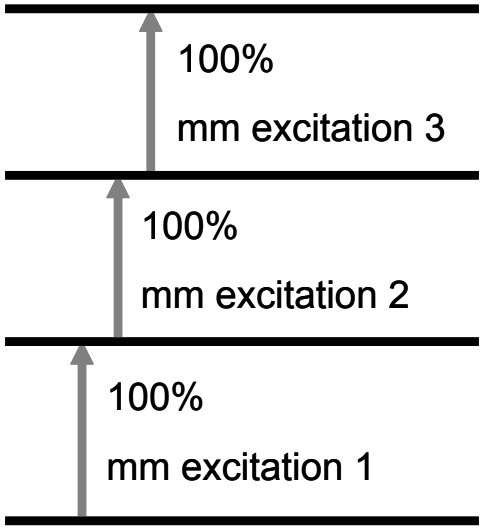

Figure 5-1: A desired multi-step mm-wave excitation sequence for Rydberg states. The mm-wave excitations (gray arrows) move all of the population from one state to the next sequentially. Such a scheme would allow for spectroscopy of high-ℓ Rydberg states.

because, if the transfer efficiency in each excitation step is $\lesssim 50\%$, then an insufficient number of Rydberg emitters will be present in the final state to be able to observe FID signal after several excitation steps. Losses may result from inexact mm-wave pulse areas (via the combination of mm-wave power and pulse duration) and from inhomogeneity of the mm-wave beam. With these losses, simply applying multiple π pulses to transfer population to high-ℓ states is not feasible for multi-step excitation

sequences. Since, in practice, mm-wave field inhomogeneity may be difficult to avoid, a high-efficiency population transfer process that has some tolerance of variation of the mm-wave power is also desirable.

5.2 Adiabatic rapid passage

Adiabatic sweeps are an established technique in nuclear magnetic resonance (NMR) spectroscopy for robustly inverting the population of a 2-level system [38, 5]. In this technique, the frequency of a pulse is swept through resonance slowly and while maintaining strong coupling of the 2 levels via the field. The strong coupling causes an avoided crossing in the eigenstates of the matter + field Hamiltonian, which results in complete transfer of the population from the initial state to the final state. Advantages of this approach are that transfer of population may have unit efficiency while not being strongly dependent on the power used in the sweep. Thus, adiabatic rapid passage may still be effective even when the excitation field has an inhomogeneous profile. Adiabatic rapid passage has also been performed in Rydberg states by Stark-sweeping Rydberg–Rydberg transition resonance frequencies [73] and by using short, chirped microwave pulses to cause adiabatic rapid passage through many transitions [39, 49].

The Hamiltonian that is used for simulations of adiabatic rapid passage is described in Sec. 5.2.1. The eigenstates of this Hamiltonian and the process of population transfer are discussed in Sec. 5.2.2. The criteria that must be satisfied to achieve adiabatic rapid passage are articulated in Sec. 5.2.3. Simulations of adiabatic rapid passage in Rydberg states are presented in Sec. 5.2.4.

5.2.1 Hamiltonian for adiabatic rapid passage

In this chapter, the Rabi frequency of the interaction of the system with electric field of the mm-waves is given by

$$\Omega = \frac{\mu\ \varepsilon}{\hbar}. \tag{5.1}$$

Here, the Ω notation for the Rabi frequency is used instead of that of Eq. 3.2. This choice is to emphasize the different application of adiabatic rapid passage. Since the active frequency multipliers of the mm-wave spectrometer output a fixed power over their operational range (see Sec. 2.2), the Rabi frequency in this case does not vary with time. Though, in general, Ω may be time-dependent.

The 2-level Hamiltonian used for the simulations of adiabatic rapid passage is [83]

$$\mathbf{H}(t) = \frac{\hbar}{2} \begin{pmatrix} 0 & \Omega \\ \Omega & 2\Delta(t) \end{pmatrix}. \tag{5.2}$$

For simplicity, the 2 states of Eq. 5.2 are labeled $|1\rangle$ and $|2\rangle$. The rotating wave approximation has been made. That is, only mm-wave frequencies near resonance are considered. Also, Eq. 5.2 is a matter + field Hamiltonian, so state $|1\rangle$ is not associated with any excitation, while state $|2\rangle$ is associated with 1 quantum of excitation by the mm-wave field. Thus, in Eq. 5.2 the diagonal element of state $|2\rangle$ is the difference between the mm-wave frequency and the resonant frequency: the detuning,

$$\Delta(t) = \frac{E_2 - E_1}{\hbar} - \omega(t). \tag{5.3}$$

Here, E_2 and E_1 are the absolute energies of states $|2\rangle$ and $|1\rangle$, respectively. Also, $\omega(t)$ is the time-varying angular frequency of the mm-wave field. For convenience, state $|1\rangle$ it is taken to have a detuning of 0 because it is not associated with any excitation.

If the radiation field were also treated in the Hamiltonian in Eq. 5.2, then it would be in a "dressed state" representation [7]. For simulating adiabatic rapid passage, the Hamiltonian used here is more convenient than one using chirped, off-diagonal, oscillating electric fields to couple states $|1\rangle$ and $|2\rangle$. In the current approach, the amplitude of the interaction is a (constant) off-diagonal matrix element. The diagonal element is the time-varying detuning, which corresponds to a frequency-swept mm-wave pulse. For an extension of the Hamiltonian in Eq. 5.2 to include more than 2 states, see Chapter 6.

5.2.2 Eigenstates and population transfer

The eigenstates of the Hamiltonian in Eq. 5.2 are [83]

$$|+\rangle = \sin\Theta|1\rangle + \cos\Theta|2\rangle \tag{5.4a}$$

$$|-\rangle = \cos\Theta|1\rangle - \sin\Theta|2\rangle, \tag{5.4b}$$

where the mixing angle Θ is given by

$$\tan 2\Theta = \frac{\Omega}{\Delta(t)}. \tag{5.5}$$

If, for example, a 2-level system begins completely in state $|1\rangle$, and the mm-waves are activated, but far from resonance ($\Delta(t)$ is positive and very large), then the system is in eigenstate $|-\rangle$. As the mm-waves are brought toward resonance ($\Delta(t)$ decreases), the mixing angle increases toward $\pi/2$. As the mm-waves pass through resonance, the sign of $\Delta(t)$ changes, and the magnitude of $\Delta(t)$ again begins to increase. Once the detuning becomes very large (compared to Ω) and negative, eigenstate $|-\rangle$ becomes composed completely of state $|2\rangle$. The mm-wave field may then be turned off, and the population of the system has been inverted while remaining in one matter + field adiabat throughout the process. Hence, the terminology of "adiabatic rapid passage" is used for this type of population transfer.

5.2.3 Criteria for adiabatic rapid passage

There are three criteria for achieving high-efficiency adiabatic rapid passage. The rules presented here are analogous to the parameters for adiabatic sweeps discussed in Ref. [73].

1. The mm-wave sweep must be a true sweep, not a broadband pulse. That is,

$$\Delta\omega \gg \Delta\omega_{\mathrm{FT}}, \tag{5.6}$$

where $\Delta\omega$ is the bandwidth (in angular frequency units) of the mm-wave pulse,

and $\Delta\omega_{\mathrm{FT}}$ is the Fourier-transform-limited bandwidth of a pulse with the same duration, Δt, as the mm-wave pulse. If the mm-wave pulse is not a true sweep, then the mixing angle (Eq. 5.5) cannot fully change from 0 to $\pi/2$.

2. The mm-wave sweep must begin and end far from resonance. More specifically,

$$|\Delta_i|, |\Delta_f| \gg \Omega, \tag{5.7}$$

where Δ_i and Δ_f are the initial and final detunings of the mm-wave pulse, respectively. If the mm-wave pulse is turned on too close to resonance, which is determined by the Rabi frequency, then the $|+\rangle$ and $|-\rangle$ eigenstates will be mixtures of states $|1\rangle$ and $|2\rangle$ as soon as the mm-wave pulse arrives. Thus, complete conversion from one zeroth-order state to the other will not be possible.

3. The sweep must satisfy the adiabaticity requirement [83]:

$$\left(\Omega^2 + \Delta(t)^2\right)^{3/2} \gg \left|\frac{\partial\Omega}{\partial t}\Delta(t) - \Omega\frac{\partial\Delta(t)}{\partial t}\right|. \tag{5.8}$$

Because the active multipliers generate a fixed power level, Ω in this case does not vary with time. So, Eq. 5.8 becomes

$$\frac{\left(\Omega^2 + \Delta(t)^2\right)^{3/2}}{\Omega} \gg \left|\frac{\partial\Delta(t)}{\partial t}\right|. \tag{5.9}$$

For the special case of a linear frequency sweep, the rate of change of the detuning is (the negative of) the sweep rate of the mm-wave pulse, $\Delta\omega/\Delta t$. Thus, Eq. 5.9 simplifies to

$$\frac{\left(\Omega^2 + \Delta(t)^2\right)^{3/2}}{\Omega} \gg \left|\frac{\Delta\omega}{\Delta t}\right|. \tag{5.10}$$

If the sweep is too fast—especially when the frequency of the mm-wave field is close to resonance—then strong coupling of states $|1\rangle$ and $|2\rangle$ will not be maintained as the frequency is tuned through resonance and the population transfer

efficiency will decrease. An occasionally useful approximation to Eq. 5.10 is [73]

$$\Omega^2 \gg \left| \frac{\Delta\omega}{\Delta t} \right|, \tag{5.11}$$

which neglects the contribution of the detuning to the adiabaticity criterion. However, it is noteworthy that, in some cases, decreasing the sweep rate of the pulse near resonance may be an effective strategy for satisfying the adiabaticity criterion in Eq. 5.10.

5.2.4 Simulations of adiabatic rapid passage in Rydberg–Rydberg transitions

To simulate the adiabatic rapid passage of Rydberg state populations due to mm-wave excitation, the time-dependent Schrödinger equation,

$$i\hbar \frac{\partial \Psi(t)}{\partial t} = \mathbf{H}(t)\Psi(t). \tag{5.12}$$

is integrated numerically using the Hamiltonian matrix in Eq. 5.2 for parameters that correspond to conditions that are experimentally plausible. Since the Hamiltonian is a matrix, $\Psi(t)$ in Eq. 5.12 is a vector of coefficients for states $|1\rangle$ and $|2\rangle$. The system population begins entirely in state $|1\rangle$.

The adiabatic frequency sweeps simulated below are for a 5-kD electric dipole transition moment, which is typical of $|\Delta n^*| \leq 1$ Rydberg–Rydberg transitions of n^* around 45. The initial and final detunings of the sweep are (in linear frequency units) $\Delta_i = -1$ GHz and $\Delta_f = +1$ GHz, respectively. Thus, the bandwidth of the sweep is $\Delta\omega/2\pi = 2$ GHz, with the resonance at the center of the frequency sweep. The duration of each pulse is 500 ns, and the pulse in the simulation turns on shortly after $t = 0$.

A simulation is shown in Fig. 5-2 for a linear frequency sweep with 10 μW of power. The small-amplitude oscillations that are visible as soon as the mm-wave pulse turns on are due to the pulse being not fully off resonance at this power level

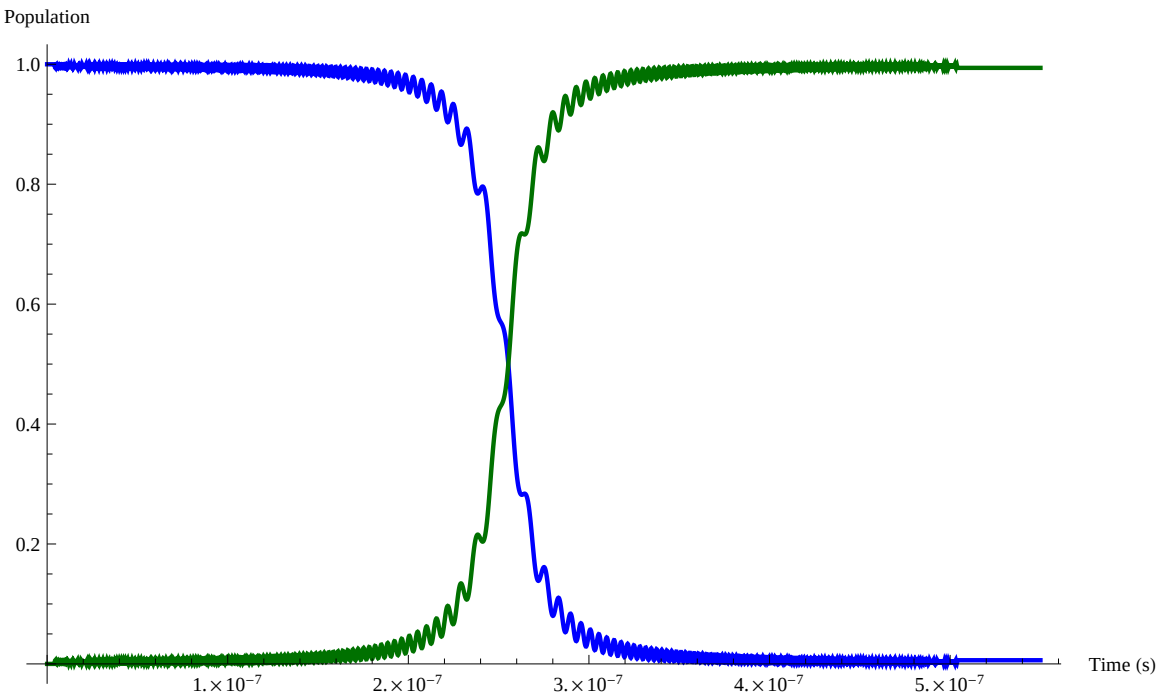

Figure 5-2: A linear frequency sweep adiabatically inverts the populations of a 2-level Rydberg system of $n^* \approx 45$. This simulation is for 10 μW of power and an electric dipole transition moment of 5 kD. Even at an initial detuning of -1 GHz, there is still some coupling of the 2 states when the pulse turns on at this power, which causes the small amplitude oscillations at the beginning of the trace. As the frequency of the sweep nears resonance, population is transferred from state $|1\rangle$ (blue trace) into state $|2\rangle$ (green trace). The pulse terminates when it reaches a detuning of $+1$ GHz. The transfer efficiency is nearly 100%.

(see Eq. 5.7). Most of the population transfer occurs when the frequency of the pulse is close to resonance, at the middle of the pulse. Population transfer from state $|1\rangle$ into state $|2\rangle$ is essentially complete.

As discussed in Sec. 5.2.3, in order to maintain adiabaticity, the sweep rate of the pulse may decrease when $\Delta(t) \approx 0$ and the left hand side of Eq. 5.9 is near its minimum. Conversely, at large detunings, the sweep rate may be larger and still satisfy Eq. 5.9. One simple form that has these properties is a cubic frequency sweep, centered about the $|2\rangle$–$|1\rangle$ resonance,

$$\Delta(t) \propto \left(t - \frac{\Delta t}{2}\right)^3, \tag{5.13}$$

where the pulse is assumed to reach resonance halfway through, that is, at $t = \Delta t/2$. A simulation for this form of sweep, also with a total bandwidth of 2 GHz, is given in Fig. 5-3. However, this form of pulse requires only 3 μW of mm-wave power to

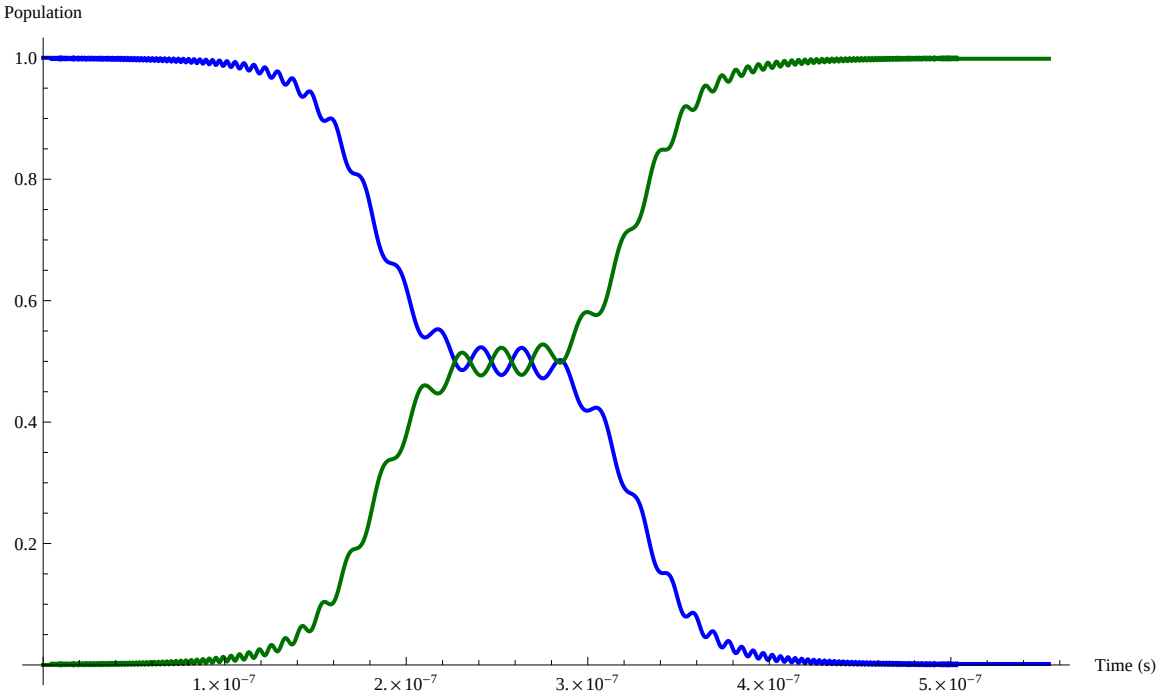

Figure 5-3: A cubic frequency sweep outperforms a linear frequency sweep. Here, $\Delta(t)$ varies according to Eq. 5.13. As in Fig. 5-2, complete population inversion occurs. However, only 3 μW of power is required in this case. Since lower power is required, the coupling when the pulse first turns on is reduced. The brief stoppage of population transfer near resonance occurs because the slope of the cubic sweep is 0 at resonance.

achieve essentially complete population transfer in this 2-level system. Since the power is lower, there is less coupling between the two states at the start of the pulse. A peculiarity of this form of sweep is that the slope of the detuning is strictly zero at resonance. Consequently, in the population profile in Fig. 5-3, the populations begin to invert, then stay at approximately 50% each at resonance, and then complete the inversion. Overall, though, this form of sweep is slightly more effective at transferring population, since lower power is required to achieve the same transfer efficiency for this 2-level system.

Another form of constant-amplitude sweep is the "constant adiabaticity pulse"

(CAP) [5]. The principle of this sweep is to maintain the same level of adiabaticity (that is, the ratio of the right hand side of Eq. 5.9 to its left hand side) throughout the pulse. For the present 2-level system, the detuning profile of the CAP is shown in Fig. 5-4, also for a sweep bandwidth of 2 GHz. The sweep rate is very fast near the

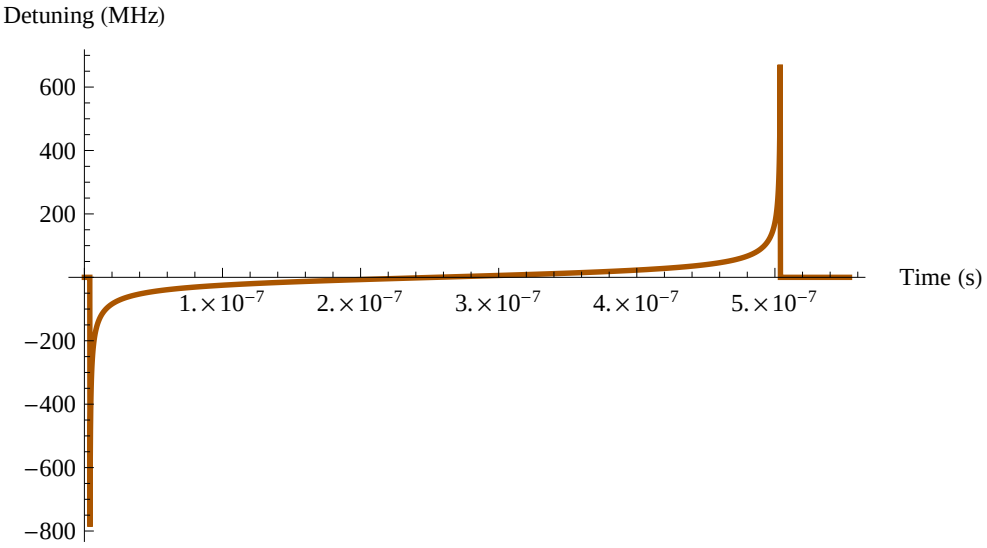

Figure 5-4: Temporal detuning profile for a constant adiabaticity pulse. The sweep rate is very fast when the instantaneous detuning is large, but much slower when the pulse is near resonance. In this way, the adiabaticity (see Eq. 5.9) stays a constant level throughout the sweep. The initial and final detunings are -1 and $+1$ GHz, respectively, which is beyond the vertical scale of the figure.

start and end of the pulse, while slow—but never zero—near the middle of the pulse. The population profile associated with the CAP for this system and with < 2 μW of mm-wave power is shown in Fig. 5-5. The rate of population transfer is approximately constant during this pulse, and the total transfer efficiency is also $\approx 100\%$.

5.3 Composite pulses

Before adiabatic rapid passage techniques, composite pulses were developed—also for NMR spectroscopy—to robustly invert populations of 2-level systems using a pulse that is a "composite" of several short, contiguous pulses of a specified phase and (nominal) pulse area (Eq. 3.1) [43, 20]. By appropriately modulating the phase and

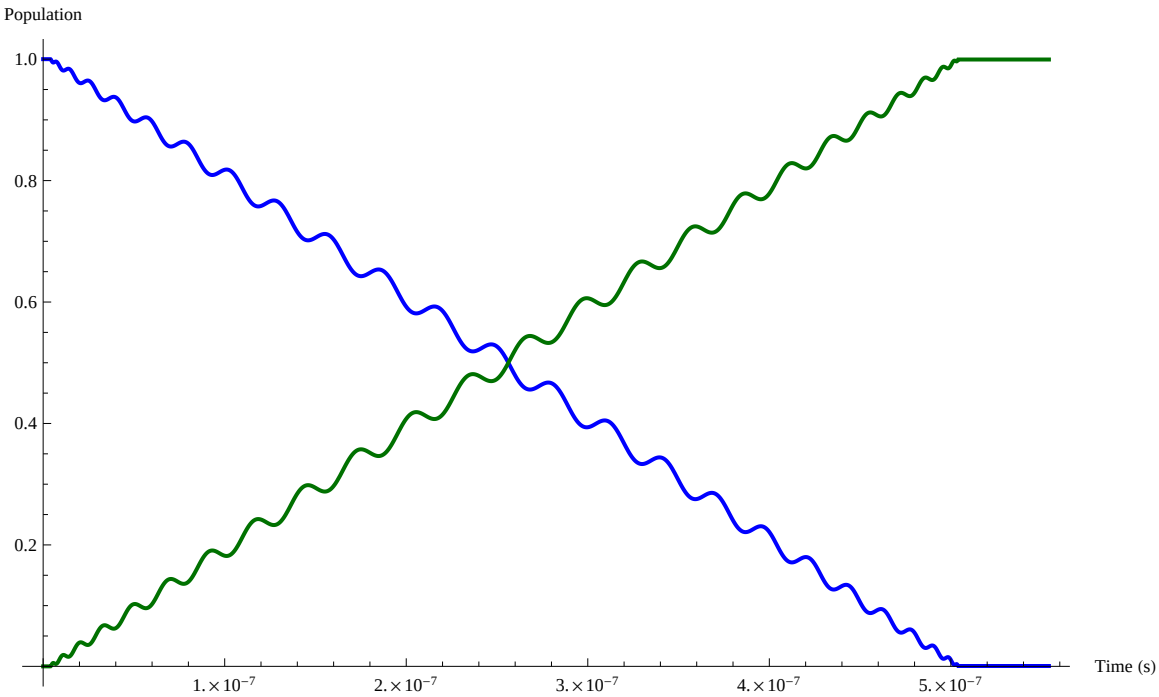

Figure 5-5: Simulation of a frequency sweep with a constant adiabaticity pulse (CAP). This pulse also achieves complete population inversion, although at a mm-wave power of 1.6 μW. Population moves from state $|1\rangle$ to $|2\rangle$ at approximately the same rate throughout the pulse, which is a consequence of the constant adiabaticity that is enforced by the form of the sweep (Fig. 5-4).

duration of each component of the overall composite pulse, high-efficiency population transfer may be achieved. Unlike adiabatic rapid passage, this method does not require significant excitation bandwidth because all of the components of the composite pulse are resonant.

In this section, the basic principles behind composite pulses are explained in Sec. 5.3.1. Then, the Hamiltonian used for simulations is described in Sec. 5.3.2. Finally, simulations of a composite pulse sequence are discussed in Sec. 5.3.3.

5.3.1 Principles of composite pulses

In the rotating frame [71], the 2-level system is represented as a vector in a sphere that rotates at the resonant frequency of the system. The population is the projection onto the vertical (z) axis of the sphere. When a pulse area of θ (Eq. 3.1) is applied to the system, the state vector rotates by an angle θ *about* the phase vector, which lies in the equatorial plane of the sphere. By convention, the first pulse in a sequence is taken to have a phase $\phi = 0$ and point along the x-axis. For example, a $\theta = \pi/2$ initial pulse results in the state vector being coincident with the y-axis. Subsequent pulses with a different phase are referenced against the phase of the initial pulse, which points in a direction determined by the value of ϕ. Thus, a second pulse that is $\phi = \pi/2$ radians different from the first pulse has a phase vector that points along the y-axis. A pulse of area θ about a phase ϕ is denoted $(\theta)_\phi$.

The principle of composite pulses is to break up, for example, a π pulse into multiple pulses, with each component having an area and a phase designed to compensate for imperfections. For instance, the first composite pulse, a π pulse proposed by Levitt and Freeman [43], was

$$\left(\frac{\pi}{2}\right)_0 (\pi)_{\pi/2} \left(\frac{\pi}{2}\right)_0, \tag{5.14}$$

which consists of a $\pi/2$ pulse (implicitly about the x-axis), a π pulse with a phase shift of 90°, and then another $\pi/2$ pulse with the same phase as the first pulse. If the pulse areas are exactly correct, then this sequence is equivalent to a π pulse. However, if the

pulse areas are not perfect, then the components partially cancel the imperfection, and a greater fraction of the population is transferred. For an inhomogeneous excitation source and/or inexact pulse areas (which occurs with CPmmW excitation of Rydberg–Rydberg transitions), the composite pulse technique may provide superior efficiency of population transfer compared to a simple π pulse. Other composite pulse sequences have also been developed [20, 41, 42, 46], but only the pulse given in Eq. 5.14 is discussed in this chapter.

5.3.2 Hamiltonian for composite pulses

For composite pulses, a modified version of Eq. 5.2 is used. The phases of the mm-wave electric field, $\phi(t)$, are included included in the Hamiltonian in Eq. 5.2 by appending an appropriate $e^{i\phi(t)}$ factor to the Rabi frequency:

$$\mathbf{H}(t) = \frac{\hbar}{2}\begin{pmatrix} 0 & \Omega e^{i\phi(t)} \\ \Omega e^{-i\phi(t)} & 2\Delta(t) \end{pmatrix}. \tag{5.15}$$

For composite pulses, the driving field is generally resonant. Thus, $\Delta(t) = 0$, and

$$\mathbf{H}(t) = \frac{\hbar}{2}\begin{pmatrix} 0 & \Omega e^{i\phi(t)} \\ \Omega e^{-i\phi(t)} & 0 \end{pmatrix} \tag{5.16}$$

is the Hamiltonian used for simulations. This Hamiltonian has the advantage of being quite simple, which makes it convenient for simulations.

5.3.3 Simulations of composite pulses in Rydberg states

To simulate the performance of composite pulses for Rydberg–Rydberg transitions, the time-dependent Schrödinger equation (Eq. 5.12) was numerically integrated as in Sec. 5.2.4 for an electric dipole transition moment of 5 kD. The type of composite pulse simulated is that in Eq. 5.14, where the phases of the three components are 0, $\pi/2$, and 0 radians, respectively. Since the mm-wave source cannot be attenuated on the timescale of a single pulse, the nominal pulse area of each component is controlled

by varying its duration. For the simulations shown below, the three component pulses of Eq. 5.14 have durations of 12.5, 25.0, and 12.5 ns, respectively.

For reference, the case where the nominal pulse area and true pulse area are the same is shown in Fig. 5-6. The composite pulse begins at $t = 4$ ns, at which point

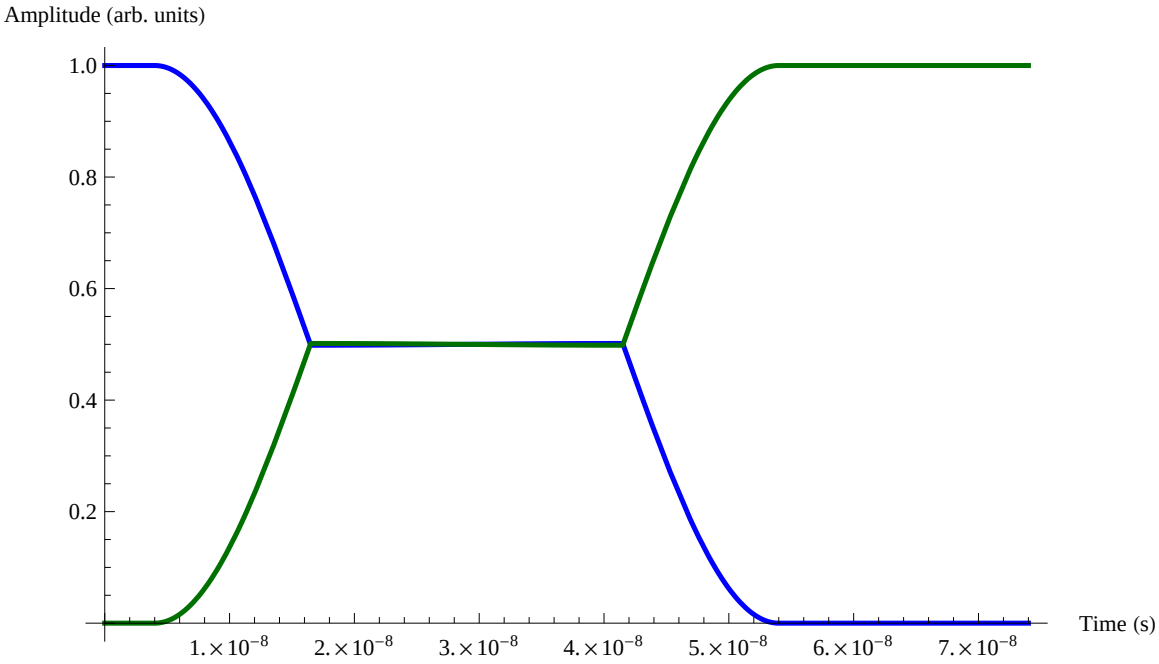

Figure 5-6: A composite π pulse with exact pulse areas behaves the same way as a usual π pulse. In this simulation of the composite pulse in Eq. 5.14, 0.6 μW of mm-wave power are applied to a Rydberg–Rydberg transition of 5 kD. The mm-wave field turns on at 4 ns. The first component pulse has a duration of 12.5 ns and is chosen to have a pulse area of $\pi/2$ exactly. This component pulse transfers half of the population from state $|1\rangle$ (blue trace) into state $|2\rangle$ (green trace). Next, a 25.0-ns component pulse (and thus an area of π) is applied. However, the phase is $+\pi/2$ radians relative to the first pulse, and the population is stationary during this pulse. Finally, a second $\pi/2$ component pulse at 0 phase completes the population inversion. The net effect is the same as if only a perfect π pulse had been applied.

the $\pi/2$ component pulse begins to transfer half of the population from state $|1\rangle$ into state $|2\rangle$. After the $\pi/2$ component pulse is complete, a component pulse with area π and a phase of $+\pi/2$ relative to the first component pulse, is applied. Since the phase vector associated with ϕ is oriented along the same direction of the state vector, there is zero projection of the state that is orthogonal to the phase. Thus, no significant population transfer occurs, and both curves are flat during the component

$(\pi)_{\pi/2}$ pulse. Finally, another $\pi/2$ component pulse, with the same phase (0) as the first component pulse, completes the inversion of the populations. Since the pulse areas are exactly correct, this sequence is equivalent to simply applying a $(\pi)_0$ pulse. Another consequence of the exact pulse areas is that the transfer efficiency is perfect.

If the profile of the mm-wave excitation is inhomogeneous, then parts of the sample will experience a locally stronger or weaker electric field than the nominal value expected from, for example, Eq. 2.1. In Fig. 5-7, the composite pulse in Eq. 5.14 is

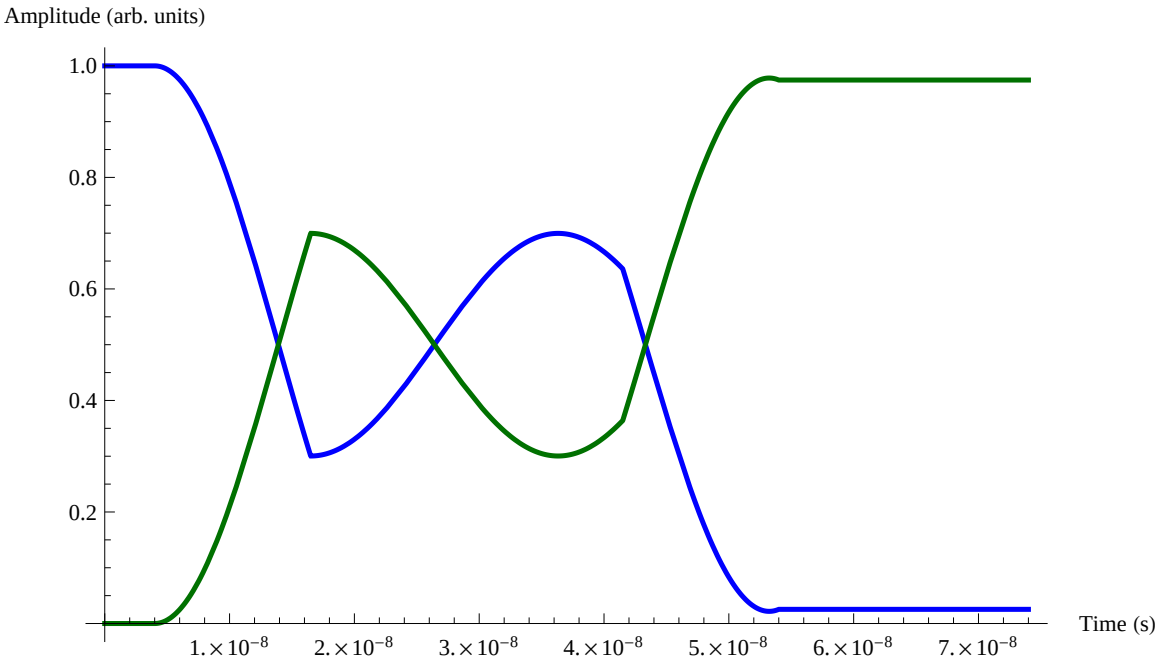

Figure 5-7: A composite pulse with larger-than-nominal pulse areas still has nearly 100% population transfer efficiency. A mm-wave power of 1 μW is used to simulate stronger pulses than those in Fig. 5-6 for a 5-kD transition dipole moment. The first component $\pi/2$ pulse transfers more than half of the poplation into state $|2\rangle$. The second component pulse, however, has a phase shift of 90° from the first component pulse. Consequently, the population rotates about the abscissa of the figure for this component pulse. Since the pulse area of the second component is approximately π, the errors in the pulse areas of the first and third components approximately cancel, and the population transfer is nearly total. The kinks in the population curves are due to the instantaneous modulations of the phase.

simulated in the case where the local electric field is stronger than the nominal field. Here, the pulse areas that the sample experiences are larger than the nominal value, and more than half of the population is transferred by each of the $(\pi/2)_0$ pulses.

However, the approximate $(\pi)_{\pi/2}$ component pulse in the middle reverses most of the overshoot from the first component pulse. Since the area of the third component pulse is the same as the first, the excesses of the two pulse areas mostly compensate each other. Thus, the population transfer efficiency is still nearly 100%, while it would have been only ≈60% without the $(\pi)_{\pi/2}$ pulse between the two $(\pi/2)_0$ pulses. Conversely, Fig. 5-8 shows a case where the pulse areas are smaller than the nominal

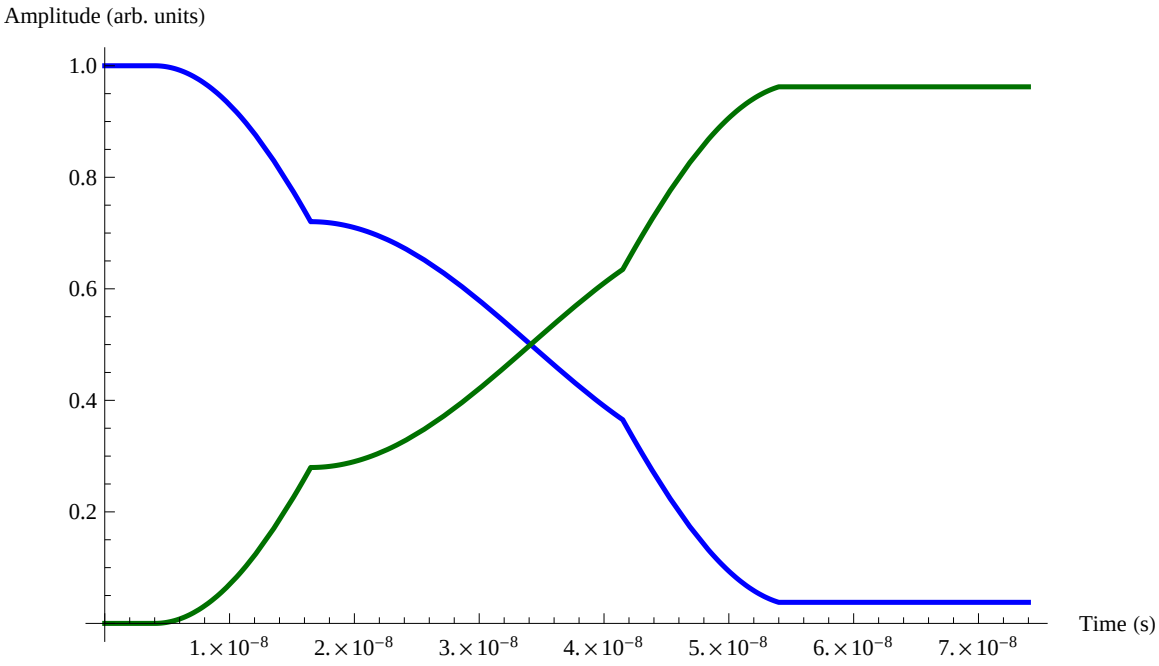

Figure 5-8: A composite pulse with weaker-than-nominal pulse areas also achieves nearly perfect population transfer. In this case, approximately 0.3 μW of mm-wave power are used to simulate the case where the pulse area is lower than the nominal value. As in Fig. 5-7, the imperfections in the component pulses compensate each other, and the population transfer is nearly complete.

values. Similar to Fig. 5-7, the phase-modulated π pulse in the middle of the sequence compensates for the inhomogeneity, and the population transfer efficiency is about 95% instead of approximately 60%.

5.4 Prospects for implementation of robust population transfer techniques

Based on the simulations presented in this chapter, I conclude that both adiabatic rapid passage and composite pulse techniques will be viable for robustly transferring populations in Rydberg states. For challenges of, and possible experimental techniques for, measuring population transfer efficiency in Rydberg–Rydberg transitions, see the discussion in Sec. 6.4.

An advantage of the composite pulse approach is that implementation for the CPmmW spectrometer is straightforward: Once the approximate power required for a π pulse of a given duration is determined empirically (see the discussion in Sec. 3.1.2), a composite pulse with components of appropriate duration and phase may be programmed into the arbitrary waveform generator. No other information is required. Additionally, the duration of a composite pulse need not be substantially longer than a single π pulse. For example, the sequence in Eq. 5.14 is only twice the duration of a π pulse alone, which is generally not significant for experiments.

Adiabatic frequency sweeps are also well suited to the capabilities of the CPmmW spectrometer, which can, in most cases, easily cover several GHz of bandwidth in a chirped pulse. However, the sweep durations that are required may be a disadvantage if state $|1\rangle$ has a lifetime that is similar to the sweep duration. Also, adiabatic sweeps may not be feasible if other allowed, undesirable transitions also occur within the sweep bandwidth. For such a situation, composite pulses, which involve only resonant excitation, may be more effective.

Chapter 6

Stimulated Raman adiabatic passage for generating high-ℓ Rydberg states

In this chapter, I discuss the simulation of the stimulated Raman adiabatic passage (STIRAP) method [24, 7, 83] for producing Rydberg states of high orbital angular momentum while evading the fast predissociation that is nearly omnipresent in core-penetrating, molecular Rydberg states. The excitation scheme is described in Sec. 6.1. The Hamiltonian for STIRAP and the mechanism of population transfer are explained in Sec. 6.2. Simulations of STIRAP based on parameters of realistic Rydberg systems are discussed in Sec. 6.3, in which the layers of complexity are added sequentially until all of the essential aspects of a real system are encompassed. The prospects for experimental observation of the phenomena simulated in this chapter are addressed in Sec. 6.4.

6.1 STIRAP excitation schemes in Rydberg atoms and molecules

In Rydberg molecules, states of low ℓ (i.e. $\ell < 4$) generally predissociate on timescales significantly faster than the 1–10 μs required to collect an FID spectrum with the CP-mmW method. Rydberg states of higher ℓ, however, are termed "core-nonpenetrating" because they rarely interact with the ion-core. Because these states do not exchange much energy or angular momentum with the ion-core, they survive for much longer than core-penetrating states. The structure of these core-nonpenetrating states is determined by the multipole moments and polarizabilities of the ion-core, which require high resolution—such as what is available with microwave and mm-waves—to study (Sec. 7.3).

The primary advantage of the STIRAP method for generating high-ℓ Rydberg molecules, then, is that there may be zero population in a (predissociated) core-penetrating state while still achieving 100% population transfer into the target high-ℓ state. A general scheme for populating core-nonpenetrating Rydberg states with the STIRAP method is shown in Fig. 6-1. The 2-photon (laser + mm-waves) transition excites a core-nonpenetrating Rydberg state, and then another mm-wave photon may excite a transition between two core-nonpenetrating states.

6.2 Principles of STIRAP

In this section, I describe the principles behind the STIRAP process. The STIRAP Hamiltonian for a 3-level system, its components, and its eigenstates are explained in Sec. 6.2.1. The mechanism of population transfer and the criteria that must be satisfied are then discussed in Sec. 6.2.2.

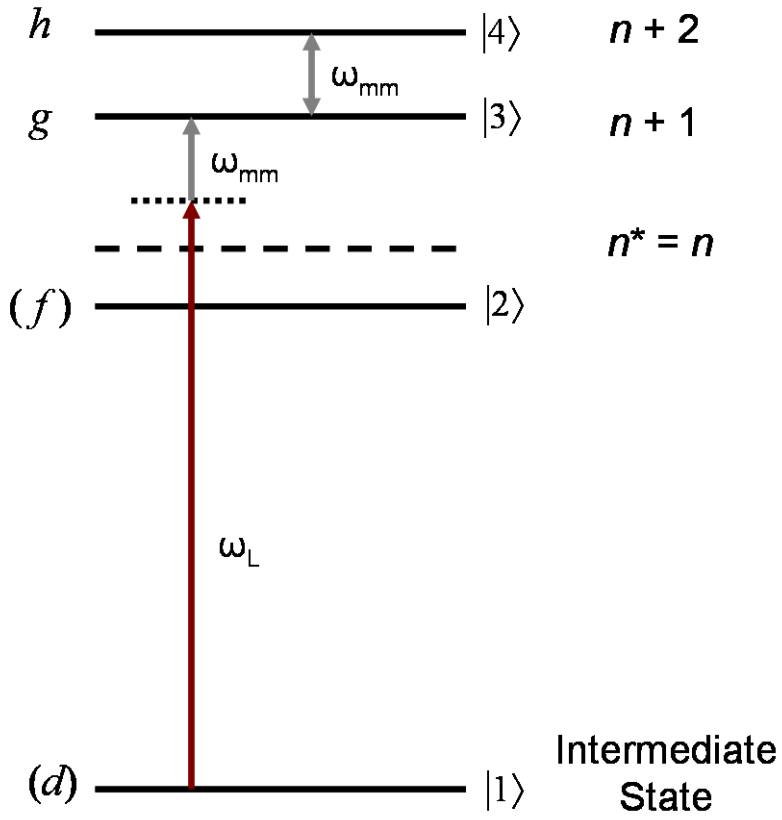

Figure 6-1: A class of optical/mm-wave excitation scheme for populating g and h Rydberg states while avoiding predissociation. A combination of laser (red arrow) and mm-wave (gray arrow) fields transfer population from an intermediate Rydberg state to a g state, which is core-nonpenetrating. A second mm-wave photon may then probe the h–g transition. In the discussions below, the d state corresponds to state $|1\rangle$, f to $|2\rangle$, and g to $|3\rangle$. The laser energy does not need to be precisely resonant with the f–d transition to achieve high-efficiency population transfer; however, the laser + mm-wave 2-photon energy should be exactly resonant with the $|3\rangle$–$|1\rangle$ transition. The quantum defects of the g and h states are nearly zero, so these states appear at energies close to $n^* = n$. The d and f states are shown in parentheses to denote their mixed-ℓ character in Rydberg molecules. The weakly penetrating f state is also generally predissociated in molecular Rydberg systems.

6.2.1 The STIRAP Hamiltonian

In this chapter, the (time-dependent) Rabi frequency of an interaction with an electric field is given by

$$\Omega(t) = \frac{\mu\ \varepsilon(t)}{\hbar}. \tag{6.1}$$

Here, the $\Omega(t)$ notation for the Rabi frequency is used instead of that of Eq. 3.2. This choice is made both to be consistent with the STIRAP literature in general (and Ref. [7] in particular) and to emphasize that, for this application, the amplitude of the excitation electric field varies with time.

The 3-level Hamiltonian used for the STIRAP simulations is [7]

$$\mathbf{H}(t) = \frac{\hbar}{2}\begin{pmatrix} 0 & \Omega_{\mathrm{L}}(t) & 0 \\ \Omega_{\mathrm{L}}(t) & 2\Delta_{\mathrm{L}} & \Omega_{\mathrm{mm}}(t) \\ 0 & \Omega_{\mathrm{mm}}(t) & 2\left(\Delta_{\mathrm{L}} + \Delta_{\mathrm{mm}}\right) \end{pmatrix}. \tag{6.2}$$

For simplicity, the 3 states in Eq. 6.2 are labeled $|1\rangle$, $|2\rangle$, and $|3\rangle$. The subscript "L" refers to the laser field, while "mm" refers to the mm-wave field. For this Hamiltonian, the rotating wave approximation (considering only driving frequencies near resonance) has been made. Also implicit is that Eq. 6.2 is the matter + field Hamiltonian. Thus, state $|1\rangle$ is not associated with any excitation. State $|2\rangle$ is associated with 1 quantum of laser excitation. Therefore, the diagonal element of state $|2\rangle$ in Eq. 6.2 is the *detuning* of the laser frequency from 1-photon resonance,

$$\Delta_{\mathrm{L}} = \frac{E_2 - E_1}{\hbar} - \omega_{\mathrm{L}}, \tag{6.3}$$

where E_n is the energy of state n, and ω_{L} is the angular frequency of the laser radiation. In the present discussion the detuning has units of frequency. Analogous to state $|2\rangle$, the diagonal element of state $|3\rangle$ is the detuning of the mm-wave radiation from the $|2\rangle$–$|3\rangle$ resonance:

$$\Delta_{\mathrm{mm}} = \frac{E_3 - E_2}{\hbar} - \omega_{\mathrm{mm}}. \tag{6.4}$$

It is notable that the sign convention in Eq. 6.4 is reversed from that in Ref. [7]. This reversal is because STIRAP is generally discussed in the context of Λ-type 3-level systems, whereas the applications of optical/mm-wave Rydberg excitation may be for either Λ- or ladder-type (see Fig. 6-1) level arrangements. The convention in this chapter thus is to treat the detunings for both the laser and mm-wave fields in the same way. Since state $|1\rangle$ is not associated with any excitation, it is taken to have a detuning of 0 by convention. Population decay of any state (such as from a predissociated Rydberg state) may be included in Eq. 6.2 by adding an imaginary element to the diagonal (such as $i\gamma/2$), which then encodes the decay rate (γ) of population in the state. The off-diagonal matrix elements in Eq. 6.2 are the time-dependent Rabi frequencies. This structure shows that the laser field ($\Omega_{\mathrm{L}}(t)$) connects state $|1\rangle$ to state $|2\rangle$, while the mm-wave field ($\Omega_{\mathrm{mm}}(t)$) connects state $|2\rangle$ to state $|3\rangle$.

The representation in Eq. 6.2 and below is similar to the "dressed state" formalism, but without explicit treatment of the field [7]. In the case of strong coupling with the field (implied by Eq. 6.8 below), this choice of representation is more computationally convenient than employing oscillating electric fields as the off-diagonal matrix elements between states; the frequency of the oscillations of the driving field is folded into a diagonal term of the Hamiltonian (which could be time dependent in the case of a chirped pulse, as in Sec. 5.2), while the off-diagonal element varies in only the amplitude of the driving field. Moreover, with the very large electric dipole transition moments of Rydberg states, the strong coupling regime is likely to be encountered.

The eigenstates of the 3-level system described by Eq. 6.2 are [7]

$$|+\rangle = \sin\Theta\sin\Phi|1\rangle + \cos\Phi|2\rangle + \cos\Theta\sin\Phi|3\rangle \tag{6.5a}$$

$$|0\rangle = \cos\Theta|1\rangle - \sin\Theta|3\rangle \tag{6.5b}$$

$$|-\rangle = \sin\Theta\cos\Phi|1\rangle - \sin\Phi|2\rangle + \cos\Theta\cos\Phi|3\rangle, \tag{6.5c}$$

where the mixing angles Θ and Φ both depend on the Rabi frequencies, while Φ also

depends on the detunings. The mixing angle Θ is discussed in more detail in the next section.

6.2.2 Population transfer in STIRAP

The key to the STIRAP process is eigenstate $|0\rangle$ in Eq. 6.5b, which has character of states $|1\rangle$ and $|3\rangle$, but none of $|2\rangle$. Thus, adiabatically changing the character of eigenstate $|0\rangle$ from completely state $|1\rangle$ to completely state $|3\rangle$ would achieve 100% population transfer from state $|1\rangle$ to state $|3\rangle$. During this process, no population ever resides in state $|2\rangle$. More specifically, the mixing angle Θ is given by

$$\tan\Theta = \frac{\Omega_{\mathrm{L}}(t)}{\Omega_{\mathrm{mm}}(t)}. \tag{6.6}$$

Rewriting this relation as

$$\frac{\sin\Theta}{\cos\Theta} = \frac{\Omega_{\mathrm{L}}(t)}{\Omega_{\mathrm{mm}}(t)}, \tag{6.7}$$

it is evident that complete population transfer from state $|1\rangle$ to $|3\rangle$ via eigenstate $|0\rangle$ may be achieved by firing the mm-wave pulse *first*, followed by the laser pulse. If the system begins in state $|1\rangle$, and the mm-wave pulse arrives first, then the $\cos\Theta$ component, and thus state $|1\rangle$ character of eigenstate $|0\rangle$, is also large. If the laser then arrives and the mm-waves terminate such that the system smoothly changes to a state where $\sin\Theta$, and thus the state $|3\rangle$ character of eigenstate $|0\rangle$, is large, then complete population transfer may be achieved. The "counterintuitive" order of the pulses [7] is an earmark of the STIRAP process.

One requirement for high-efficiency population transfer is that the coupling of the zeroth-order states to the radiation fields must be large. Also, to change adiabatically the character of eigenstate $|0\rangle$ from state $|1\rangle$ to state $|3\rangle$, it is better (although not always strictly necessary) that the temporal profiles of both the laser and mm-wave pulses be smooth. More specifically, assuming that the laser pulse is resonant (i.e. $\Delta_{\mathrm{L}} = 0$), the condition on the Rabi frequencies for adiabatic change of the character

of the eigenstates is [7]

$$\left|\frac{\partial\Omega_{\rm L}(t)}{\partial t}\Omega_{\rm mm}(t) - \Omega_{\rm L}(t)\frac{\partial\Omega_{\rm mm}(t)}{\partial t}\right| \ll \left(\Omega_{\rm L}^2(t) + \Omega_{\rm mm}^2(t)\right)^{3/2}. \tag{6.8}$$

Violation of this inequality leads to "non-adiabatic" transitions where the population moves into the undesirable state $|2\rangle$ via the $|+\rangle$ or $|-\rangle$ eigenstates.

6.3 Simulations of STIRAP for optical/mm-wave population transfer in Rydberg states

In this section, I discuss simulations of optical/mm-wave STIRAP for Rydberg systems such as those outlined in Sec. 6.1. First, the parameters that correspond to these systems are described in Sec. 6.3.1. Second, simulations of population transfer in 3-level systems are described in Sec. 6.3.2. Third, in Sec. 6.3.3, a second Rydberg level is added to the manifold, and the consequences are analyzed. Finally, the effects of using longer laser pulses are characterized in Sec. 6.3.4 for 3-level systems.

6.3.1 Simulation parameters

To simulate STIRAP for optical/mm-wave excitation of Rydberg states, the time-dependent Schrödinger equation (Eq. 5.12) is integrated numerically using the Hamiltonian matrix in Eq. 6.2 for parameters that correspond to our experimental conditions. Since the Hamiltonian is a matrix, $\Psi(t)$ in Eq. 5.12 is understood to be a vector of state coefficients. Initially, the entire system population is in state $|1\rangle$.

For the optical transition, the assumed parameters are an electric dipole transition moment of 2 Debye (typical for an allowed optical transition), a pulse energy of 10 mJ, a duration of about 5 ns (temporal full width at half maximum), and a pulse bandwidth of 0.03 cm^{-1} (the specification for our pulsed dye lasers when an etalon is used to narrow the bandwidth). In this case, the bandwidth of the pulsed dye laser is significantly larger than that of a Fourier-transform-limited pulse of the same duration. To account for this difference, I used an effective Rabi frequency for the

laser field,

$$\Omega_{\mathrm{L,\ eff}}(t) = \Omega_{\mathrm{L}}(t)\frac{\Delta\omega_{\mathrm{FT}}}{\Delta\omega_{\mathrm{L}}}, \tag{6.9}$$

where $\Delta\omega_{\mathrm{L}}$ is the bandwidth of the laser pulse and $\Delta\omega_{\mathrm{FT}}$ is the bandwidth of a Fourier-transform limited pulse with the same duration as the laser.[1] This effective Rabi frequency dampens the coupling strength of the laser by the extent to which the laser pulse is not Fourier-transform limited. This computational approach is employed because it is consistent with the scaling presented in Ref. [7]. The temporal envelope of the laser is a Gaussian.

For a mm-wave transition, an electric dipole transition moment of 5 kD was assumed, which is typical of $|\Delta n^*| \leq 1$ Rydberg–Rydberg transitions of n^* around 45. A mm-wave pulse with an energy of 0.5 mW (easily feasible with the active multipliers that generate 30 mW) and a duration of 10 ns (chosen to match approximately the pulse duration of the laser) was assumed. The temporal profile of the mm-waves is a rectangular pulse because the active multipliers generate a fixed power output (see Sec. 2.2).

6.3.2 Population transfer for 3-level systems

Results of a simulation using the parameters mentioned above are shown in Fig. 6-2 for a situation where there is no predissociation in state $|2\rangle$ and where both the laser and mm-wave frequencies are perfectly resonant. The mm-wave and laser pulse timings that correspond to Fig. 6-2 are shown in Fig. 6-3. The efficiency of population transfer into state $|3\rangle$ is $\approx$90% in this case. Some population does move into state $|2\rangle$, which shows that the STIRAP population transfer is not perfect, even in this idealized case. However, the efficiency is high enough to hold promise.

A key aspect of the population transfer is the relative pulse timings, illustrated in Fig. 6-3. It was found empirically that the turn-off of the mm-wave pulse must come almost exactly at the maximum of the amplitude of the laser pulse. Otherwise, the transfer efficiency decreases drastically. This behavior occurs because the mm-wave

[1] A useful relation here is that, in units convenient for spectroscopy, the speed of light in vacuum is $c = 29.979\ \mathrm{GHz/cm^{-1}}$.

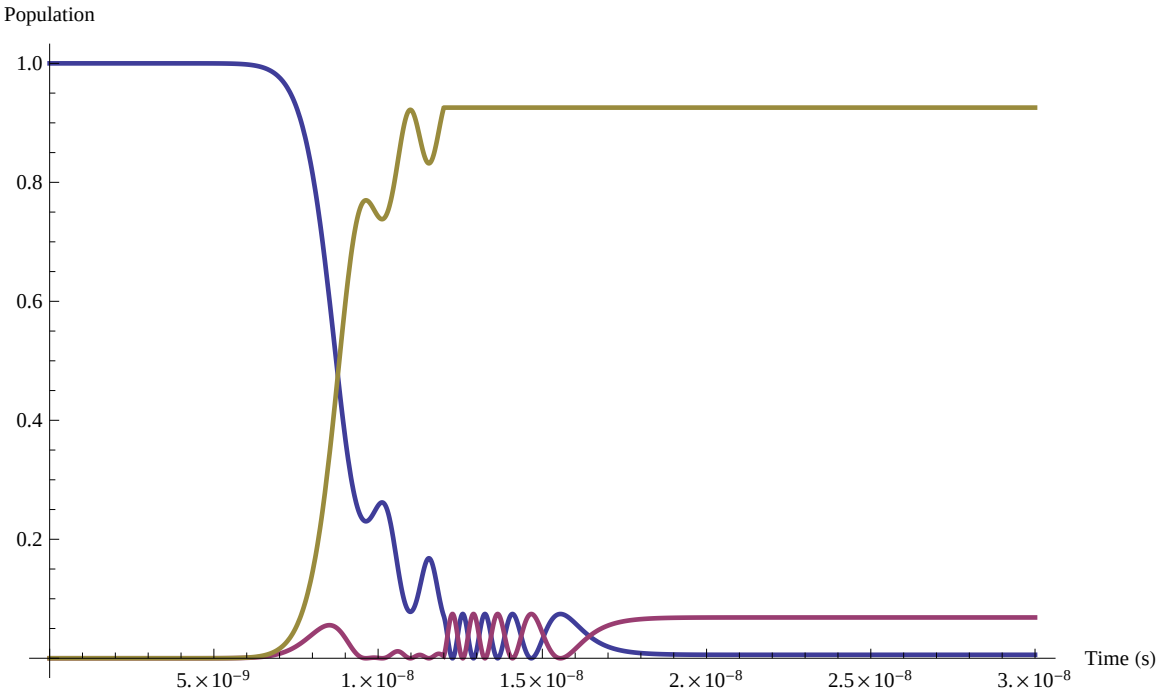

Figure 6-2: A simulation shows that optical/mm-wave STIRAP in a 3-level system may be possible with a pulsed dye laser. Initially, the population is entirely in state $|1\rangle$ (blue trace). During the excitation sequence, shown in Fig. 6-3, a small fraction of the population moves into state $|2\rangle$ (pink trace), while approximately 90% of the population is transferred into state $|3\rangle$ (gold trace). The population that has not been transferred into state $|3\rangle$ oscillates between states $|1\rangle$ and $|2\rangle$ during the time after the mm-wave pulse has terminated but the laser pulse is still present.

pulse is a square wave and does not have a smooth temporal profile. Because of the sharp turn-off of the mm-wave pulse, the $\frac{\partial}{\partial t}\Omega_{\mathrm{mm}}(t)$ term in Eq. 6.8 becomes large at this point, and the adiabaticity criterion may only be satisfied when the laser pulse is close to its maximum amplitude.

In Fig. 6-4, the same parameters are simulated as in Figs. 6-2 and 6-3, except with a predissociation lifetime of 100 ps in state $|2\rangle$ (incorporated using the complex Hamiltonian formalism). Here, the consequences of transient population in state $|2\rangle$ become apparent. The transfer efficiency decreases to about 50%, which is still experimentally viable, and the other half of the population has decayed out of the system. Here, it also becomes apparent that direct, multi-photon excitation will not generate appreciable population in Rydberg molecules. If predissoication happens on a timescale faster than the excitation pulses, the transient population in the predis-

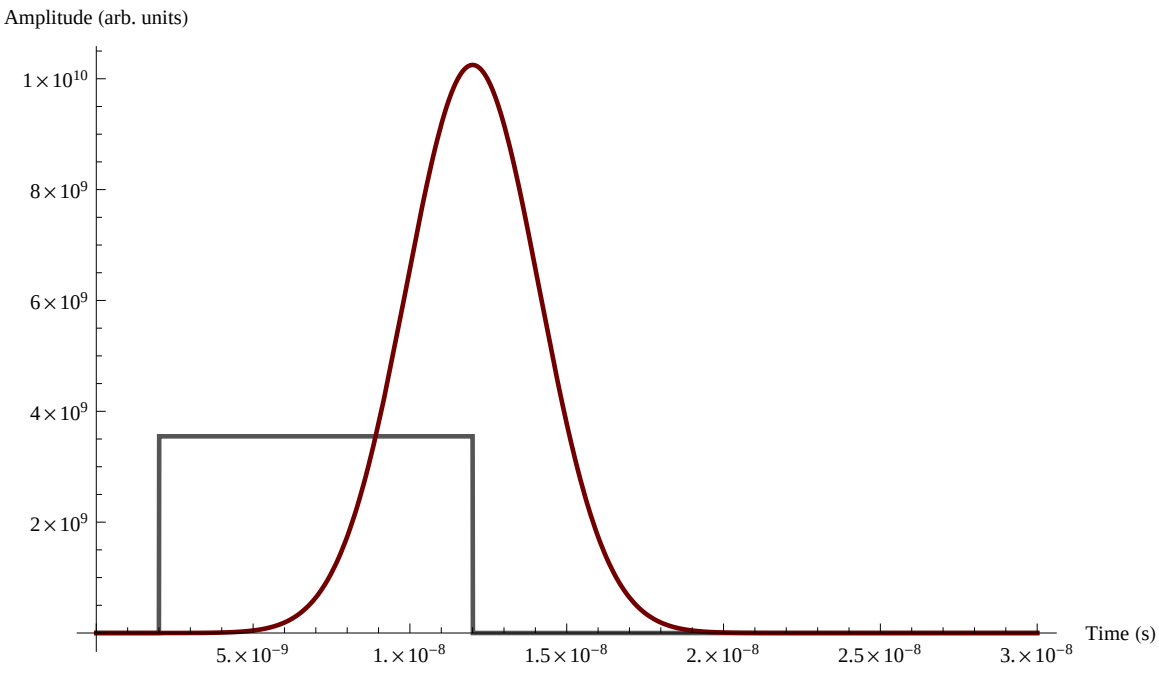

Figure 6-3: Optimizing the pulse timings is essential for optical/mm-wave STIRAP. The mm-waves (gray, square pulse) arrive *first*. During the mm-wave pulse, the laser (red, Gaussian pulse) begins to arrive. The mm-wave pulse terminates exactly at the maximum of the laser pulse amplitude, which is essential for satisfying the adiabaticity criterion in Eq. 6.8. Since the effective Rabi frequency of the laser field is lowered according to Eq. 6.9, the relative amplitudes of the two pulses shown in the figure are not particularly meaningful.

sociated state will have decayed by the end of the excitation. Thus, a more carefully designed method, such as STIRAP, is required to avoid nearly complete population loss.

Even though a pulsed dye laser, with its bandwidth substantially larger than that of a Fourier-transform-limited pulse of the same duration, is not particularly well-suited to performing STIRAP, the process will still succeed in this system. The mm-wave source is easily controlled and is associated with the large electric dipole moments of Rydberg–Rydberg transitions, which helps to drive the STIRAP process. The mm-waves, however, do not have a smooth temporal profile, which may cause loss. The laser pulse, however, has a Gaussian envelope that, if located correctly in time, can compensate for the discontinuous pulse envelope of the mm-wave source. (It may be feasible to further enhance the STIRAP efficiency by shaping the temporal

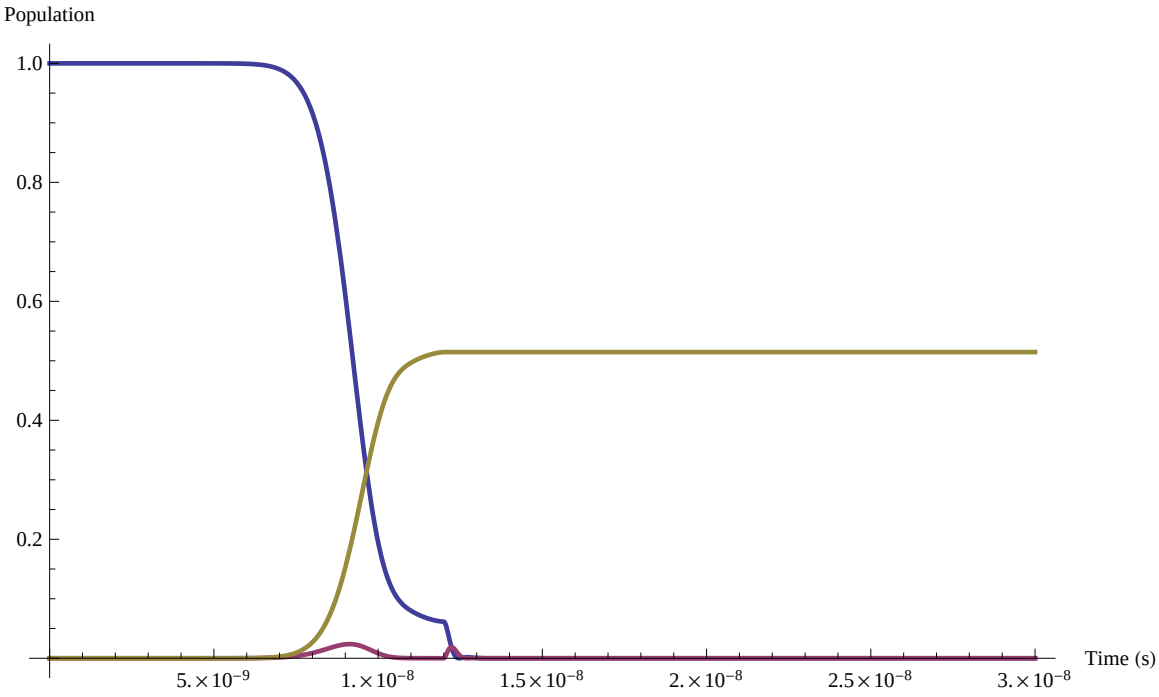

Figure 6-4: Optical/mm-wave STIRAP still transfers population in a 3-level system with a population decay in state $|2\rangle$. The parameters here are the same as in Fig. 6-2, except with a 100 ps lifetime of state $|2\rangle$. Only 50% of the system population is transferred into state $|3\rangle$. The other half of the population has decayed out of the system. This loss is consistent with the transient state $|2\rangle$ population that is observed during the pulse sequence.

profile of the mm-waves with a fast, voltage-controlled attenuator.)

In Fig. 6-5, a detuning of the laser frequency, $\Delta_{\mathrm{L}} = 5$ GHz (0.17 cm^{-1}), is added, but the overall 2-photon resonance is maintained ($\Delta_{\mathrm{mm}} = -\Delta_{\mathrm{L}}$). The population transfer efficiency further decreases, but only to ≈30%. This simulation shows that the overall efficiency is not particularly sensitive to the laser detuning, provided that the 2-photon resonance condition is satisfied. It was found that efficiency is, however, sensitive to 2-photon resonance. For example, under the conditions of Fig. 6-2, a 2-photon detuning of 500 MHz completely quenches the population transfer. Also, with the laser photon perfectly resonant, a 100 ps lifetime, and a 2-photon detuning of 200 MHz, the transfer efficiency is ≈20%.

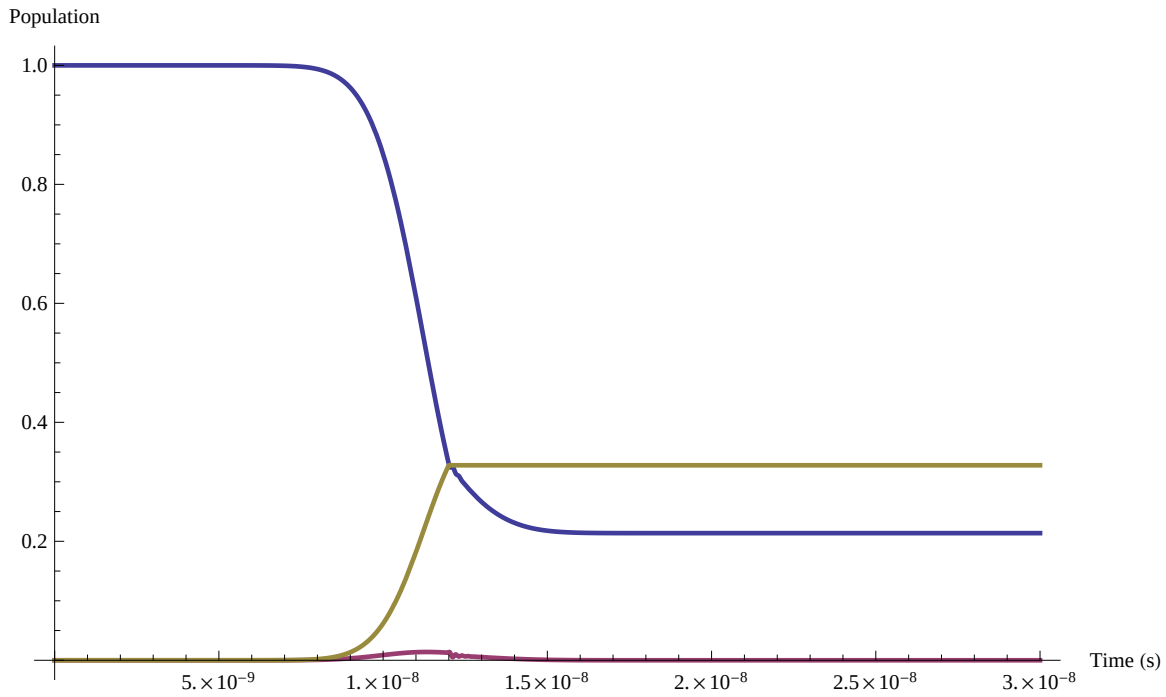

Figure 6-5: STIRAP in a 3-level system with a population decay in state $|2\rangle$ and a laser detuning of 5 GHz, but with the 2-photon transition still resonant. Precise resonance of the laser pulse is not essential for transferring population, as the efficiency here is still around 30%. Overall 2-photon resonance, however, is necessary. Another consequence of the nonresonant laser field is that not all of the population moves out of state $|1\rangle$. Furthermore, less population is lost to decay here than in Fig. 6-4.

6.3.3 Population transfer in 4-level systems with 2 Rydberg states

In Rydberg systems, it is probable that in addition to the 3 levels considered above, there will be another state, $|4\rangle$, that is approximately $\hbar\omega_{\mathrm{mm}}$ away from state $|3\rangle$, as indicated in Fig. 6-1. To anticipate the effects of such a situation, a fourth state was added to the Hamiltonian in Eq. 6.2, which is coupled to state $|3\rangle$ by $\Omega_{\mathrm{mm}}(t)$ and has an associated 3-photon (1 laser + 2 mm-wave photons) overall detuning of Δ_4,

$$\mathbf{H}(t) = \frac{\hbar}{2}\begin{pmatrix} 0 & \Omega_{\mathrm{L}}(t) & 0 & 0 \\ \Omega_{\mathrm{L}}(t) & 2\Delta_2 & \Omega_{\mathrm{mm}}(t) & 0 \\ 0 & \Omega_{\mathrm{mm}}(t) & 2\Delta_3 & \Omega_{\mathrm{mm}}(t) \\ 0 & 0 & \Omega_{\mathrm{mm}}(t) & 2\Delta_4 \end{pmatrix}. \tag{6.10}$$

For brevity, the notation for the detunings has been changed so that the diagonal element indicates the overall detuning from resonance for that level: Δ_2 for state $|2\rangle$, Δ_3 for state $|3\rangle$, and Δ_4 for state $|4\rangle$. A further benefit to this notation is that this approach may be easily extended to systems of arbitrary level arrangements and couplings. Simulation of this Hamiltonian with the same parameters as in Fig. 6-2 and a 3-photon detuning (Δ_4) of 1 GHz is shown in Fig. 6-6. The final state distribution is substantially similar to that in Fig. 6-2, and less than 10% of the population moves into state $|4\rangle$. This simulation indicates that population is unlikely to transfer into an unintended state.

A lifetime of 100 ps for state $|2\rangle$ is added for the simulation shown in Fig. 6-7. Qualitatively, the population distribution resembles that of the 3-level system with decay (Fig. 6-4). The final state $|3\rangle$ population is down to 40%, compared to 50% in Fig. 6-4. Part of this difference is that a small population has moved into state $|4\rangle$. The remainder of the difference is likely due to $|4\rangle$–$|3\rangle$ couplings decreasing the $|3\rangle$–$|2\rangle$ transfer efficiency by changing the state $|3\rangle$ eigenenergy while the mm-wave field is present. It is worth noting here that, given a large initial population in state $|1\rangle$, transfer of a few percent into state $|4\rangle$ may still provide a sufficient number of

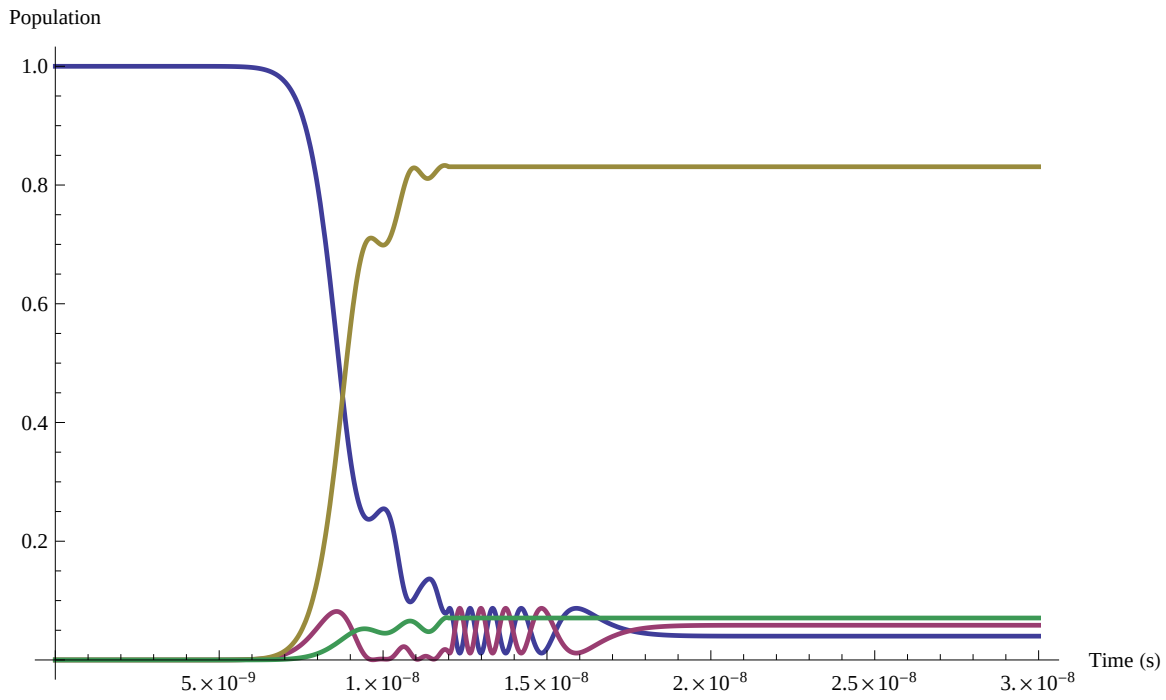

Figure 6-6: A second Rydberg level does not significantly affect optical/mm-wave STIRAP. Parameters are the same as in Fig. 6-2, and the $|3\rangle$–$|2\rangle$ transition differs in frequency by 1 GHz from the $|4\rangle$–$|3\rangle$ transition. Overall, the population curves resemble those of Fig. 6-2. The transfer efficiency into state $|3\rangle$ is still >80%, and 5–10% of the population finishes in state $|4\rangle$ (green trace).

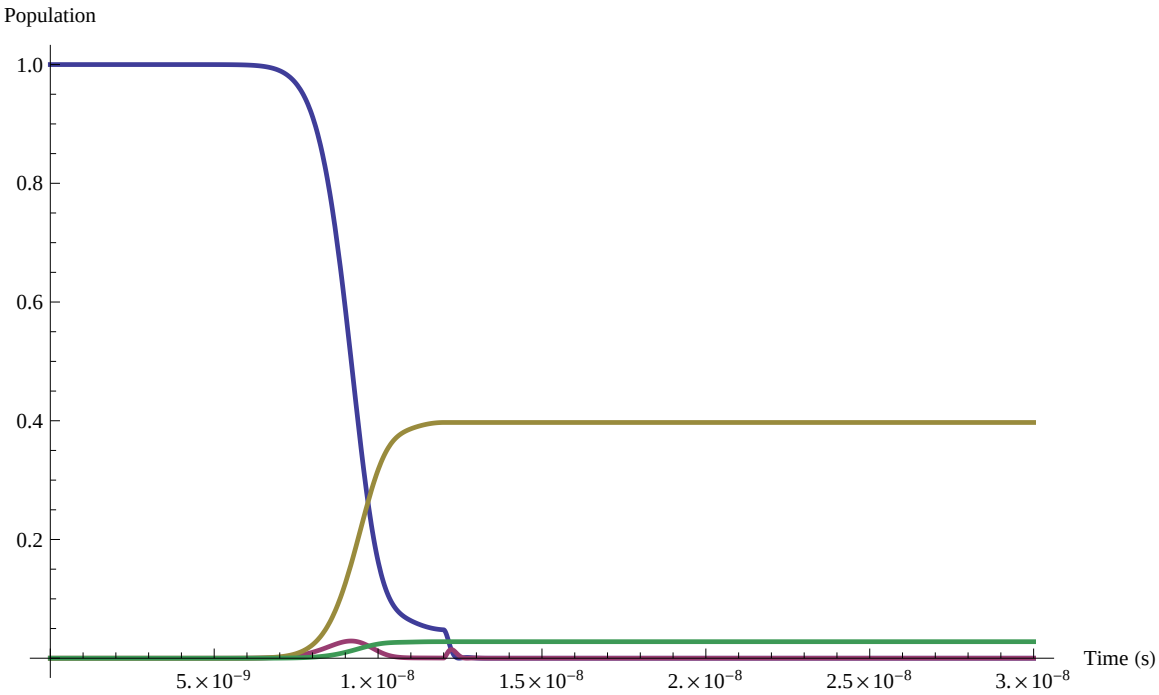

Figure 6-7: 4-level optical/mm-wave STIRAP with predissociation in state $|2\rangle$. Parameters for this simulation are similar to those in Fig. 6-6, except with a 100-ps lifetime in state $|2\rangle$. Approximately 40% of the population is transferred into state $|3\rangle$, while a small fraction of the population is also transferred into state $|4\rangle$.

Rydberg emitters to observe transitions between state $|4\rangle$ and other Rydberg states.

6.3.4 3-level systems with long laser pulses

In simulations of 3-level, optical/mm-wave STIRAP under various conditions, it was found that a laser pulse with substantially longer duration (200 ns full width at half maximum, for example), *even if the bandwidth is not Fourier-transform-limited*, significantly enhances both the transfer efficiency and the robustness of the STIRAP process. A simulation is shown in Fig. 6-8, which has a 100 ps lifetime in state $|2\rangle$.

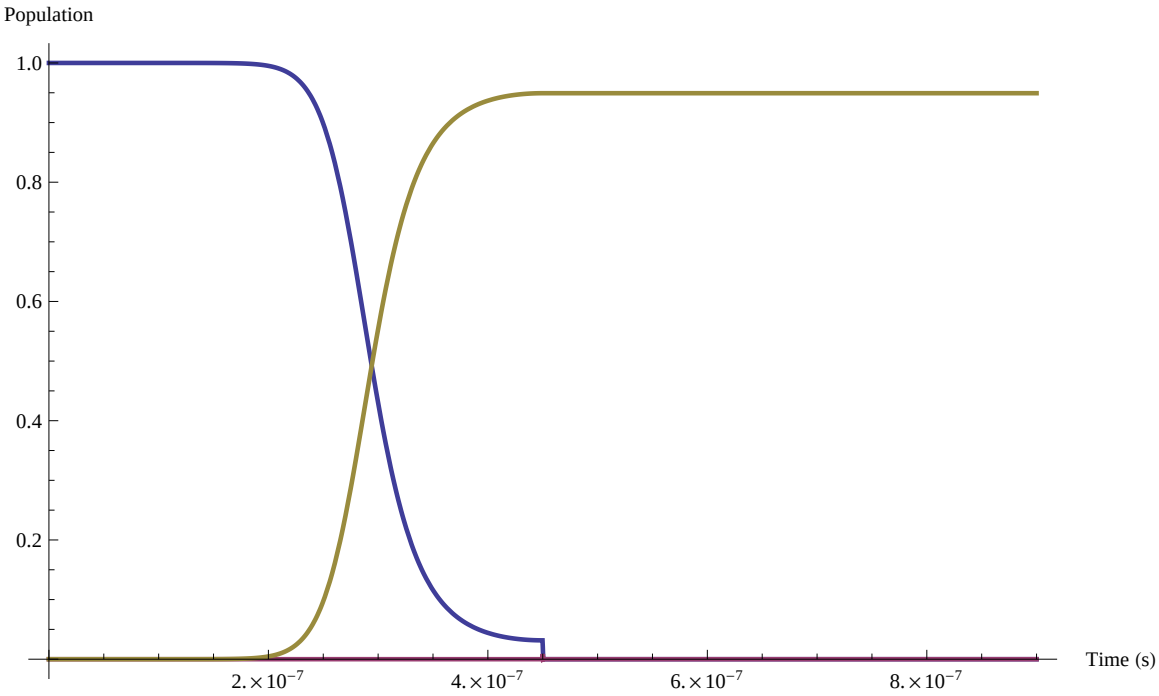

Figure 6-8: 3-level optical/mm-wave STIRAP with a long laser pulse is much more efficient. In this simulation, the Gaussian laser pulse has a full width at half maximum of 200 ns, but the pulse energy is still 10 mJ, as used above. The mm-wave pulse duration has been changed to 200 ns to better match the simulated laser pulse. The relative timing of the pulses is similar to that in Fig. 6-3, with the mm-wave pulse turning off exactly at the maximum of the laser pulse amplitude. With a state $|2\rangle$ lifetime of 100 ps, the transfer efficiency exceeds 90%.

The efficiency is above 90%, and the transient state $|2\rangle$ population is minimal over the longer pulses. A much shorter predissociation lifetime of 1 ps is simulated in Fig. 6-9. In this case, transfer efficiency is still 30%, which is more than sufficient

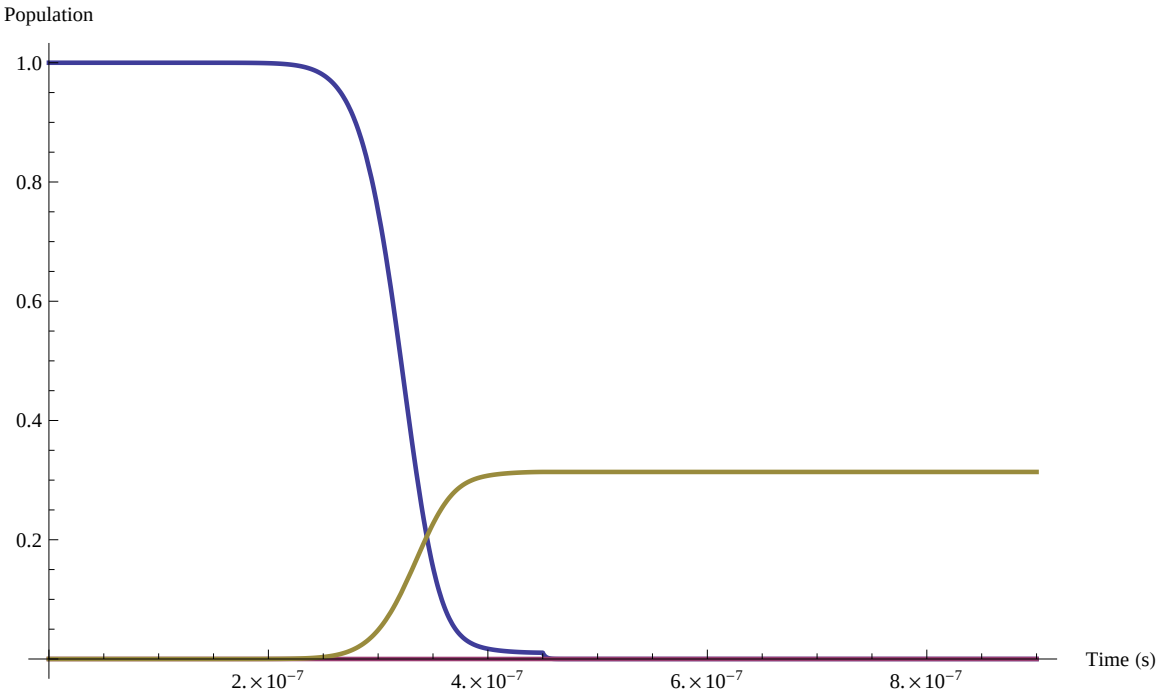

Figure 6-9: 3-level STIRAP with a long laser pulse is viable in the case of fast predissociation. The decay time of state $|2\rangle$ is reduced to 1 ps, and the transfer efficiency is still 30%. The transient population in state $|2\rangle$ is small over this 400-ns process, but the accumulation of this small population results in the calculated loss.

for performing further experiments on the prepared system. Longer pulses result in higher transfer efficiencies because they the change the character of eigenstate $|0\rangle$ in Eq. 6.5b more slowly, which better satisfies the adiabaticity criterion in Eq. 6.8. Overall, to improve STIRAP efficiency for Rydberg systems, it is better to make longer laser pulses than shorter ones.

6.4 Prospects for the experimental observation of optical/mm-wave STIRAP in Rydberg states

To experimentally validate an attempt at 3-level optical/mm-wave STIRAP, the final population in state $|3\rangle$ must be monitored as a function of the delay between the laser and mm-wave pulses. As the delay becomes negative (mm-waves before laser), and the two pulses are moved into the temporal arrangement shown in Fig. 6-3, there

should be a maximum in the state $|3\rangle$ population. This maximum transfer efficiency at negative pulse delay is such a unique, defining feature of STIRAP that it is referred to in the literature as the "STIRAP signature" [7].

State $|3\rangle$ population could, in principle, be detected via FID: Another mm-wave transition in a group of Rydberg levels (such as the one shown in Fig. 4-1) could be probed in order to monitor the state $|3\rangle$ population. However, one challenge of such an approach is that mm-wave power required for STIRAP is generally several orders of magnitude higher than what is required for a $\pi/2$ excitation pulse, which generates maximum FID signal. Another challenge is that the number density of emitters that is produced by our photoablation source fluctuates. Thus, the intensity of the transition being probed would also fluctuate, which would make the efficiency of the optical/mm-wave STIRAP process difficult to determine.

Ramped-field ionization detection (see Sec. 2.6.1), however, could simultaneously detect the populations in both state $|2\rangle$ (provided that it does not predissociate) and state $|3\rangle$. The ionization signals from each state would be temporally separated in the data from the time-of-flight mass spectrometer. A ratio of the signals from each state could be recorded as a function of the laser/mm-wave delay time to search for the "STIRAP signature," and subsequently measure the efficiency of the population transfer.

Chapter 7

Conclusions and future work

7.1 Spectroscopy, dynamics, and manipulations of Rydberg states

Broadband, high-resolution, direct detection of Rydberg–Rydberg transitions has been demonstrated with CPmmW spectroscopy. Because of the ∼5 kD transition dipole moments, only ∼1 μW of power for ∼1 μs is needed to fully polarize a ∼10 GHz bandwidth. Moreover, all transitions within this 10 GHz may be detected in each shot with a resolution of ∼100 kHz. Fast survey acquisition, combined with phase information from the time-domain signals, which distinguishes upward from downward transitions, makes the CPmmW technique well suited to rapidly mapping out entire manifolds of Rydberg levels.

Additionally, the CPmmW technique enables time-domain observation of dynamical phenomena, such as transient nutations, that are driven by the strong interaction of large transition dipole moments with electromagnetic radiation. Furthermore, Rydberg states may be manipulated by the easily controlled mm-wave source, and the results of these manipulations may be directly monitored with the CPmmW spectrometer. It is possible to sequentially populate states with high angular momentum and determine homogeneous lifetimes. Methods such as adiabatic sweeps and composite pulse sequences should allow for more intricate manipulations.

7.2 Cooperative effects in Rydberg systems

Superradiance, a cooperative effect, is probed directly in FID detection and indirectly using photon echoes. The CPmmW method opens a new, time-domain window into studying cooperative dynamics. For example, the photon-echo approach will be able to probe long-lived, ensemble-level coherences in Rydberg samples that have been predicted [86].

Since the cooperative effects scale linearly with the number density of Rydberg states, a higher-density source will allow for a more systematic investigation of these effects. Construction is underway of a collisional cooling photoablation beam source, which will achieve both a higher number density of $\sim 10^8$ particles/cm^3 and a narrower Doppler width of $\sim$50 kHz [56, 50, 66]. Then, the number density of Rydberg emitters will be tunable simply by adjusting the power of the excitation laser. This source will be used for studies of both atomic and molecular systems. Additionally, the strength of cooperative effects may be adjusted by varying n^*, as shown in Eq. 4.12.

7.3 Pure electronic spectroscopy of molecular Rydberg states

For *molecules* in core-nonpenetrating states ($\ell > 3$), *each* rovibrational state of the ion-core has its *own* separate manifold of Rydberg levels because the nonpenetrating Rydberg electron does not interact strongly with the ion-core, [45] which has a vibrational quantum number, v^+, and a total angular momentum quantum number (exclusive of spin), N^+. Thus, CPmmW spectra of these states should be simple in that they are "atom-like," and the resultant molecular spectra would be "pure electronic spectra," decoupled from the vibrational and rotational motions of the ion-core. These $\Delta v^+ = 0$ and $\Delta N^+ = 0$ selection rules will render the spectra to be trivially assignable, in contrast to assignment of laser transitions, which do not obey such restrictive rotation-vibration selection rules. There will be exclusively $\Delta v^+ = 0$, $\Delta N^+ = 0$ transitions, but the quantum defects will be slightly v^+, N^+

dependent. This v^+, N^+ dependence, sampled via CPmmW spectra from selectively laser populated levels with different v^+, N^+ quantum numbers, reveals the multipole moments and polarizabilities of the ion-core. The CPmmW method offers broadband search capability at sufficient resolution [37] to determine the multipole moments and polarizabilities of molecular ions through pure electronic spectroscopy of Rydberg molecules. Also, information about weak ℓ, v^+, N^+ state-mixing may be garnered from the capability to record the $\sim$1% accurate relative transition intensities inherent in the chirped pulse method [11, 10, 17].

While many molecules in core-penetrating Rydberg states undergo predissociation or autoionization faster than the $\sim$1 μs required for the collection of FID, nonpenetrating ($\ell > 3$) states typically have lifetimes longer than 10 μs, and so will live long enough to permit the recording of FID spectra. Core-nonpenetrating states of molecules can be populated using optical/mm-wave STIRAP techniques to avoid the predissociation of low-ℓ, core-penetrating Rydberg states. Other possibilities for generating core-nonpenetrating states include Stark admixing of high-ℓ character with a programmed electric field or by sequentially populating high-ℓ states with a sequence of short, crafted π pulses. Additionally, BaF is a rare example of a molecule for which the dissociation limit lies above the ionization limit into the lowest electronic state of the ion-core [33]. Hence Rydberg–Rydberg transitions in BaF will be a direct *molecular* application of all of the CPmmW techniques described in this thesis.

Appendix A

Relations between linewidth and pulse duration for some commonly encountered functions

In this appendix, I give some useful relations between linewidth and pulse duration for three functions commonly encountered in CPmmW experiments: exponential decays (Sec. A.1), Gaussians (Sec. A.2), and rectangular functions (Sec. A.3). Relations are given for both magnitude Fourier transforms and magnitude-squared Fourier transforms (power spectra). Generally, magnitude Fourier transforms are used in chirped-pulse methods because the amplitude of the magnitude Fourier transform is linearly proportional to the electric field, which is, in turn, linearly proportional to the sample polarization that the excitation pulse creates. Fourier transforms were evaluated by multiplying the function by $e^{-i\omega t}$ and integrating from either $t = 0$ to ∞ (for an exponential decay) or from $t = -\infty$ to ∞ (for Gaussians and rectangular pulses).

A.1 Exponential decays

Exponential decays have the form

$$A(t) = A_{\mathrm{o}} e^{-\gamma t} = A_{\mathrm{o}} e^{-t/\tau}, \tag{A.1}$$

where $A(t)$ is the amplitude (and A_o is the amplitude at $t = 0$), γ is the decay rate, and $\tau = \gamma^{-1}$ is the decay constant (not to be confused with the waiting time in Sec. 4.1.2). Exponential decays are generally encountered in homogeneous decay processes. Examples of homogeneous decay processes include transit-time ("fly-out") line broadening, blackbody dephasing, and superradiance.

A.1.1 Magnitude Fourier transform

The magnitude Fourier transform of an exponential decay results in a lineshape that is the square root of a Lorentzian, which depends on the angular frequency, ω, the resonant frequency, ω_o, and γ according to

$$\frac{1}{\sqrt{(\omega - \omega_o)^2 - \gamma^2}}. \tag{A.2}$$

The full width at half maximum (FWHM), Γ—which is generally the quantity that is measured experimentally—for Eq. A.2 in angular frequency units is related to the decay time τ by

$$\Gamma_\omega = \frac{2\sqrt{3}}{\tau}. \tag{A.3}$$

Here, the ω subscript denotes angular frequency units. The linear frequency, ν, is related to the angular frequency by

$$\nu = \frac{\omega}{2\pi}. \tag{A.4}$$

In linear frequency units, the FWHM of Eq. A.2 is

$$\Gamma_\nu = \frac{\sqrt{3}}{\pi\tau}, \tag{A.5}$$

where the ν subscript denotes linear frequency units. Since $\pi/\sqrt{3} \approx 2$, a practically useful approximation in this case is

$$\Gamma_\nu \approx \frac{1}{2\tau}, \tag{A.6}$$

A.1.2 Magnitude-squared Fourier transform

For a magnitude-squared Fourier transform of an exponential decay the lineshape is a Lorentzian.[1] A Lorentzian depends on the angular frequency, ω, the resonant frequency, ω_o, and γ according to

$$\frac{1}{(\omega - \omega_o)^2 - \gamma^2}. \tag{A.7}$$

In this case, the FWHM in angular frequency units is related to the decay time by

$$\Gamma_\omega = \frac{2}{\tau}, \tag{A.8}$$

and the FWHM in linear frequency units is

$$\Gamma_\nu = \frac{1}{\pi\tau}. \tag{A.9}$$

A.2 Gaussians

A Gaussian centered at $t = 0$ has the form

$$A(t) = A_o e^{-t^2/2\sigma_t^2} \tag{A.10}$$

where σ_t is the (temporal) standard deviation. Gaussian decays are generally encountered in inhomogeneous decay processes. Examples of inhomogeneous decay processes include Doppler dephasing and line broadening due to stray electric or magnetic fields.

[1] The lineshape is also a Lorentzian if an exponential decay is mirrored about the amplitude axis so that the function is 2-sided and symmetric, and a magnitude Fourier transform is taken by integrating from $t = -\infty$ to ∞.

A.2.1 Magnitude Fourier transform

The magnitude Fourier transform of a Gaussian is also a Gaussian.[2] The standard deviation in angular frequency, σ_ω, is related to σ_t by

$$\sigma_\omega = \frac{1}{\sigma_t}. \tag{A.11}$$

In linear frequency,

$$\sigma_\nu = \frac{1}{2\pi\sigma_t}. \tag{A.12}$$

In practice, though, the FWHM is generally measured. The FWHM the frequency domain in angular frequency units is

$$\Gamma_\omega = \frac{2\sqrt{2\ln 2}}{\sigma_t}. \tag{A.13}$$

In linear frequency units,

$$\Gamma_\nu = \frac{\sqrt{2\ln 2}}{\pi\sigma_t}. \tag{A.14}$$

The temporal FWHM of the Gaussian is related to σ_t by

$$T_{\mathrm{FWHM}} = 2\sqrt{2\ln 2}\ \sigma_t. \tag{A.15}$$

By this metric, Eqs. A.13 and A.14 become

$$\Gamma_\omega = \frac{8\ln 2}{T_{\mathrm{FWHM}}} \tag{A.16}$$

and

$$\Gamma_\nu = \frac{4\ln 2}{\pi\ T_{\mathrm{FWHM}}}. \tag{A.17}$$

[2]This relation is true if the limits of the Fourier transform are $t = -\infty$ and $t = +\infty$. If only the $t > 0$ component of a Gaussian is recorded, such as in an FID, the Fourier transform is less simple. In this case, it may be convenient to mirror the time trace about $t = 0$ and make the decay 2-sided in order to extract information such as a decay rate.

A.2.2 Magnitude-squared Fourier transform

For a magnitude-squared Fourier transform with the same σ_t as in Sec. A.2.1, the standard deviation in angular frequency is

$$\sigma_\omega = \frac{1}{\sqrt{2}\sigma_t}, \tag{A.18}$$

while in linear frequency,

$$\sigma_\nu = \frac{1}{2\sqrt{2}\pi\sigma_t}. \tag{A.19}$$

The FWHM relations are

$$\Gamma_\omega = \frac{2\sqrt{\ln 2}}{\sigma_t}, \tag{A.20}$$

$$\Gamma_\nu = \frac{\sqrt{\ln 2}}{\pi\sigma_t}, \tag{A.21}$$

$$\Gamma_\omega = \frac{4\sqrt{2}\ln 2}{T_{\mathrm{FWHM}}}, \tag{A.22}$$

and

$$\Gamma_\nu = \frac{2\sqrt{2}\ln 2}{\pi\ T_{\mathrm{FWHM}}}. \tag{A.23}$$

A.3 Rectangular functions

Rectangular functions, or step functions, are encountered when generating mm-wave pulses and when using rectangular windows for Fourier transforms of data traces. Rectangular pulses are characterized by a duration Δt and a constant amplitude. The relationships given in this section are useful in determining the bandwidth of a rectangular pulse with duration Δt.

A.3.1 Magnitude Fourier transform

The magnitude Fourier transform of a rectangular pulse leads to a lineshape of

$$\frac{\sin(\omega - \omega_\mathrm{o})}{(\omega - \omega_\mathrm{o})}, \tag{A.24}$$

or $\mathrm{sinc}(\omega - \omega_\mathrm{o})$. Here, the FWHM is for the main lobe of the sinc function, centered at $\omega = \omega_\mathrm{o}$. The equation for the FWHM is transcendental, and thus not analytic, but the FWHM is approximately

$$\Gamma_\omega = \frac{7.582}{\Delta t} \tag{A.25}$$

in angular frequency units. In linear frequency units,

$$\Gamma_\nu = \frac{1.207}{\Delta t}. \tag{A.26}$$

A.3.2 Magnitude-squared Fourier transform

The magnitude-squared Fourier transform of a rectangular function gives a lineshape of $\mathrm{sinc}^2(\omega - \omega_\mathrm{o})$. The approximate FWHM relations are

$$\Gamma_\omega = \frac{5.566}{\Delta t} \tag{A.27}$$

and

$$\Gamma_\nu = \frac{0.8859}{\Delta t}. \tag{A.28}$$

Bibliography

[1] K. Afrousheh, P. Bohlouli-Zanjani, D. Vagale, A. Mugford, M. Fedorov, and J. D. D. Martin. Spectroscopic Observation of Resonant Electric Dipole-Dipole Interactions between Cold Rydberg Atoms. *Physical Review Letters*, 93(23):233001, November 2004.

[2] V. M. Akulin and N. V. Karlov. *Intense Resonant Interactions in Quantum Electronics*. Texts and monographs in physics. Springer-Verlag, Berlin, 1992.

[3] W. R. Anderson, J. R. Veale, and T. F. Gallagher. Resonant Dipole-Dipole Energy Transfer in a Nearly Frozen Rydberg Gas. *Physical Review Letters*, 80(2):249–252, January 1998.

[4] J. A. Armstrong, P. Esherick, and J. J. Wynne. Bound even-parity $J = 0$ and 2 spectra of Ca: A multichannel quantum-defect theory analysis. *Physical Review A*, 15(1):180–196, January 1977.

[5] J. Baum, R. Tycko, and A. Pines. Broadband and adiabatic inversion of a two-level system by phase-modulated pulses. *Physical Review A*, 32(6):3435–3447, December 1985.

[6] Patrice Bell, F. Aguirre, E. R. Grant, and S. T. Pratt. Mode-dependent vibrational autoionization of NO_2. *The Journal of Chemical Physics*, 119(19):10146–10157, 2003.

[7] K. Bergmann, H. Theuer, and B. Shore. Coherent population transfer among quantum states of atoms and molecules. *Reviews of Modern Physics*, 70(3):1003–1025, July 1998.

[8] S. A. Borgström and J. R. Rubbmark. Stark mixing of high-lying calcium levels by laser-produced charges. *Journal of Physics B: Atomic and Molecular Physics*, 10(18):3607–3615, December 1977.

[9] C. M. Brown, S. G. Tilford, and M. L. Ginter. Absorption spectrum of Ca I in the 1580–2090-Å region. *Journal of the Optical Society of America*, 63(11):1454–1462, November 1973.

[10] Gordon G. Brown, Brian C. Dian, Kevin O. Douglass, Scott M. Geyer, and Brooks H. Pate. The rotational spectrum of epifluorohydrin measured by chirped-pulse Fourier transform microwave spectroscopy. *Journal of Molecular Spectroscopy*, 238(2):200–212, August 2006.

[11] Gordon G. Brown, Brian C. Dian, Kevin O. Douglass, Scott M. Geyer, Steven T. Shipman, and Brooks H. Pate. A broadband Fourier transform microwave spectrometer based on chirped pulse excitation. *The Review of Scientific Instruments*, 79(5):053103, May 2008.

[12] Francis X. Campos, Yanan Jiang, and Edward R. Grant. Triple-resonance spectroscopy of the higher excited states of NO_2: Rovibronic interactions, autoionization, and ℓ-uncoupling in the (100) manifold. *The Journal of Chemical Physics*, 93(4):2308–2327, 1990.

[13] Ling Chen, Charles E. Cottrell, and Alan G. Marshall. Effect of signal-to-noise ratio and number of data points upon precision in measurement of peak amplitude, position and width in Fourier transform spectrometry. *Chemometrics and Intelligent Laboratory Systems*, 1(1):51–58, November 1986.

[14] Jason Otto Clevenger. *Spectra and Dynamics of Calcium Monochloride*. PhD thesis, Massachusetts Institute of Technology, 2002.

[15] Anthony P. Colombo, Yan Zhou, Kirill Prozument, Stephen L. Coy, and Robert W. Field. Chirped-pulse millimeter-wave spectroscopy: Spectrum, dynamics, and manipulation of Rydberg–Rydberg transitions. *The Journal of Chemical Physics*, 138(1):014301, 2013.

[16] E. U. Condon and G. H. Shortley. *The Theory of Atomic Spectra*. Cambridge University Press, 1964.

[17] Brian C. Dian, Gordon G. Brown, Kevin O. Douglass, and Brooks H. Pate. Measuring picosecond isomerization kinetics via broadband microwave spectroscopy. *Science*, 320(5878):924–8, May 2008.

[18] R. H. Dicke. Coherence in Spontaneous Radiation Processes. *Physical Review*, 93(1):99–110, January 1954.

[19] C. Fabre, S. Haroche, and P. Goy. Millimeter spectroscopy in sodium Rydberg states: Quantum-defect, fine-structure, and polarizability measurements. *Physical Review A*, 18(1):229–237, July 1978.

[20] Ray Freeman, Stewart P. Kempsell, and Malcolm H. Levitt. Radiofrequency pulse sequences which compensate their own imperfections. *Journal of Magnetic Resonance*, 38(3):453–479, March 1980.

[21] Thomas F. Gallagher. *Rydberg Atoms*. Cambridge University Press, Cambridge, 1994.

[22] Thomas F. Gallagher and Pierre Pillet. Dipole–Dipole Interactions of Rydberg Atoms. In E. Arimondo, P. R. Berman, and C. C. Lin, editors, *Advances in Atomic, Molecular, and Optical Physics*, volume 56, pages 161–218. Elsevier Academic Press, Amsterdam, 2008.

[23] W. R. S. Garton and K. Codling. Ultra-violet extensions of the arc spectra of the alkaline earths: the absorption spectrum of calcium vapour. *Proceedings of the Physical Society*, 86(5):1067–1075–1152–1, November 1965.

[24] U. Gaubatz, P. Rudecki, S. Schiemann, and K. Bergmann. Population transfer between molecular vibrational levels by stimulated Raman scattering with partially overlapping laser fields. A new concept and experimental results. *The Journal of Chemical Physics*, 92(9):5363–76, 1990.

[25] Thomas R. Gentile, Barbara J. Hughey, Daniel Kleppner, and Theodore W. Ducas. Microwave spectroscopy of calcium Rydberg states. *Physical Review A*, 42(1):440–451, July 1990.

[26] Christopher M. Gittins. *Electronic structure and electronic-vibrational energy exchange in Rydberg states of calcium monofluoride*. PhD thesis, Massachusetts Institute of Technology, 1995.

[27] F. Gounand, M. Hugon, P. R. Fournier, and J. Berlande. Superradiant cascading effects in rubidium Rydberg levels. *Journal of Physics B: Atomic and Molecular Physics*, 12(4):547–553, February 1979.

[28] P. Goy, J. M. Raimond, G. Vitrant, and S. Haroche. Millimeter-wave spectroscopy in cesium Rydberg states. Quantum defects, fine- and hyperfine-structure measurements. *Physical Review A*, 26(5):2733–2742, November 1982.

[29] M. Gross, P. Goy, C. Fabre, S. Haroche, and J. M. Raimond. Maser Oscillation and Microwave Superradiance in Small Systems of Rydberg Atoms. *Physical Review Letters*, 43(5):343–346, July 1979.

[30] S. Guizard, N. Shafizadeh, M. Horani, and D. Gauyacq. nf Rydberg complexes of NO in a magnetic field, probed by double resonance multiphoton ionization. *The Journal of Chemical Physics*, 94(11):7046–7060, 1991.

[31] E. L. Hahn. Spin Echoes. *Physical Review*, 80(4):580–594, November 1950.

[32] S. D. Hogan, J. A. Agner, F. Merkt, T. Thiele, S. Filipp, and A. Wallraff. Driving Rydberg-Rydberg Transitions from a Coplanar Microwave Waveguide. *Physical Review Letters*, 108(6):063004, February 2012.

[33] Zygmunt J. Jakubek and Robert W. Field. Core-penetrating Rydberg series of BaF: $s{\sim}p{\sim}d{\sim}f$ supercomplexes. *Physical Review Letters*, 72(14):2167–2170, April 1994.

[34] N. J. A. Jones, R. S. Minns, R. Patel, and H. H. Fielding. Observation of the Stark effect in $v^+ = 0$ Rydberg states of NO: a comparison between predissociating and bound states. *Journal of Physics B: Atomic, Molecular and Optical Physics*, 41(18):185102, September 2008.

[35] Jeffrey J. Kay. *Rydberg Series of Calcium Monofluoride: Spectrum, Structure, and Dynamics*. PhD thesis, Massachusetts Institute of Technology, 2007.

[36] Jeffrey J. Kay, Daniel S. Byun, Jason O. Clevenger, Xing Jiang, Vladimir S. Petrović, Robert Seiler, Jonathan R. Barchi, Anthony J. Merer, and Robert W. Field. "Spectrum-only" assignment of core-penetrating and core-nonpenetrating Rydberg states of calcium monofluoride. *Canadian Journal of Chemistry*, 82(6):791–803, June 2004.

[37] Jeffrey J. Kay, Stephen L. Coy, Vladimir S. Petrović, Bryan M. Wong, and Robert W. Field. Separation of long-range and short-range interactions in Rydberg states of diatomic molecules. *The Journal of Chemical Physics*, 128(19):194301, May 2008.

[38] Ēriks Kupče and Ray Freeman. Stretched Adiabatic Pulses for Broadband Spin Inversion. *Journal of Magnetic Resonance, Series A*, 117(2):246–256, December 1995.

[39] J. Lambert, Michael W. Noel, and T. F. Gallagher. Rydberg-atom population transfer by population trapping in a chirped microwave pulse. *Physical Review A*, 66(5):053413, November 2002.

[40] H. Lefebvre-Brion and R. W. Field. *The Spectra and Dynamics of Diatomic Molecules*. Elsevier Academic Press, 2004.

[41] Malcolm H. Levitt. Symmetrical composite pulse sequences for NMR population inversion. I. Compensation of radiofrequency field inhomogeneity. *Journal of Magnetic Resonance*, 48(2):234–264, June 1982.

[42] Malcolm H. Levitt and R. R. Ernst. Composite pulses constructed by a recursive expansion procedure. *Journal of Magnetic Resonance*, 55(2):247–254, November 1983.

[43] Malcolm H. Levitt and Ray Freeman. NMR population inversion using a composite pulse. *Journal of Magnetic Resonance*, 33(2):473–476, February 1979.

[44] Wenhui Li, I. Mourachko, M. W. Noel, and T. F. Gallagher. Millimeter-wave spectroscopy of cold Rb Rydberg atoms in a magneto-optical trap: Quantum defects of the ns, np, and nd series. *Physical Review A*, 67(5):052502, May 2003.

[45] Stephen R. Lundeen. Fine Structure in High-L Rydberg States: A Path to Properties of Positive Ions. In P. R. Berman and C. C. Lin, editors, *Advances in Atomic, Molecular, and Optical Physics*, volume 52 of *Advances In Atomic,*

Molecular, and Optical Physics, pages 161–208. Elsevier Academic Press, Amsterdam, 2005.

[46] David J. Lurie. Numerical design of composite radiofrequency pulses. *Journal of Magnetic Resonance*, 70(1):11–20, October 1986.

[47] A. M. Lyyra, W. T. Luh, L. Li, H. Wang, and W. C. Stwalley. The A $^1\Sigma_u^+$ state of the potassium dimer. *The Journal of Chemical Physics*, 92(1):43–50, 1990.

[48] J. C. MacGillivray and M. S. Feld. Theory of superradiance in an extended, optically thick medium. *Physical Review A*, 14(3):1169–1189, September 1976.

[49] H. Maeda, J. H. Gurian, D. V. L. Norum, and T. F. Gallagher. Coherent Population Transfer in an Atom by Multiphoton Adiabatic Rapid Passage. *Physical Review Letters*, 96(7):073002, February 2006.

[50] S. E. Maxwell, N. Brahms, R. deCarvalho, D. R. Glenn, J. S. Helton, S. V. Nguyen, D. Patterson, J. Petricka, D. DeMille, and J. M. Doyle. High-Flux Beam Source for Cold, Slow Atoms or Molecules. *Physical Review Letters*, 95(17):173201, October 2005.

[51] J. C. McGurk, R. T. Hofmann, and W. H. Flygare. Transient absorption and emission and the measurement of T_1 and T_2 in the J 0→1 rotational transition in OCS. *The Journal of Chemical Physics*, 60(7):2922–2928, April 1974.

[52] J. C. McGurk, T. G. Schmalz, and W. H. Flygare. Fast passage in rotational spectroscopy: Theory and experiment. *The Journal of Chemical Physics*, 60(11):4181–4188, June 1974.

[53] F. Merkt. Molecules in high Rydberg states. *Annual Review of Physical Chemistry*, 48(2):675–709, January 1997.

[54] F. Merkt and A. Osterwalder. Millimetre wave spectroscopy of high Rydberg states. *International Reviews in Physical Chemistry*, 21(3):385–403, July 2002.

[55] F. Merkt and H. Schmutz. Very high resolution spectroscopy of high Rydberg states of the argon atom. *The Journal of Chemical Physics*, 108(24):10033–10045, 1998.

[56] J. K. Messer and Frank C. De Lucia. Measurement of Pressure-Broadening Parameters for the CO-He System at 4 K. *Physical Review Letters*, 53(27):2555–2558, December 1984.

[57] L. Moi, C. Fabre, P. Goy, M. Gross, S. Haroche, P. Encrenaz, G. Beaudin, and B. Lazareff. Heterodyne detection of Rydberg atom maser emission. *Optics Communications*, 33(1):47–50, April 1980.

[58] B. R. Mollow. Power Spectrum of Light Scattered by Two-Level Systems. *Physical Review*, 188(5):1969–1975, December 1969.

[59] I. Mourachko, D. Comparat, F. de Tomasi, A. Fioretti, P. Nosbaum, V. M. Akulin, and P. Pillet. Many-Body Effects in a Frozen Rydberg Gas. *Physical Review Letters*, 80(2):253–256, January 1998.

[60] Klaus Müller-Dethlefs and Edward W. Schlag. High-Resolution Zero Kinetic Energy (ZEKE) Photoelectron Spectroscopy of Molecular Systems. *Annual Review of Physical Chemistry*, 42(1):109–136, October 1991.

[61] A. Osterwalder, R. Seiler, and F. Merkt. Measurement of the hyperfine structure in low-ℓ, high-n Rydberg states of ortho H_2 by millimeter wave spectroscopy. *The Journal of Chemical Physics*, 113(18):7939–7944, 2000.

[62] A. Osterwalder, S. Willitsch, and F. Merkt. High-resolution pulsed field ionization study of high Rydberg states of benzene. *Journal of Molecular Structure*, 599(1-3):163–176, December 2001.

[63] A. Osterwalder, A. Wüest, F. Merkt, and Ch. Jungen. High-resolution millimeter wave spectroscopy and multichannel quantum defect theory of the hyperfine structure in high Rydberg states of molecular hydrogen H_2. *The Journal of Chemical Physics*, 121(23):11810–11838, 2004.

[64] G. Barratt Park, Adam H. Steeves, Kirill Kuyanov-Prozument, Justin L. Neill, and Robert W. Field. Design and evaluation of a pulsed-jet chirped-pulse millimeter-wave spectrometer for the 70–102 GHz region. *The Journal of Chemical Physics*, 135(2):024202, July 2011.

[65] Hyunwook Park, P. J. Tanner, B. J. Claessens, E. S. Shuman, and T. F. Gallagher. Dipole-dipole broadening of Rb ns – np microwave transitions. *Physical Review A*, 84(2):22704, August 2011.

[66] David Patterson and John M. Doyle. Bright, guided molecular beam with hydrodynamic enhancement. *The Journal of Chemical Physics*, 126(15):154307, April 2007.

[67] D. W. Posener. Precision in measuring resonance spectra. *Journal of Magnetic Resonance*, 14(2):121–128, May 1974.

[68] S. T. Pratt. Vibrational autoionization in polyatomic molecules. *Annual Review of Physical Chemistry*, 56(1):281–308, January 2005.

[69] S. T. Pratt, J. L. Dehmer, P. M. Dehmer, and W. A. Chupka. Reactions of Rydberg states of molecular hydrogen. *The Journal of Chemical Physics*, 101(2):882–890, 1994.

[70] Kirill Prozument, Anthony P. Colombo, Yan Zhou, G. Barratt Park, Vladimir S. Petrović, Stephen L. Coy, and Robert W. Field. Chirped-Pulse Millimeter-Wave Spectroscopy of Rydberg-Rydberg Transitions. *Physical Review Letters*, 107(14):143001, September 2011.

[71] I. I. Rabi, N. F. Ramsey, and J. Schwinger. Use of Rotating Coordinates in Magnetic Resonance Problems. *Reviews of Modern Physics*, 26(2):167–171, April 1954.

[72] J. M. Raimond, G. Vitrant, and S. Haroche. Spectral line broadening due to the interaction between very excited atoms: 'the dense Rydberg gas'. *Journal of Physics B: Atomic and Molecular Physics*, 14(21):L655–L660, November 1981.

[73] Jan R. Rubbmark, Michael M. Kash, Michael G. Littman, and Daniel Kleppner. Dynamical effects at avoided level crossings: A study of the Landau-Zener effect using Rydberg atoms. *Physical Review A*, 23(6):3107–3117, June 1981.

[74] J. R. Rydberg. XXXIV. On the structure of the line-spectra of the chemical elements. *Philosophical Magazine Series 5*, 29(179):331–337, April 1890.

[75] M Schäfer, M Andrist, H Schmutz, F Lewen, G Winnewisser, and F Merkt. A 240–380 GHz millimetre wave source for very high resolution spectroscopy of high Rydberg states. *Journal of Physics B: Atomic, Molecular and Optical Physics*, 39(4):831–845, February 2006.

[76] Klaus Siglow, Robert Neuhauser, and Hans Jürgen Neusser. Resolved high Rydberg spectroscopy of benzene·rare gas van der Waals clusters: Enhancement of spin–orbit coupling in the radical cation by an external heavy atom. *The Journal of Chemical Physics*, 110(12):5589–5599, 1999.

[77] N. Skribanowitz, I. P. Herman, J. C. MacGillivray, and M. S. Feld. Observation of Dicke Superradiance in Optically Pumped HF Gas. *Physical Review Letters*, 30(8):309–312, February 1973.

[78] J. Stanojevic, R. Côté, D. Tong, E. E. Eyler, and P. L. Gould. Long-range potentials and $(n-1)d{+}ns$ molecular resonances in an ultracold Rydberg gas. *Physical Review A*, 78(5):052709, November 2008.

[79] Jack Sugar and Charles Corliss. Atomic Energy Levels of the Iron-Period Elements: Potassium through Nickel. *Journal of Physical and Chemical Reference Data*, 14(Supplement 2):1–664, 1985.

[80] Paul J. Tanner, Jianing Han, E. S. Shuman, and T. F. Gallagher. Many-Body Ionization in a Frozen Rydberg Gas. *Physical Review Letters*, 100(4):043002, January 2008.

[81] H. C. Torrey. Transient Nutations in Nuclear Magnetic Resonance. *Physical Review*, 76(8):1059–1068, October 1949.

[82] A. Ganesh Vaidyanathan, William P. Spencer, Jan R. Rubbmark, Hajo Kuiper, Claude Fabre, Daniel Kleppner, and Theodore W. Ducas. Experimental study of nonadiabatic core interactions in Rydberg states of calcium. *Physical Review A*, 26(6):3346–3350, December 1982.

[83] Nikolay V. Vitanov, Thomas Halfmann, Bruce W. Shore, and Klaas Bergmann. Laser-induced population transfer by adiabatic passage techniques. *Annual Review of Physical Chemistry*, 52:763–809, January 2001.

[84] T. Wang, S. F. Yelin, R. Côté, E. E. Eyler, S. M. Farooqi, P. L. Gould, M. Koštrun, D. Tong, and D. Vrinceanu. Superradiance in ultracold Rydberg gases. *Physical Review A*, 75(3):33802, March 2007.

[85] S. F. Yelin and Michael Fleischhauer. Modification of local field effects in two level systems due to quantum corrections. *Optics Express*, 1(6):160–168, September 1997.

[86] Yan Zhou. Cooperative effects in a dense Rydberg gas. *Molecular Physics*, 110(15-16):1909–1915, August 2012.